UNIVERSITY OF CALIFORNIA, MERCED

Advanced Computational Approaches to Plasma Behavior in Argon and Helium Systems

A dissertation submitted in partial satisfaction of the

requirements for the degree of

Doctor of Philosophy

in

Mechanical Engineering

by

José Alfredo Millán Higuera

Committee in charge:

Professor Venkattraman Ayyaswamy, Chair
Professor Gerardo Diaz
Professor Jeanette Cobian
Professor Yanbao Ma

Summer 2024

Advanced Computational Approaches to Plasma Behavior in Argon and Helium Systems

The dissertation of José Alfredo Millán Higuera, titled Advanced Computational Approaches to Plasma Behavior in Argon and Helium Systems, is approved:

Chair _____

Venkattraman Ayyaswamy

_____

Gerardo Diaz

_____

Jeanette Cobian

_____

Yanbao Ma

University of California, Merced

To José Alfredo Millán Ramirez and Adriana Higuera Espinoza

For all the support provided professionally and personally during all these years.

Acknowledgments

The completion of this dissertation was a collective effort. Although I am the main author, many others have contributed significantly to my professional development. I want to thank my supervisor, Dr. Venkattraman Ayyaswamy, for his expertise, patience, and the freedom he provided to explore the topics independently, allowing for comprehensive research in plasma. Additionally, I extend my gratitude to Dr. Saravanapriyan Sriraman for the opportunity to develop my skill set and expertise in a professional environment at Lam Research, where I worked with a dynamic team developing novel modeling methodologies at the rapid pace characteristic of the semiconductor industry.

I also acknowledge the professors at UC Merced whose expertise provided essential pieces of the puzzle that helped me further develop my skillset holistically. Lastly, I am grateful to my colleagues, whose endless conversations, whether related to plasmas or not, sparked ideas that were instrumental in developing the various concepts I explored during my research.

Contents

List of Figures

List of Tables

Vita

Jose Alfredo Millan Higuera received the Bachelor of Science Degree in Mechanical Engineering from University of Puerto Rico, Mayaguez in June of 2018. In August 2018, Jose started in the graduate program at University of California, Merced, as a Ph.D. student working with Professor Venkattraman Ayyaswamy. Jose research interests include computational plasma physics with emphasis on weakly ionized, atmospheric plasmas while combining control of the plasmas to explore potential solutions in a scalable manner.

Abstract

Advanced Computational Approaches to Plasma Behavior in Argon and Helium Systems

by

José Alfredo Millán Higuera

Doctor of Philosophy in Mechanical Engineering

University of California, Merced

Professor Venkattraman Ayyaswamy, Chair

This dissertation undertakes a comprehensive exploration of computational methods for studying and optimizing plasma processes, focusing specifically on the behavior and characteristics of atmospheric plasmas under various ignition waveforms. Leveraging somaFOAM, an in-house plasma solver based on OpenFOAM, this research delves into the effects of different voltage profiles—including sinusoidal, unipolar, bipolar, and sinusoidal damped waveforms—on plasma stability and efficiency. While atmospheric plasmas provide potential novel applications in medical, surface treatment, water purification, and decontamination of surfaces, the main limitation is the inherent instability of atmospheric plasma due to the high breakdown voltage. Furthermore, its traditional mode of operation, which consists of filamentary discharges, can be counterproductive to surface treatment as the filaments current are discretized, now allowing for fine control of the system when the sensitivity of the surface needs to be considered, alongside the nonuniform mode of operation. As such, atmospheric pressure glow discharges, operating in the radio frequency regime, allow for modular control of the plasma intensity while allowing the surface to be treated uniformly. Further study is of interest to supplant and replace depending on the application filamentary discharges. However, a systematic understanding of the controlling parameters within the plasma is required to have a stable glow discharge, as the ignition of an atmospheric glow discharge is inherently difficult due to the high power required to operate at atmospheric pressure. As such, it is interesting to study modes of control to ignite a stable plasma while simultaneously maximizing its reactivity, as these properties are inverse to each other.

As such, the first project aims to consider control of the input parameters by utilizing different ignition waveforms at the same cycled-averaged power to study the effects of utilizing different waveforms on plasma stability and reactivity. However, as the

feedstock gases also affect the characterization of the waveforms, two feedstock gases, argon and helium, are utilized to establish independence or dependence on the feedstock gas while at the same time studying the benefits of each feedstock gas, helium provides ease of operation and characterization, argon has been touted as a low-cost alternative which also promises ease of operation in comparison to other feedstock gas. Analysis is provided to determine whether the plasma operates in the α or γ mode of operation. However, further research is required, such as determining the criticality of the waveforms utilized to operate the plasma while at the same time investigating the effects of dielectric barrier discharges to maximize reactivity within the system, as previous research in the kilohertz regime seems to indicate that dielectrics can stabilize the plasma operation.

The second project further investigates argon plasma as research also considers the potential for scalability of the plasma, for which argon provides an opportunity. α-γ relationship between the voltage and current, the relationship between the γ mode of operation and a plasma dominated by secondary electron emissions followed by the study of the electron profiles as a relationship of stability, the relationship between the bulk voltage and input voltage for the pulsed waveforms for power coupling are studied for bare electrodes in order to provide a comprehensive picture of the plasma characterization, allowing for a deeper study of the plasma physics compared to the first project which one touched to a surface level as the interest was to determine the effects of the waveform coupled with the feedstock gas. At the same time, the addition of dielectric elements is considered within the dielectric gap to characterize the addition of such elements into the plasma and whenever such a strategy to maximize reactivity and stability is feasible. The third project, inspired upon the numerical downtime of utilizing modeling techniques in the second project, intends to use dynamic mode decomposition as a data-driven method to obtain a prediction that is adequate for purposes of analysis and characterization of the plasma without the computational downtime, utilizing a domain of parametrized solutions to train the model. Three cases are evaluated, with the first case at the boundary of the solution domain, the second case within the domain of the solution, and the third case partially outside the domain of the solution to evaluate edge cases and cases within the domain of the solution to determine the strength and weaknesses of the prediction, to be able to utilize data-driven techniques with existing databases to be able to characterize the plasma without the computational burden encountered with modeling techniques, allowing for just-in-time data results, improving efficiency.

The different projects presented here aim to comprehensively describe atmospheric plasmas and their characterization under different feedstock gases and input waveforms in order to propose a new way to maximize stability and reactivity simultaneously, utilizing a control approach to achieve this. At the same time, as parametrization techniques are computationally expensive, a data-driven technique could be seen

as another tool to minimize computational downtime while obtaining results that can be utilized to understand the plasma characterization, allowing for a more efficient control mode of the plasma.

Chapter 1

Introduction

1.1 Plasma fundamentals

Plasmas, also known as the fourth state of matter, make up a large portion of the available matter in the universe, with more than 99 % of matter being plasma [1]. Although similar in composition to a gas, plasma is thermally and electrically conductive, as the free ions and electrons facilitate the conductivity of thermal and electrical loads [2, 3, 4]. An important distinction in plasmas is whether they are thermal or nonthermal, which informs the range of operations and applications where they can be applied. For practical applications, which are the focus of this document, thermal plasmas are classified as plasmas where the energy of the electrons and the other charged species match each other [5, 6]. In contrast, in nonthermal plasmas, there are orders of magnitude differences in the energy of the electrons compared to the ions [5, 6]. This relationship can be expressed as $T_e >> T_i$ for nonthermal plasmas and $T_e \sim T_i$ for thermal plasmas.

Different applications and points of interest for thermal plasmas include aerospace applications such as the ignition of scramjet systems [7] and engineering solutions tailored towards re-entry of launch vehicles into the atmosphere [8] and hypersonic systems [9], applications within heavy industries such as garbage disposal [10], welding [11], surface cutting [12], diamond growth [13], and metal component melting [14], among others. In the automotive industry, thermal plasmas are widely utilized for the ignition of combustion processes through the use of spark plugs [15]. Other thermal plasma processes include generating extreme ultraviolet (EUV) light [16] and nuclear fusion processes [17]. Therefore, the need for thermal plasmas in modern applications is widespread. Figure 1.1 showcases a schematic of an inductively coupled plasma (ICP) utilized in different thermal applications [11, 12, 14].

On the other hand, nonthermal plasmas, alongside laser-assisted plasmas in the generation of EUV light, form the backbone of the semiconductor industry. Nonthermal plasmas in different ignition modes are responsible for various processes, such as

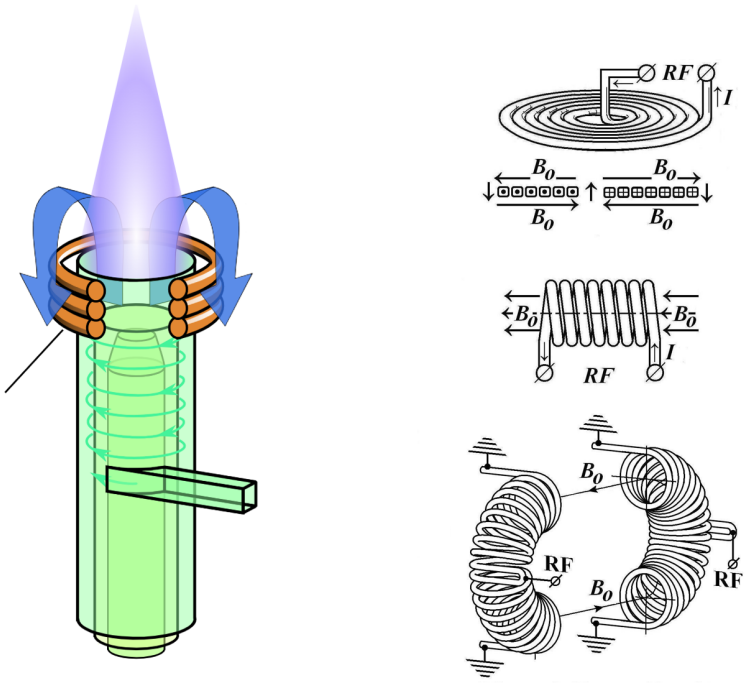

Figure 1.1: Schematic diagrams of ICP plasmas in different configurations. ICP processes are employed in various thermal plasma applications.

etching [19, 20], surface decontamination [21], and deposition [22]. Recently, plasma processes have also gained interest due to their benefits in medical applications, such as the topical treatment of cancer, the healing of scarring tissues due to burns, and the healing of tissue affected by invasive methods in medical procedures [23]. Other applications, such as water treatment and agricultural processes [24, 21], are also fields of application for nonthermal plasmas, where successes have been found in decontamination and surface treatment. The study of nonthermal plasmas is of particular interest due to the array of applications that can be utilized with great success. Figure 1.2 showcases a schematic of different dielectric barrier discharge (DBD) systems utilized in the ignition of nonthermal plasma at atmospheric pressure [25].

Nonthermal plasmas, depending on the operational parameters and electro-spatial characterization, can be classified as DBD [18, 26, 27], glow discharge [28, 29, 30], atmospheric pressure glow discharge (APGD) [18, 31, 32], and capacitively coupled plasma (CCP) [19, 33, 34], to mention a few modes of operation. These classifications might overlap, such as an APGD plasma operating in the radio frequency (RF) regime, which can also function as a CCP [22]. The descriptions of these plasmas are as follows:

• **DBD:** Plasma operated in the kilohertz (kHz) regime at atmospheric pressure,

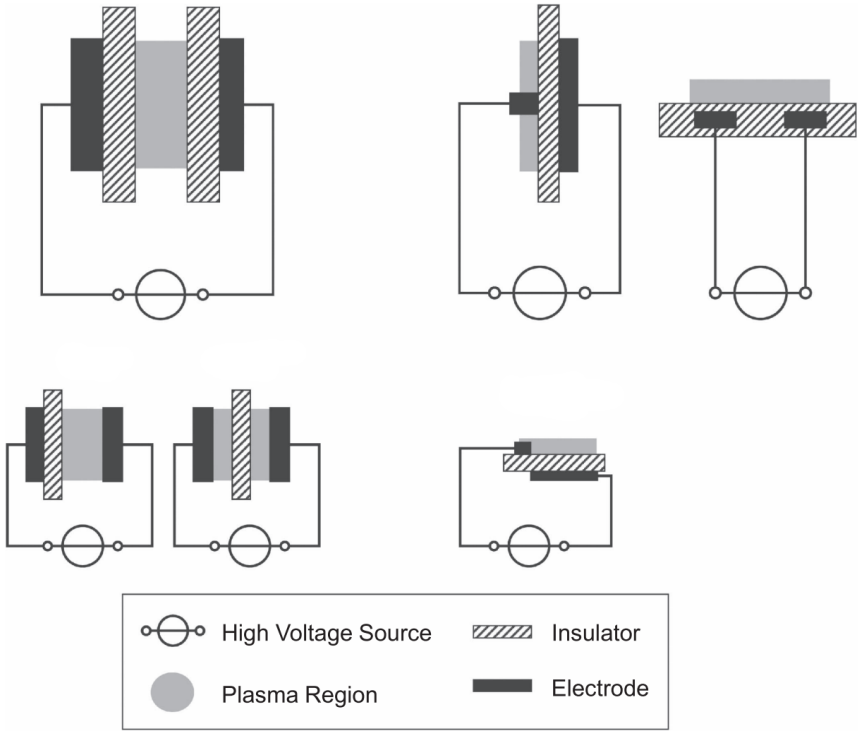

Figure 1.2: Basic planar configurations of DBDs [18]. Different configurations are utilized depending on the case being studied.

where a high voltage breaks down the plasma [18]. Stability is achieved with a dielectric barrier in the electrodes, where the dielectric acts as a ballast, accumulating charge and countering charges within the plasma to avoid arcing [35, 36]. These plasmas manifest as streamers in operations of interest [36].

- **Glow Discharge:** Plasmas operated using a DC source at reduced pressures appear as a cloud of light enclosed by the reactor [37]. They can also operate in the RF regime at reduced and atmospheric pressures [34, 38].

- **APGD:** This is a subclassification of glow discharge plasmas. These plasmas are ignited under atmospheric pressure at different operational regimes [39, 40], such as RF or kHz. The selection of feedstock gas is important to minimize instabilities [41], particularly for plasmas operating in the kHz regime [42].

- **CCP:** Plasma operated in the RF frequency regime, where the operation of the plasma at this frequency causes a capacitive effect, manifested in the phase shift angle between current density and operating voltage in sinusoidal driven plasmas [19, 34, 43].

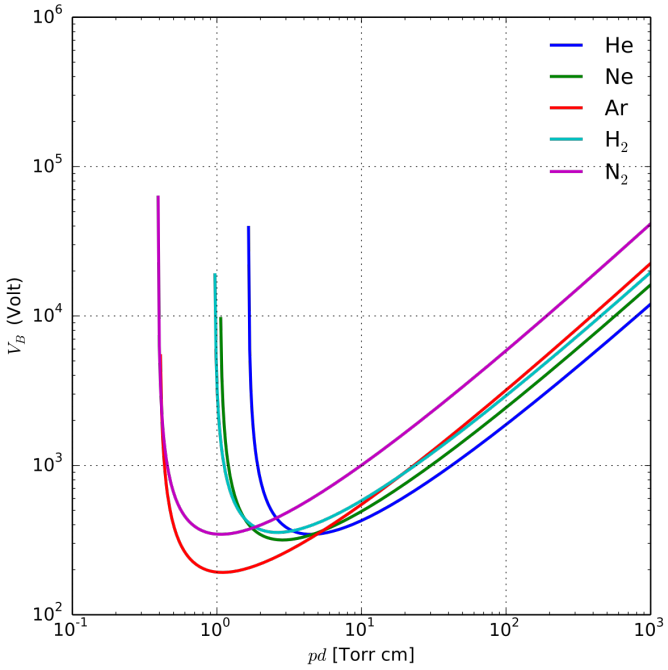

Figure 1.3: Paschen curve for different gases at various operating pressures and gaps.

Given the variety of operational modes and their distinct characteristics, it would be unfeasible to study all the aforementioned modes of operation. Therefore, this study focuses on APGD-CCP and CCP-DBD, as they present novel opportunities in applications of interest due to the ease of ignition and relatively low operating costs since such plasmas do not require vacuum systems to achieve operations of interest [22, 38, 39].

Two modes of operation are important to distinguish the stability of the system: the α and γ modes [31, 44, 45, 46]. These modes differ in their electron generation and current ranges. The alpha mode operates at low current density, where the plasma process is sustained by bulk ionization [31]. In contrast, the γ mode operates at a high current density and sustains the plasma through secondary electron emissions (SEE) [31, 47]. In the γ mode, the collision of ions with the electrode generates secondary electrons, further intensifying the plasma. SEE depends on the electrode or dielectric material [48]. The γ mode of operation should be avoided as it is prone to instabilities such as constriction and filamentation, potentially leading to arcing if plasma parameters are not properly controlled [46, 49, 50]. While DBD plasmas are typically ignited in a filamentary form when operated in the kHz regime, one of the main interests in APGD plasmas is their glow structure, allowing for their use in applications where a filamentary discharge would not be suitable due to the risk of

damage associated with the high operating current of DBD plasmas [51].

An external power supply ignites APGD-CCP and DBD-CCP plasmas in the RF frequency regime. Depending on the feedstock gas, different breakdown voltages are encountered as a function of operating pressure and reactor dimension. This relationship can be expressed with the Paschen equation, an empirical relationship relating the aforementioned parameters [52].

$$V_b = \frac{B(p \cdot d)}{\ln\left[A(p \cdot d)\right] - \ln\left[\ln\left(1 + 1/\gamma_{se}\right)\right]} \tag{1.1}$$

In the Paschen equation, A and B are constants found experimentally depending on the feedstock gas, γ is the SEE coefficient, d is the gap of the plasma reactor, and p is the system's pressure. The reactor's pressure and gap size determine the plasma's breakdown voltage and feedstock gas selected for the plasma system. The Paschen curve, while obtained by the ignition of an arc for a feedstock gas, a similar curve with a similar trend is also obtained for breakdown voltages for both direct current (DC) and frequency driven plasmas [53, 54], providing important insights into the ignition characteristics of the feedstock gas to be utilized. For the frequency of interest, RF, it is observed that the breakdown voltage decreases by 20% compared to a plasma operated in the kHz regime [53], indicating that a lower voltage is required for plasma ignition. Figure 1.4 showcases the relationship between breakdown voltage and frequency for sinusoidal ignition waveform. This observation aligns with numerous published papers, where the operational voltage of DBD plasmas [55] is compared to that of APGD-CCP plasmas [39], showing a decrease in voltage by an order of magnitude. An important consideration when studying plasmas is that the breakdown voltage is always higher than the operating voltage [38]. The initial process necessitates a high voltage to break down the feedstock gas utilized to ignite the plasma. Afterward, the plasma is self-sustained by operating in the α and γ mode by highly energetic electrons flowing through the space as a function of the potential within the system and generating charged species as they collide with neutral species. However, these electrons do not require a large driving voltage as pre-breakdown conditions because there is already a level of ionization within the system [39].

Other considerations, as shown in the pressure-distance relationship, indicate that a larger voltage is required to initiate the breakdown process as the pressure and distance increase as seen in figure 1.3. This is less than ideal for atmospheric plasmas due to the high power requirements of high pressure-distance values. While decreasing the pressure or gap of the reactor will alleviate the need for high operational power, reducing the pressure necessitates using vacuum systems, defeating the purpose of studying atmospheric pressure plasmas if vacuum systems are needed. Reducing the gap can be done, but it is important to determine whether such a reduction is feasible for the applications of interest, as reducing the gap might be tailored toward other applications outside the scope of this study.

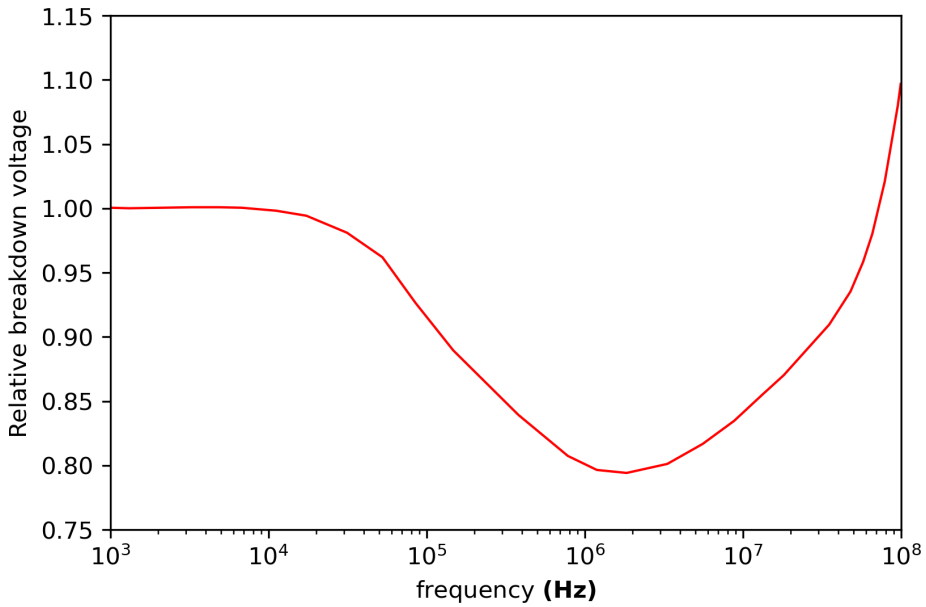

Figure 1.4: Ratio of the breakdown voltage at an operating frequency to the Paschen breakdown voltage.

Hence, the interest in studying different feedstock gases to operating parameters is crucial, as certain gases ignite more easily than others, facilitating the study and application of plasma processes. Nonetheless, operational costs must be considered to minimize the cost of an application of interest. As shown in figure 1.3, different gases utilized, and the pd values to ensure ignition indicate that helium is the most stable and easiest plasma to ignite compared to the alternatives. However, compared to other gases such as argon, the high operating cost of helium [56] limits its applications to laboratory settings where the goal is to ensure the stability of the system being studied and understand the response to the operational parameters before expanding to practical applications. Therefore, it is of interest to study alternatives that provide low operational costs and stable operation akin to that provided by a helium plasma.

Besides the aforementioned parameters to stabilize the plasma, such as reactor gap, pressure, and feedstock gas, a DBD can also be utilized to stabilize the plasma [58]. However, such effects are unclear in plasmas operating in the DBD-RF configuration under different ignition profiles. Nonetheless, there is still interest in investigating the effects of integrating such elements into the reactors, as the main interest is to maximize the system's stability while maximizing reactivity. These two factors, however, are inversely related; the more reactive the plasma, the less stable it becomes [22]. Therefore, it is of interest to study the parameterization of the input waveforms utilized in power supplies to ignite the plasma, as in many instances, oper-

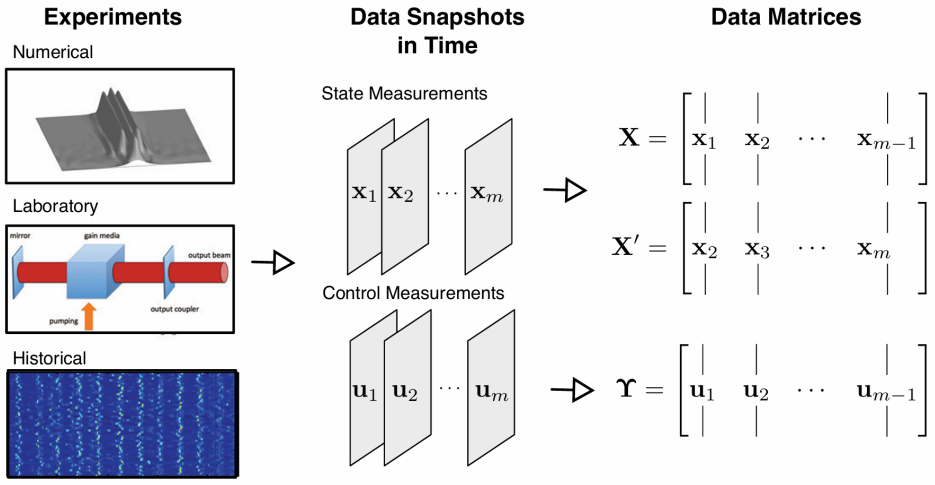

Figure 1.5: Schematic overview of DMD on a fluid flow [57].

ating parameters such as duty cycle, amplitude, frequency, and damping factor can be modified to optimize a solution where plasma reactivity is maximized while avoiding instabilities and arcing of the system. This problem thus becomes a control problem where multiple variables are carefully parameterized to maximize the solution given a set of conditions.

As such, maximizing plasma reactivity while maintaining a stable mode of operation is an ideal problem that could be explored using machine-learning methods. Methods such as dynamic mode decomposition (DMD) allow for training datasets to predict behavior and thus speed up results that would otherwise be obtained using conventional plasma modeling tools, adding overhead which is often time prohibitive [59]. By exploring such methods, gaps in the data they were originally trained on can be predicted, allowing for running different parameterization studies while minimizing time constraints [60]. Such machine learning algorithms could be utilized to study ways to minimize power consumption during the breakdown process, which, in many instances, is ignited using a sinusoidal waveform that is less than ideal for system efficiency. Nonetheless, utilization of such algorithms warrants comprehensive study to determine their limitations and advantages given a training dataset [61]. However, there are many possibilities, as DMD methods allow for predicting gaps and future behavior within the data. Figure 1.5 [62] showcases an overview of DMD on a fluid flow example and how it can be utilized in the diagnostics of trained data.

1.2 Comparison of different ignition waveforms at constant power

An important consideration in the ignition of plasma systems is the power absorption by the plasma. Depending on the ignition waveform, larger power absorption indicates a more efficient mode of operation than its counterparts. Thus, a plasma can achieve the same number density at a lower power than another plasma with a higher power load [24, 36, 63]. It is of interest to study the effects that different ignition waveforms, operating at the same power, have on the number density of the plasmas. In this instance, whether the plasma operates in the α or γ mode is secondary; the goal is to analyze and determine which ignition waveform can generate the strongest plasma.

While a direct comparison between feedstock gases is not possible due to each gas's different characteristics, it is still useful to compare different feedstock gases to gain a broad understanding of the plasma's characterization and intensity due to the parameterization of its operating parameters. This study used argon and helium feedstock gases to study the plasma characterization. Also, DBD are excluded to minimize the introduction of variables to the system. Nevertheless, studying the effects of the dielectric on plasma stability remains of interest.

For this study, parameters such as ignition waveform, feedstock gas, pressure, and reactor dimensions are fundamental to establishing a relationship within these parameters in an atmospheric-driven plasma. One of the main challenges of igniting an APGD-CCP plasma is the high power requirement due to the operating pressure [64]. The operational characterization of the plasma is challenging because of the risk of entering the γ mode of operation due to the already high voltage used within the plasma. This study aims to provide insights into balancing power input and the mode of operation, dependent on the feedstock gas and the ignition waveform.

1.3 Study of the critical point of operation for different ignition waveforms for an argon plasma

While the preceding study provided insights into the mode of operation and number density generated as a result of constant input power, it does not address the operational criticality for each waveform utilized, i.e., the transition point between a plasma in the α mode of operation to one in the γ mode of operation. Therefore, it is of interest to determine operational criticality to establish the maximum reactivity the plasma can achieve before instabilities appear within the system. In this case, only argon was studied due to its immediate interest and low cost of operation, which promises widespread adoption compared to helium [56, 58] . Additionally, the effects of integrating a dielectric into the system are studied to determine whether

the waveform's operational efficiency and reactivity increase due to the presence of dielectrics [58].

Moreover, compared to the preceding study where a power-coupled algorithm was utilized to match the power of the plasma to that of a user-specified power, an external circuit algorithm is now coupled to the model. This ensures the simulation accounts for the impedance losses found in a power supply and the transition between α and γ modes of operation, where input voltage decreases compared to its critical value as the differential conductivity of the plasma becomes negative [39]. Building on the previous study's findings, this research aims to provide a comprehensive understanding of APGD-CCP and DBD-RF plasma characterization, to maximize reactivity in the system while maintaining stable plasma operation.

1.4 Utilization of DMD for prediction of intermediate data

One of the challenges encountered in previous studies was the large data generation and post-processing requirements, which resulted in significant time and computational overhead due to the number of simulations needed for a comprehensive analysis of plasma characterization. Additionally, because pulsed waveforms have advantages over other types of waveforms, it is of interest to parameterize and study these phenomena using Gaussian waves. These waveforms allow granular control of the plasma profile in the reactor. However, studying all possible cases is impractical due to the large amount of data required.

DMD offers a solution to this problem. DMD is a data-driven algorithm that decomposes complex dynamical systems into spatiotemporal modes, providing insights into the system's behavior. Initially developed for fluid dynamics [65], DMD has expanded into various fields [61]. By approximating linear dynamics that best fit the observed data, DMD extracts dominant modes that capture the system's essential features. DMD's data-agnostic nature makes it particularly suited for handling large datasets, as it relies on the data to uncover patterns and dynamics rather than specific physical models [62]. This flexibility allows researchers to explore a wide range of behaviors and operational scenarios efficiently.

DMD can be utilized to significantly reduce computational overhead in plasma research by predicting plasma behavior under different conditions without extensive simulations. Training the DMD model on a subset of data allows it to predict the plasma's response to untested parameter sets, saving resources and accelerating the research process. This method provides quick insights into the effects of various parameters, optimizing the system's performance while maintaining stability.

1.5 Goals and objectives

The utilization of glow discharges has dominated low-pressure systems due to the large characteristic lengths of particles at such pressures, allowing for isotropic processing of surfaces in various semiconductor industry applications. However, while APGD-CCP may not be suitable for state-of-the-art semiconductor processes, numerous potential applications still need to be explored. These include decontamination of surfaces where filamentary discharges might cause damage, medical applications where glow discharges may be less invasive, and areas where replacing filamentary discharges could benefit the lifespan of reactors, such as ozone generation. A significant challenge in utilizing APGD-CCP discharges lies in the high-power requirements due to the pressure-distance relationship, making the parametrization of operating conditions difficult. APGD-CCP plasmas are highly sensitive to the driven potential, leading to an inherently unstable system that can exhibit constriction and arcing, defeating the purpose of using APGD-CCP. Although several studies have demonstrated the benefits of different feedstock gases and waveforms in maximizing plasma intensity while minimizing instability, a comprehensive parametric study still needs to be completed on the behavior of feedstock gases and waveforms used to ignite the plasma. The main objective of this research is to provide a comprehensive understanding of the differences between feedstock gases and driven waveforms. It seeks to determine whether different feedstock gases dramatically change the plasma profile and whether certain waveforms can drive the plasma to higher intensity while maintaining stability, thus allowing for lower operational power and adequate number density for specific applications. Two feedstock gases will be studied — helium and argon plasmas. Helium, known for its ease of ignition, serves as a comparative basis. Conversely, argon has a lower operating cost and offers the potential for scalability in various processes of interest.

Another point of interest, from a modeling perspective, is the significant computational overhead in obtaining results due to the complexity of the plasma medium. Given the parametrized nature of these studies, computational downtime can hinder the application of obtained results in potential applications. Therefore, it is essential to investigate the feasibility of data-driven techniques such as DMD. This approach could yield results approximating those from running a simulation but with minimal computational overhead. Such advancements in reducing computational overhead would accelerate the development of novel technologies, enabling quicker access to results than traditional simulation methods.

1.6 Executive summary

The main objectives of this research can be summarized as follows:

- Study APGD-CCP for argon and helium plasmas under different waveforms at

constant power input to determine which waveform can ignite a plasma with the highest intensity.

- Determine the critical point of operation within the stable and unstable modes of operation, i.e., α and γ modes, for the different waveforms utilized in both APGD and DBD-RF modes.
- Investigate the effects of integrating dielectric materials into the system to determine whether their presence enhances the operational efficiency and reactivity of the plasma.
- Examine the influence of different feedstock gases, specifically argon and helium, on plasma characterization and performance.
- Evaluate the high power requirements and operational challenges associated with igniting APGD-CCP plasmas, focusing on balancing power input and maintaining stable operation.
- Provide a comprehensive understanding of APGD-CCP and DBD-RF plasma characterization, with the goal of optimizing plasma reactivity while maintaining stability.
- Analyze the application of Gaussian waveforms for granular control of the plasma profile and their potential advantages over other waveform types.
- Study the feasibility of utilizing machine learning algorithms such as DMD to predict data from a training dataset, aiming to reduce computational overhead and accelerate the research process.

The following subsections will discuss in detail the findings related to the different objectives of this research, providing a comprehensive analysis of the plasmas studied and the characterization of these systems.

Chapter 2

Basic plasma equations and equilibrium

2.1 Governing equations

The plasma medium is difficult to simulate due to its stochastic nature and the varying time frames of its parameters. Lieberman [66] describes the problem: a distribution function $f(\mathbf{r}, \mathbf{v}, t)$ is introduced for a given species in the six-dimensional phase space $(\mathbf{r}, \mathbf{v})$ of particle positions and velocities. The distribution function is defined as the number of particles within a spatial volume, where $\mathbf{r}$ denotes the position vector and $\mathbf{v}$ represents the particle velocity.

$$f(\mathbf{r}, \mathbf{v}, t) d^3r d^3 = \text{number of particles inside a six-dimensional phase space volume } d^3r d^3v \text{ at } (\mathbf{r}, \mathbf{v}) \text{ at time } t.$$

The six coordinates $(\mathbf{r}, \mathbf{v})$ are considered independent variables. Figure 2.1 shows a fixed differential volume dx, $\mathrm{dv_x}$ simplified in one dimension to solve the fluxes entering and exiting the fixed differential volume. The Boltzmann equation is obtained by deriving and solving the fluxes of the differential volume and accounting for the collision term for a given species.

$$\frac{\partial f}{\partial t} + \mathbf{v} \cdot \nabla_{\mathbf{r}} f + \frac{\mathbf{F}}{m} \cdot \nabla_{\mathbf{v}} f = \left. \frac{\partial f}{\partial t} \right|_c \tag{2.1}$$

Here, the function f denotes the number of particles within a spatial volume, $\mathbf{v}$ represents the particle velocity, and $\mathbf{F}$ represents the force exerted on the particle. The variable m signifies the particle mass, ∇_r indicates the vector gradient, and ∇_v corresponds to the velocity gradient. The left-hand side of the equation is derived from the solution of the collisionless Boltzmann equation, while the right-hand side embodies the collision term. The continuity equation can be obtained by integrating

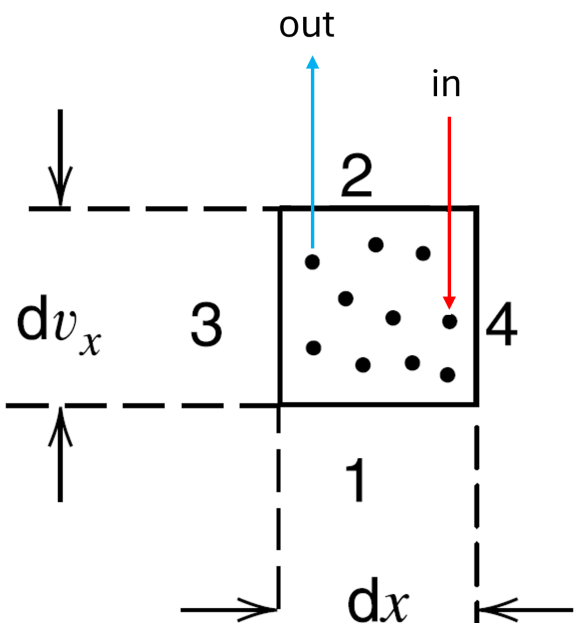

Figure 2.1: One-dimensional $v_x - x$ phase space, illustrating the derivation of the Boltzmann equation and the change in f due to collisions [66].

the Boltzmann equation over velocity space. However, to solve the plasma problem as a fluid continuum, the Boltzmann equation distribution properties must be averaged to obtain equations depending on the spatial coordinates and time only, as seen in equation 2.2 and 2.3. The Boltzmann equation can be expressed as a macroscopic continuity equation by integrating the distribution function and particle velocity, as shown in equation 2.4.

$$n(\mathbf{r}, t) = \int f d^3v \tag{2.2}$$

$$\Gamma(\mathbf{r}, t) = n\mathbf{u} = \int \mathbf{v} f d^3v \tag{2.3}$$

$$\frac{\partial n}{\partial t} + \nabla \cdot (n\mathbf{u}) = G - L \tag{2.4}$$

The variable n signifies the average particle density, **u** represents the mean velocity, and G and L denote the particle gains and losses, respectively. When macroscopic transport is not considered [67], the continuity equation's source and loss terms can be calculated as gains and losses from the chemical reactions themselves as seen in equation 2.5.

$$\omega_i = k_{fi} \prod_k [X]_k^{v'_{ki}} - k_{ri} \prod_k [X]_k^{v''_{ki}} \tag{2.5}$$

The sources and losses for reactions are calculated as follows: k_{fi} and k_{ri} are the forward and reverse reaction rates, v'_{ki} and v''_{ki} are the stoichiometric coefficients, and X is the molar concentration of species k. The total gains and losses are calculated by summing all the sources and losses from all the reactions where species i is present. Further expansion of the continuity equation gives rise to the momentum equation. For readers interested in the intricate details of the momentum equation's derivation, we direct them to the work of Krall and Trivelpiece [68].

$$mn\left(\frac{\partial \mathbf{u}}{\partial t} + (\mathbf{u}\cdot\nabla)\mathbf{u}\right) = en(\mathbf{E} + \mathbf{u}\times\mathbf{B}) - \nabla\cdot\Pi + \mathbf{f}\Big|_c \tag{2.6}$$

Where e signifies the electric charge, $\mathbf{E}$ represents the electric field, $\mathbf{B}$ denotes the magnetic field, and Π corresponds to the pressure tensor. For weakly ionized plasmas, the pressure tensor simplifies to a pressure gradient ∇p. The magnetic term $\mathbf{B}$, exerting minimal effects on the plasma studied in this paper, is omitted for practicality. The term $\mathbf{f}$ describes the momentum transfer per unit volume due to collisions with other species. One can derive the energy conservation equation by multiplying the Boltzmann equation by $\frac{1}{2}mv^2$ and then integrating over velocity. Subsequent integration and mathematical manipulations yield the energy equation.

$$\frac{\partial}{\partial t}\left(\frac{3}{2}p\right) + \nabla\cdot\frac{3}{2}(p\mathbf{u}) + p\nabla\cdot\mathbf{u} + \nabla\cdot\mathbf{q} = \frac{\partial}{\partial t}\left(\frac{3}{2}p\right)\Big|_c \tag{2.7}$$

The term $(\frac{3}{2}\mathrm{p})$ denotes the thermal energy density, while $(\frac{3}{2}\mathrm{p}\mathbf{u})$ represents the macroscopic thermal energy flux, characterizing the flow of thermal energy density at the fluid velocity. The term $\mathrm{p}\nabla\cdot\mathbf{u}$ accounts for the heating of the fluid due to compressibility, and $\mathbf{q}$ represents the heat vector flow, contributing to the macroscopic thermal energy flux. The right-hand side of the equation addresses the generation and loss of species' thermal energy. As the plasma is a multiphysics problem driven by an electrical source, it is necessary to describe the electrical distribution within the plasma. To characterize the electrical properties of the plasma, the Maxwell equations are solved to obtain the poisson equation, assuming negligible magnetic effects. The equations are as follows

$$\nabla\times\mathbf{E} = -\mu_0\frac{\partial \mathbf{H}}{\partial t} \tag{2.8}$$

$$\nabla\times\mathbf{H} = \epsilon_0\frac{\partial \mathbf{E}}{\partial t} + \mathbf{J} \tag{2.9}$$

$$\epsilon_0 \nabla \cdot \mathbf{E} = \rho \tag{2.10}$$

$$\epsilon_0 \nabla \cdot \mathbf{H} = 0 \tag{2.11}$$

$\mathbf{E}(\mathrm{r}, \mathrm{t})$ and $\mathbf{H}(\mathrm{r}, \mathrm{t})$ are the electric and magnetic field vectors, and μ_0 and ϵ_0 are the permeability and permittivity of free space. The charge continuity equation relates the field sources, the charge density $\rho(\mathrm{r}, \mathrm{t})$, and the current density $\mathbf{J}(\mathrm{r}, \mathrm{t})$. By combining the charge continuity equation, equation 2.12 and the Maxwell equations, equations 2.8, 2.9, 2.10, and 2.8, the following equation is obtained represented in equation 2.13.

$$\frac{\partial \rho}{\partial t} + \nabla \cdot \mathrm{J} = 0 \tag{2.12}$$

$$\nabla \cdot \mathrm{E} = \frac{\rho}{\epsilon_0} \tag{2.13}$$

In the case a dielectric element is present, the following equation calculates the charge accumulation of electrons and ions is given as [55]

$$\frac{d\sigma_e}{dt} = n \cdot \Gamma_e \tag{2.14}$$

$$\frac{d\sigma_i}{dt} = \alpha_s (1 + \gamma_{SEE}) n_i \mu_i E \cdot n - \min(\sigma_e, \sigma_i) \tag{2.15}$$

where the function $\min(\sigma_\mathrm{e}, \sigma_\mathrm{i})$ compares the values of σ_e and σ_i returns the value of the smallest one. The field generated due to the accumulation of charge on the dielectric is calculated using

$$n(D_1 - D_2) = \rho_s \tag{2.16}$$

Where ρ_s is the net charge density of the dielectric surface and D_1 and D_2 are the electric displacement fields above and below the boundary. Within somaFOAM, the continuity, momentum, and energy equations are adapted, simplified, and resolved using a segregated approach. Leveraging the drift-diffusion approximation [66] further streamlines the problem, eliminating the need to solve the momentum equation directly. The equations employed in somaFOAM, starting with the drift-diffusion approximation, are presented below.

$$\mathbf{\Gamma} = \pm \mu n \mathbf{E} - D \nabla n \tag{2.17}$$

$$D = \mu \frac{k_b T}{e} \tag{2.18}$$

Here, $\mathbf{\Gamma}$ represents the particle flux, μ denotes the mobility coefficient, and D is the diffusion coefficient, with k_b representing the Boltzmann constant and T the species' temperature. The introduction of the drift-diffusion approximation necessitates alterations to the continuity equation. The modified equation is presented below and defined as follows

$$\frac{\partial n}{\partial t} + \nabla \cdot \mathbf{\Gamma} = G - L \tag{2.19}$$

In the case of the electron energy equation, the following form is adopted [69]

$$\frac{3}{2} k_B n_e T_e + \nabla \cdot \mathbf{q_e} = e\mathbf{\Gamma_e} \cdot \mathbf{E} + Q_e + \sum_j R_{je} \Delta H_e \tag{2.20}$$

Where q_e represents the electron energy flux, Q_e denotes the electron energy loss due to elastic collisions, and the summation of R_{je} multiplied by ∇H_e signifies the electron energy gain from inelastic collisions. In this context, R_{je} denotes the rate coefficient for the inelastic collision of electrons with species j. ∇H_e symbolizes the corresponding energy exchange, corresponding to the energy threshold needed for the electron to initiate the reaction. Both q_e and Q_e are further decomposed as follows

$$\nabla \cdot \mathbf{q_e} = \nabla \cdot \left(\frac{5}{2} k_B T_e \mathbf{\Gamma_e} \right) - \left(\frac{5}{2} n_e D_e \right) \nabla^2 T_e \tag{2.21}$$

$$Q_e = 3 \frac{m_e}{M} n_e \nu_{en} (T_e - T_g) \tag{2.22}$$

Where M represents the mass of the background gas, ν_{en} denotes the electron-neutral momentum transfer frequency, and T_g corresponds to the background gas temperature. ν_{en} can be defined as follows:

$$\nu_{en} = \frac{|e|}{m_e \mu_e} \tag{2.23}$$

Considering the benchmark models for this paper, ions' contributions to the background temperature are omitted because ion contributions are negligible in non-thermal, stable atmospheric plasmas. While the background gas temperature is important in practical applications, such analysis is beyond the scope of this paper. The drift-diffusion model was selected for its simplicity and because both benchmark models employ the drift-diffusion approximation.

2.2 Boundary conditions

Boundary conditions for the species number density, voltage, and electron temperature are prescribed as follows. Unless noted otherwise, these boundary conditions are

sourced from Hagelaar [70, 71]. The boundary conditions for ions, excited states, and ground states are as follows.

$$\nabla n_i = 0 \tag{2.24}$$

A flux boundary condition is utilized to close the continuity equation for the electrons. The electron number density boundary condition is presented below.

$$\mathbf{\Gamma_e} = \frac{1}{4} n_e \sqrt{\frac{8 k_B T_e}{\pi m_e}} \mathbf{n} + (a-1)\mu_e \mathbf{E} n_e - a \sum_k \gamma_{se,k} \mathbf{\Gamma_{i,k}} \tag{2.25}$$

γ_{se} denotes the SEE coefficient, and $\mathbf{\Gamma_{i,k}}$ represents the ion flux towards the electrodes. The coefficient a is a Boolean value indicating whether $\mathbf{E}$ is directed towards the electrodes (having a value of 1) or not (having a value of 0). The vector $\mathbf{n}$ represents the normal unit directed towards the boundary. The impact of ions on the electrode surface causes a dislocation from the electrode, effectively acting as a source for electrons. However, not every collision produces an electron, as the generation of an electron due to ion collision with the electrode walls is contingent upon the SEE coefficient. The ion flux boundary condition is presented as follows, resembling the electron boundary condition except for the SEE [69].

$$\mathbf{\Gamma_i} = \frac{1}{4} n_i \sqrt{\frac{8 k_B T_i}{\pi m_i}} \mathbf{n} + a \mu_i \mathbf{E} n_i \tag{2.26}$$

A modified version of equation (2.25) is utilized for the electron energy equation.

$$\mathbf{\Gamma}_\epsilon = \left(\frac{5}{2} k_B T_e\right) \left[\frac{1}{4} n_e \sqrt{\frac{8 k_B T_e}{\pi m_e}}\right] - \left(\frac{5}{2} k_B T_{se}\right) \sum_k \gamma_{se,k} \mathbf{\Gamma_{i,k}} \tag{2.27}$$

For the voltage boundary condition, 0 V (ground) is assigned to the mesh's left electrode. A power-regulating algorithm adjusts the voltage in each cycle for the right electrode, ensuring that the simulated power aligns with a specified time-averaged power. This configuration was utilized to benchmark the results obtained from somaFOAM against the benchmark cases. Other simulation parameters, such as pressure and background gas temperature, are kept constant.

Chapter 3

Finite volume method and somaFOAM

3.1 Application of finite volume method in somaFOAM

The solution of plasma phenomena requires a discretized approach, as plasma equations are very difficult to solve analytically [72]. While some cases are solvable with many assumptions to simplify the problem, these mathematical methods demand an advanced understanding of mathematics [66]. However, most plasma problems fall outside the scope of these assumptions, necessitating numerical tools to represent plasma physics accurately. Many commercial solvers, such as COMSOL [73], Star-CCM+ [74], and PLASIMO [75], have libraries capable of solving nonthermal plasma problems. However, utilizing these libraries often requires paying additional fees on top of those for the base software, making access to such software suites impractical for many.

Moreover, the closed-source nature of these software packages prevents researchers from modifying the source code to meet their specific needs, forcing them to rely on the vendor to implement desired algorithms. This may involve additional fees or waiting for software release cycles, with no guarantee that the requested features will be included. These limitations hinder research endeavors, making the use of commercial platforms less prudent. On the other hand, developing a numerical suite from scratch is a time-consuming process. Creating boilerplate code takes significant time before any tailored development for studying plasma phenomena can begin. Furthermore, while this approach allows for minute control over the modeling code, choosing a programming baseline becomes challenging. Compiled languages like C++, Rust, and C offer fast execution times but can be cumbersome to develop [76, 77, 78]. Conversely, interpreted languages like Python and MATLAB enable quick implementation of algorithms but at the cost of time overhead due to their interpreted nature [79].

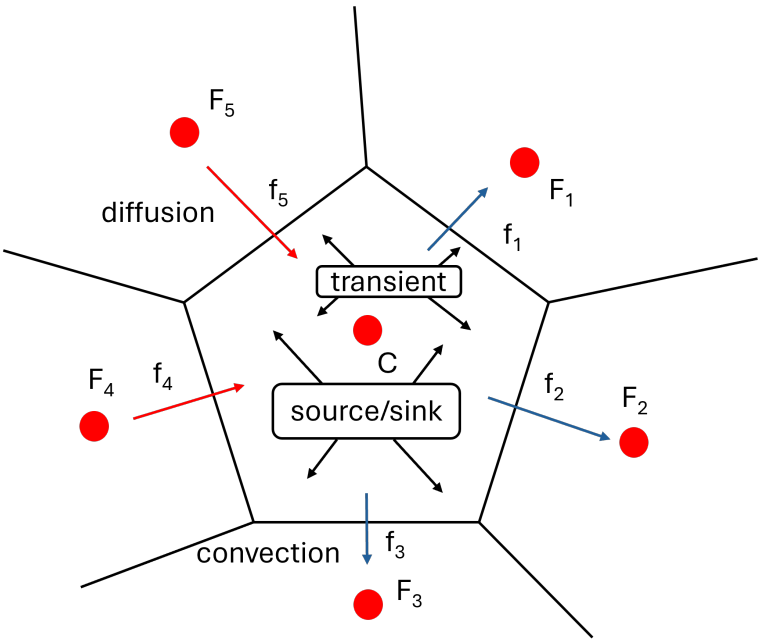

Figure 3.1: Conservation of a discrete element utilizing a FVM approach.

OpenFOAM, an open-source numerical toolbox based in C++, provides a substantial amount of boilerplate code to comprehensively develop numerical algorithms in a compiled language. Originally developed as a computational fluid dynamics (CFD) code utilizing a object-oriented approach [80], it has become the numerical toolbox of choice for developing algorithms utilizing the finite volume method (FVM) for different complex physics phenomena [81]. The FVM, based on the control volume formulation, divides the solution domain into control volumes (cells within a mesh), where the variable of interest in each cell is the average with respect to the control volume stored in the centroid of the finite volume element [82]. Figure 3.1 showcases the control volume formulation of the FVM. The FVM is conservative as the flux entering a given control volume is identical to the flux leaving it [83].

$$\int_{V_P} \nabla \cdot (\rho \mathbf{u} \phi) dV = \oint_{\partial V_P} d\mathbf{S} \cdot (\rho \mathbf{u} \phi) = \sum_f \mathbf{S}_f \cdot (\rho \mathbf{u} \phi)_f \tag{3.1}$$

$$\int_{V_P} \nabla \cdot (\rho \Gamma_\phi \nabla \phi) dV = \oint_{\partial V_P} d\mathbf{S} \cdot (\rho \Gamma_\phi \nabla \phi) = \sum_f \mathbf{S}_f \cdot (\rho \Gamma_\phi \nabla \phi)_f \tag{3.2}$$

$$\int_{V_P} S_\phi(\phi) dV = S_c V_P + S_P V_P \phi_P \tag{3.3}$$

```
tmp<fvScalarMatrix> NEqn
(
    fvm::ddt(Ni)
        + fvm::div((fvc::interpolate(F_[i]) & mesh_.Sf()), Ni, "div(F,Ni)")
    - fvm::laplacian(D_[i], Ni, "laplacian(D,Ni)")
    - chemistry.RR(i)*plasmaConstants::A/W(i)
    + chemistry.dRRDi(i)*Ni
    - fvm::Sp(chemistry.dRRDi(i),Ni)
);

solverPerf = NEqn->solve(mesh_.solutionDict().solver("Ni"));
```

Figure 3.2: Code snippet in somaFOAM syntax describing the continuity equation.

$$(\nabla\phi) = \frac{1}{V_P}\sum_f (\mathbf{S}_f\phi_f) \tag{3.4}$$

To discretize the partial differential equation using the FVM, the governing equations are integrated over a differential volume integral, where the volume integrals are converted to surface integrals using Gauss's theorem [84]. The surface integral is approximated using the midpoint rule, resulting in a summation of the convective, diffusive, source, and gradient terms as seen in equations 3.1, 3.2, 3.3 and 3.4 for the transport equation correlating the centroids of the control volume to the surface faces of the centroids [82, 85]. For the source term, S_c is the constant part of the source term, while for S_p is the non-linear part of the source term. For a transport equation, all the terms are combined as seen in equation 3.5.

$$\int_{V_P} \frac{\partial\rho\phi}{\partial t} dV + \sum_f \mathbf{S}_f \cdot (\rho\mathbf{u}\phi)_f + \sum_f \mathbf{S}_f \cdot (\rho\Gamma_\phi \nabla\phi)_f = S_c V_P + S_P V_P \phi_P \tag{3.5}$$

To advance the solution in time, a time integral is applied such as shown in equation 3.6, where the time derivative and the implicit source integral is expanded further in equation 3.7, 3.8, 3.8 and 3.10.

$$\begin{aligned}\int_t^{t+\Delta t} \left[\left(\frac{\partial\rho\phi}{\partial t} \right)_P V_P + \sum_f \mathbf{S}_f \cdot (\rho\mathbf{u}\phi)_f + \sum_f \mathbf{S}_f \cdot (\rho\Gamma_\phi \nabla\phi)_f \right] dt \\ = \int_t^{t+\Delta t} (S_c V_P + S_P V_P \phi_P) dt\end{aligned} \tag{3.6}$$

$$\left(\frac{\partial\rho\phi}{\partial t} \right)_P = \frac{\rho_P^n \phi_P^n - \rho_P^o \phi_P^o}{\Delta t} \tag{3.7}$$

Table 3.1: Partial entities for `fvm` or `fvc` class functions in OpenFOAM.

Term description	Implicit/Explicit	Test Expression	fvm::/fvc:: functions
Laplacian	Imp/Exp	$\nabla^2\phi$	laplacian(phi)
		$\nabla \cdot \Gamma\nabla\phi$	laplacian(Gamma, phi)
Time derivative	Imp/Exp	$\frac{\partial\phi}{\partial t}$	ddt(phi)
		$\frac{\partial\rho\phi}{\partial t}$	ddt(rho, phi)
Second time derivative	Imp/Exp	$\frac{\partial}{\partial t}(\rho\frac{\partial\phi}{\partial t})$	d2dt2(rho, phi)
Convection	Imp/Exp	$\nabla \cdot (\psi)$	
		$\nabla \cdot (\psi\phi)$	div(psi, phi)
Divergence	Exp	$\nabla \cdot \chi$	div(chi)
Gradient	Exp	$\nabla\chi$	
		$\nabla\phi$	grad(chi)
Curl	Exp	$\nabla \times \phi$	curl(phi)
Source	Imp	$\rho\phi$	Sp(rho,phi)
	Imp/Exp		SuSp(rho,phi)

$$\int_t^{t+\Delta t} \phi(t)dt = \frac{1}{2}(\phi^o + \phi^n)\Delta t \tag{3.8}$$

$$\phi^n = \phi(t) + \Delta t \tag{3.9}$$

$$\phi^0 = \phi(t) \tag{3.10}$$

OpenFOAM provides a database of different discretization schemes [85], allowing for ease of implementation since they are part of OpenFOAM's boilerplate code. OpenFOAM syntax, tailored towards solving FVM problems, is very similar to a symbolic representation of the partial differential equation of interest, allowing for ease of implementation [86]. For instance, the continuity equation's form in somaFOAM as shown in figure 3.2 is similar to its symbolic representation. Partial differential equations in OpenFOAM are solved by storing the equation in classes `fvScalarMatrix` or `fvVectorMatrix`, depending on whether the equation is scalar or vector. The functions within the continuity equation, `fvm`, and `fvc`, specify whether the terms are solved explicitly or implicitly. Table 3.1 specifies the different discretization schemes as function of `fvm` or `fvc` depending on the case use. After the matrix is set up,

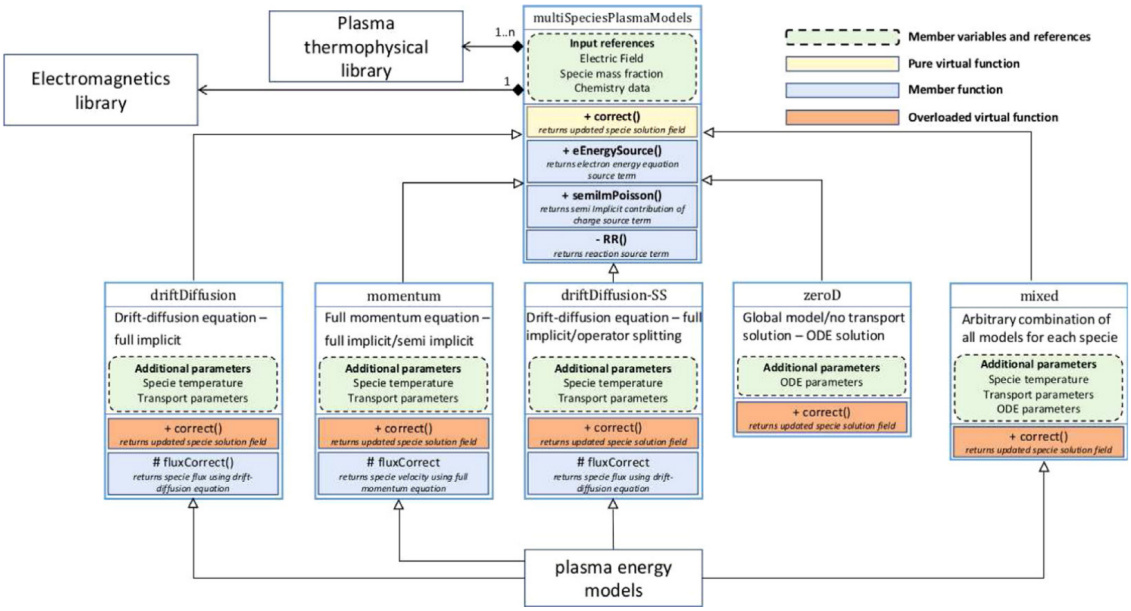

Figure 3.3: UML diagram showcasing the relationship of different libraries in SOMAFOAM [89].

relaxation factors are applied to make the matrix diagonally dominant, reducing instabilities in the solution. The `solve()` function is executed to solve the matrix of the constituent partial differential equation.

Equations encompassing the plasma problem are solved in somaFOAM, an in-house plasma solver based on OpenFOAM developed for solving plasma phenomena. Access to the code, installation instructions, and sample cases are available as reference [87]. The governing equations for plasmas are solved in a segregated manner [88], first solving the continuity equation (which requires solving the source and sink terms of the chemical reactions, handled by the plasma thermophysical library), then solving the drift-diffusion approximation to solve the energy equation, and finally solving the Poisson equation in conjunction with the dielectric, if present, iteratively until the problem is solved. This process continues to the next time step until a user-defined end time completes the simulation. A unified modeling language (UML) diagram, as seen in figure 3.3 and provided by somaFOAM original paper [89], provides insights into the relationship between the different libraries within somaFOAM necessary to solve the plasma problem. Since plasma problems are complex multiphysics problems, a large number of libraries solving different physical parameters are required.

3.2 Discretization schemes for governing equations

In somaFOAM, `fvm` is employed, converting the volume integral into a surface integral. The keyword `Gaussian` must be specified before utilizing any scheme of interest per part of somaFOAM syntax.

$$\int_V \nabla \cdot \mathbf{a} dV = \oint_{\partial V} d\mathbf{S} \cdot \mathbf{a} \tag{3.11}$$

A central differencing scheme, named `linear` in OpenFOAM, is utilized for gradient schemes. This scheme is derived from approximating the integral using the midpoint rule, summing the surface elements, and rearranging the elements as needed. The accompanying equation 3.15 and diagram 3.4 showcases the discretization and stencil of the central differencing scheme. f_x represents the interpolation factor defined as the ratio of distances $\overline{fN}$ and $\overline{PN}$ as seen in equation 3.13.

$$\phi_f = f_x \phi_P + (1 - f_x)\phi_N \tag{3.12}$$

$$f_x = \frac{\overline{fN}}{\overline{PN}} \tag{3.13}$$

A linear limited (`linearLimited`) scheme is employed for divergence schemes, combining both the upwind and the linear schemes. The upwind scheme is defined as seen in equation 3.14 and stencil represented in figure 3.5

$$\phi_f = \begin{cases} \phi_f = \phi_P, & \overset{\circ}{F} \geq 0 \\ \phi_f = \phi_N, & \overset{\circ}{F} \leq 0 \end{cases} \tag{3.14}$$

The implementation of the `linearLimited` scheme is done by utilizing a Sweby limiter as seen in equation 3.14, coupling a first-order scheme to a correction factor, Ψ, to increase the accuracy of the solution while minimizing the oscillatory behavior encountered in central differencing schemes for divergence schemes.

$$\phi_f = \phi_{UD} + \Psi[(\phi)_{CD} - (\psi)_{UD}] \tag{3.15}$$

Where ϕ_{UD} represented the solution of the upwind scheme and ϕ_{CD} the solution of the central difference scheme. Since the cases studied are one-dimensional and orthogonal, the discretization of the gradient in the diffusion term is performed in somaFOAM with a central difference scheme as seen in equation 3.15 with the orthogonality represented in figure 3.6, which is the default in all the studies performed.

An Euler time discretization is utilized to determine both value ϕ and value $\nabla\phi$. Equations 3.16 and 3.17 showcases the implementation of the euler implicit method

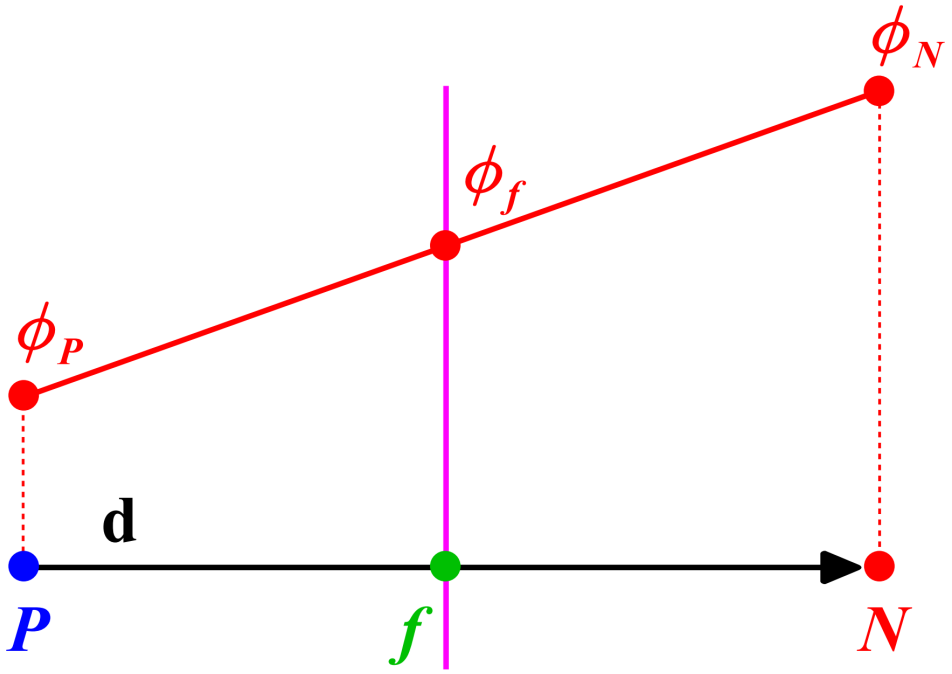

Figure 3.4: Stencil of the central differencing scheme.

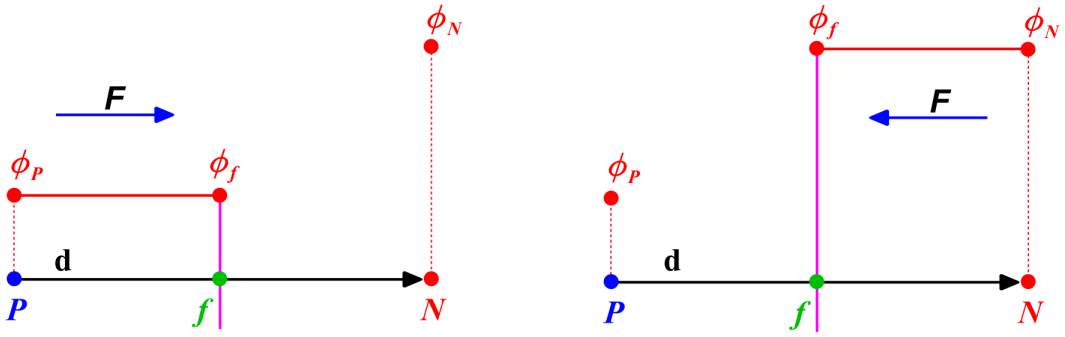

Figure 3.5: Stencil of the upwind scheme.

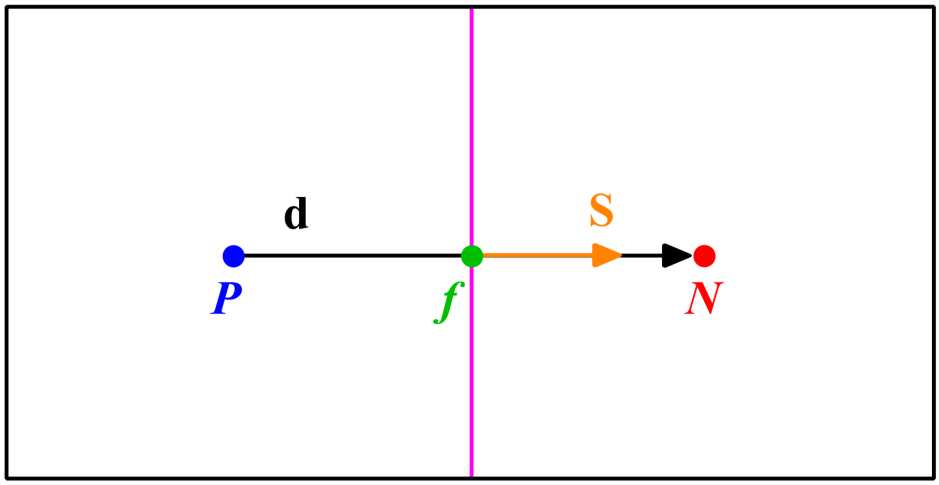

Figure 3.6: Orthogonality in the diffusive term.

$$\phi_f = f_x \phi_P^n + (1 - f_x)\phi_N^n \tag{3.16}$$

$$\mathbf{S}(\nabla\phi)_f = \Delta \frac{\phi_N^n - \phi_P^n}{\mathbf{d}} \tag{3.17}$$

As the equations are assembled, matrix-solving techniques such as BiCGStab and BICCG are utilized alongside matrix preconditioners to speed up the convergence of the matrix being solved [90]. This approach ensures that the numerical solution of the plasma governing equations is accurate and efficient, leveraging various discretization schemes to handle the complexities of plasma behavior.

3.3 Implementation of plasma boundary conditions in somaFOAM

As the partial differential equations are solved, boundary conditions must be provided. A zero-gradient boundary condition is applied for the neutral species, equating the value of the adjacent cell to the boundary condition. For the active species, the continuity and energy equations for electrons implement mixed boundary conditions. This dictates that the boundary operates as a Dirichlet or Neumann boundary condition based on the calculated ratio, with 1 indicating a Dirichlet boundary condition and 0 signifying a Neumann boundary condition. A sample boundary condition in figure 3.7 considering the heat transfer problem is shown, representing convection heat transfer

in a wall and elucidating how such conditions are implemented within somaFOAM. The following equations for conduction and convection are given as follows:

$$\mathrm{q_{conv}} = \mathrm{q_{cond}} \tag{3.18}$$

$$\mathrm{q_{conv}} = \cdot A \cdot (T_{\mathrm{inf}} - T_B) \tag{3.19}$$

$$\mathrm{q_{cond}} = \frac{\lambda}{\sigma} \cdot A \cdot (T_B - T_X) \tag{3.20}$$

where h is the convective heat transfer coefficient, λ the conductive heat transfer coefficient, A the surface area, and δ the distance from the surface to the center of the conductive element. In somaFOAM, the mixed boundary condition is defined as follows

$$X_B = f \cdot x_{ref} + (1 - f) \cdot \left[X_x + \frac{\mathrm{Grad_{ref}(x)}}{\mathrm{deltaCoeffs}} \right] \tag{3.21}$$

where $\mathrm{x_{ref}}$ is the reference value at the boundary, $\mathrm{x_x}$ is the value in the cell center, $\mathbf{Grad(X)_{ref}}$ is the reference gradient, **deltaCoeffs** is the inverse of the face-center to cell-center distance, and f is a weighted factor that defines the boundary condition type.

$$T_B = f \cdot T_{\mathrm{inf}} + (1 - f) \cdot T_x \tag{3.22}$$

$$f = \frac{1}{1 + \frac{\lambda}{h \cdot \delta}} \tag{3.23}$$

Algebraic modifications yield the final boundary condition form. As shown in equation 3.22 and 3.23. For the boundary conditions, the values are extracted for the time step being solved, after the solution is developed in time to close the solution.

3.4 Implementation of external voltage boundary conditions in somaFOAM

While the previous sections discussed the implementation of boundary conditions for the active species, the implementation of the powered boundary condition required detailed discussion, as it is not directly implemented on the electrode. Instead, two types of boundary conditions were implemented: one that directly couples the power to the plasma, and another that simulates an external circuit from a power supply with an added resistance element [39]. For the power-coupled plasma algorithm, figure 3.8 showcases a UML diagram showcase how the algorithm is integrated into somaFOAM.

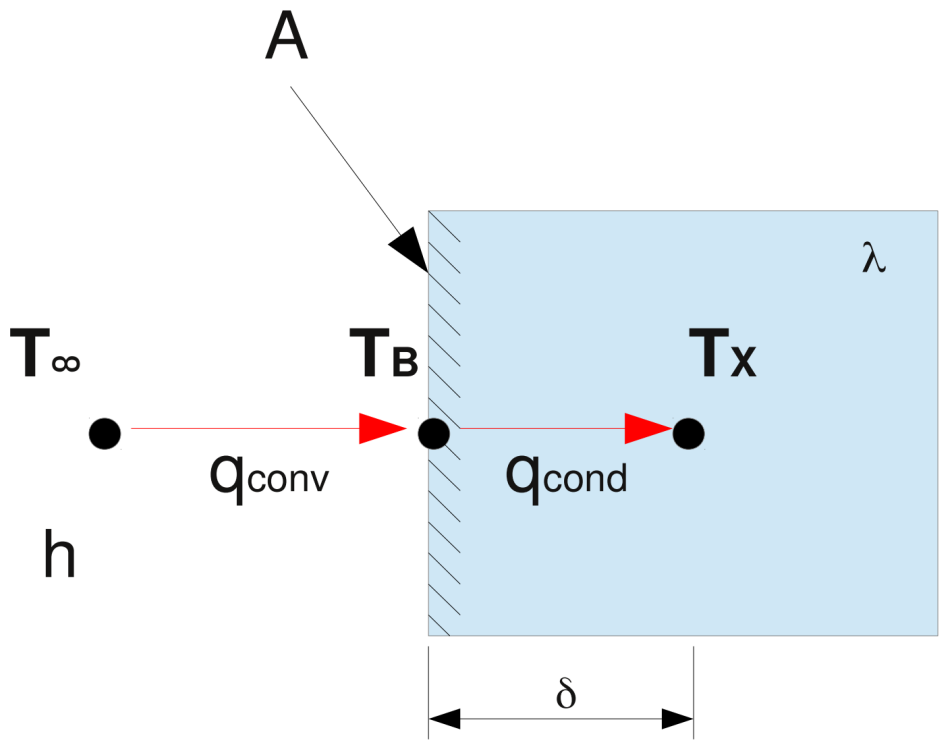

Figure 3.7: Control volume for a conduction-convection case showcasing mixed boundary conditions.

The power-coupled algorithm works for cases where the electrode is bare or in the presence of a dielectric. However, limitations exist. As the power-coupled algorithm matches the average power of the plasma per cycle to user input, it can not model the electrical characterization of the plasma because of an external power supply, which is important as the plasma intensity is a function of the external power supply. Nonetheless, such an approach is still acceptable for obtaining a general idea of the characterization of plasma at a certain power. To address this, an external circuit with a resistor representing the impedance of the external circuit is implemented to simulate a plasma system connected to an external power supply. Figures 3.9 and 3.10 show the schematic of the implementation in OpenFOAM, with equations 3.9 and 3.10 presenting the semi-discretized form of the external circuit, implemented in somaFOAM as a boundary condition. This boundary condition is implemented semi-implicitly to ensure stability in the solution.

$$J_c = \frac{1}{d}\int_0^a \sum_s q_s \Gamma_s dx \tag{3.24}$$

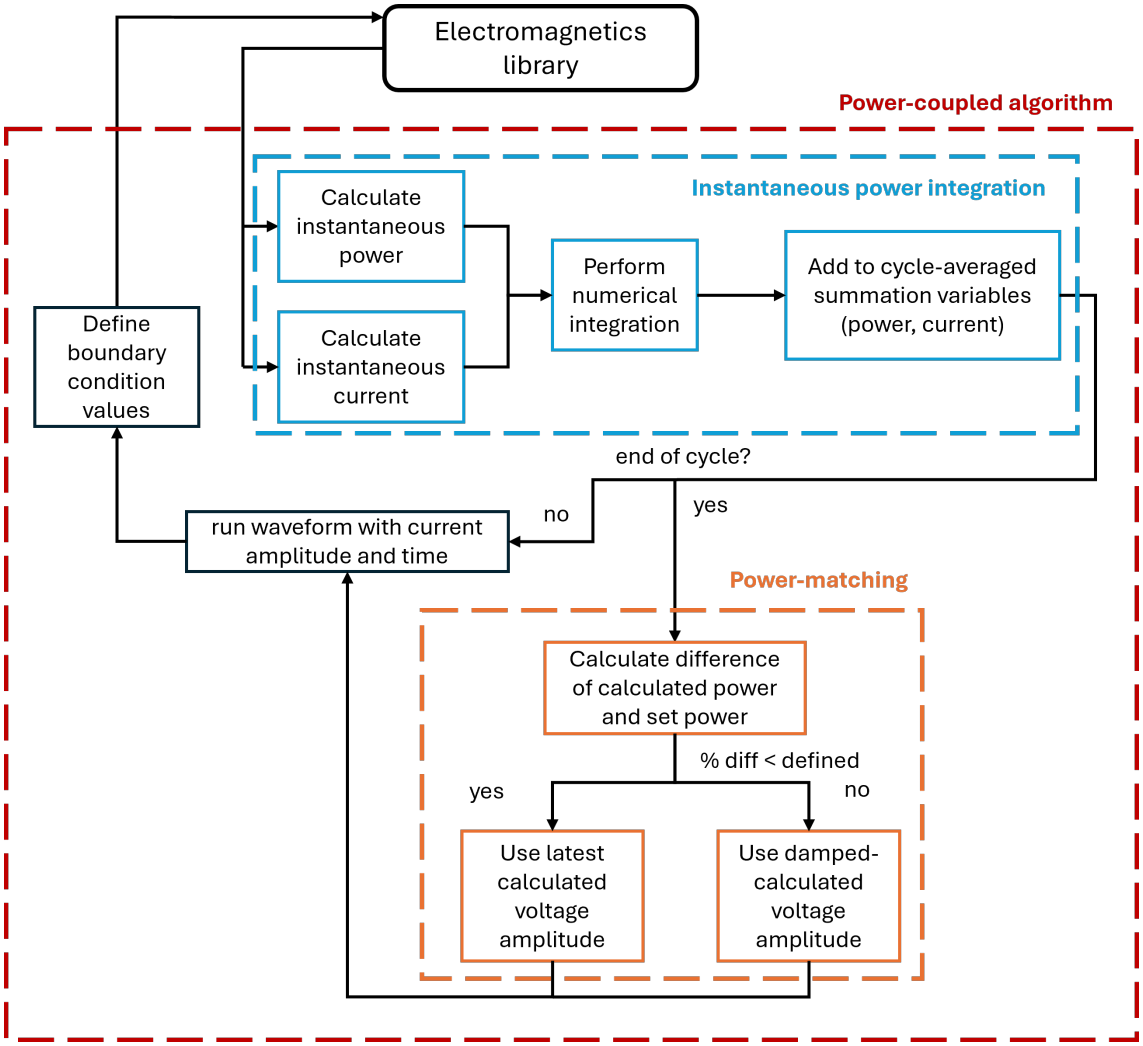

Figure 3.8: Logic diagram of the electromagnetic library within somaFOAM.

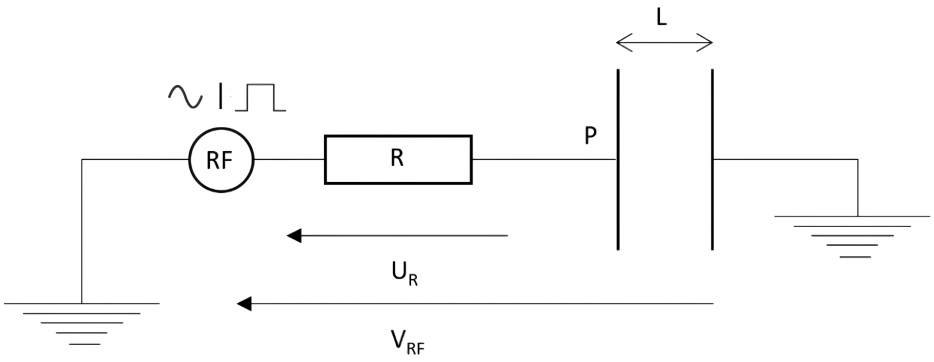

Figure 3.9: Electrical configuration of bare electrodes used to ignite argon and helium plasmas.

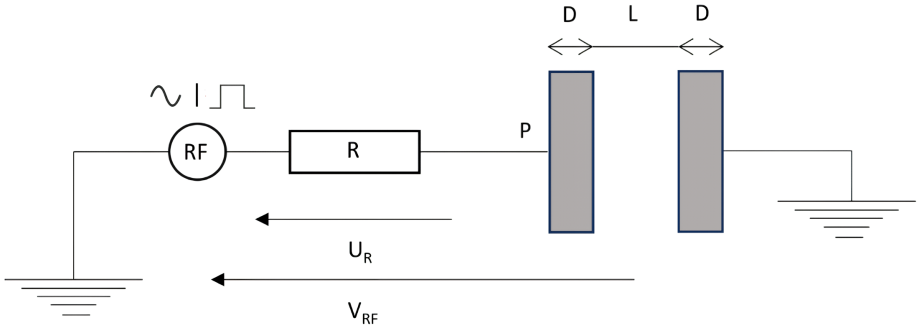

Figure 3.10: Electrical configuration of DBD used to ignite argon and helium plasmas.

$$U_R^k = (V_{rf}^k - P^k)/\left(1 - \frac{L\Delta t}{\epsilon_{eq} R}\right) \tag{3.25}$$

$$P^{k+1} = P^k + (U_R^k - RJ_c^k)\frac{L\Delta t}{\epsilon_{eq} R} \tag{3.26}$$

For the first study, which examines the influence of power in helium and argon plasmas using different ignition waveforms, the power-coupling algorithm is used. For the follow-up study to determine the critical point of operation and the study where a training dataset is utilized for the DMD algorithm, the external circuit is used by default as it provides a more accurate modeling of the plasma.

The different waveforms used are shown in figure 3.11 for the first and second studies, with the third study superimposing a sinusoidal waveform with a Gaussian waveform with a duty cycle of 10%, as shown in figure 3.12. Equations 3.27 and 3.28

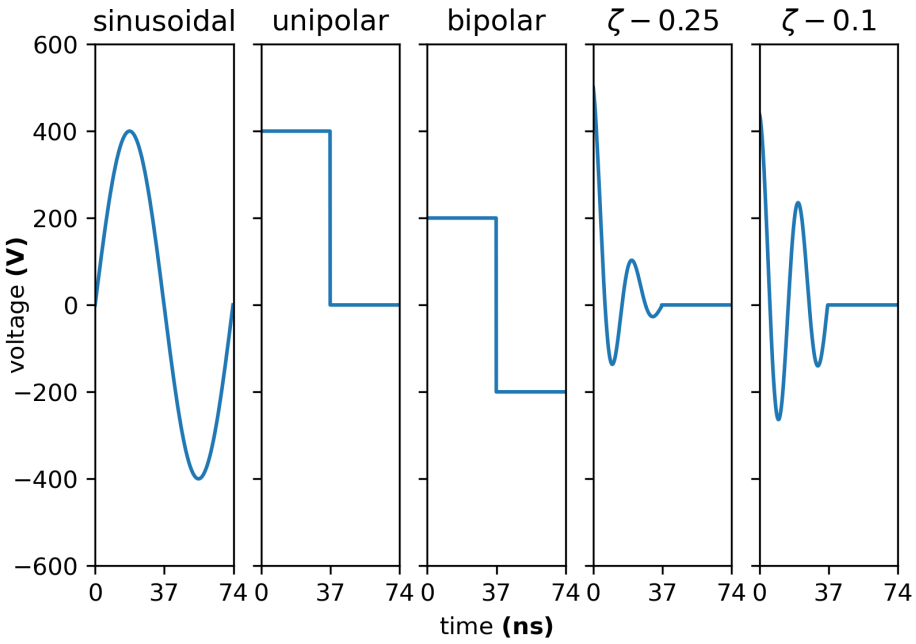

Figure 3.11: Input waveforms used to ignite argon and helium plasmas.

outline the unipolar and bipolar discharges, respectively, each operating at a duty cycle of 50%. In the unipolar pulsed discharge, the voltage amplitude v_0 falls to zero during the switching event. Similarly, for the bipolar pulsed discharge, there is a drop in voltage amplitude to $-v_0$ after the duty cycle.

$$v(t) = \begin{cases} v_0, & \mathrm{t} \leq \mathrm{D_{duty}} * \frac{1}{\mathrm{f}} \\ 0, & \mathrm{t} \geq \mathrm{D_{duty}} * \frac{1}{\mathrm{f}} \end{cases} \tag{3.27}$$

$$v(t) = \begin{cases} v_0, & \mathrm{t} \leq \mathrm{D_{duty}} * \frac{1}{\mathrm{f}} \\ -v_0, & t \geq \mathrm{D_{duty}} * \frac{1}{\mathrm{f}} \end{cases} \tag{3.28}$$

For the sinusoidal damped ignition waveforms, the behavior is dictated by equation 3.29, where v_0 denotes the voltage amplitude, ω_D represents the damped natural frequency as specified by equation 3.30, ω is the natural frequency, and ξ stands for the viscous damping ratio. The sinusoidal decay equation, originally formulated by Resen et al [91]. to analyze vibrational effects in structures, has been repurposed in this study to generate a sinusoidal pulsed discharge, building on previous research.

$$v(t) = e^{\xi\omega t}\left[v_0 \cos\omega_D t + \left(\frac{1}{\omega_D} + 2\xi \sin\omega_D t\right)\right] \tag{3.29}$$

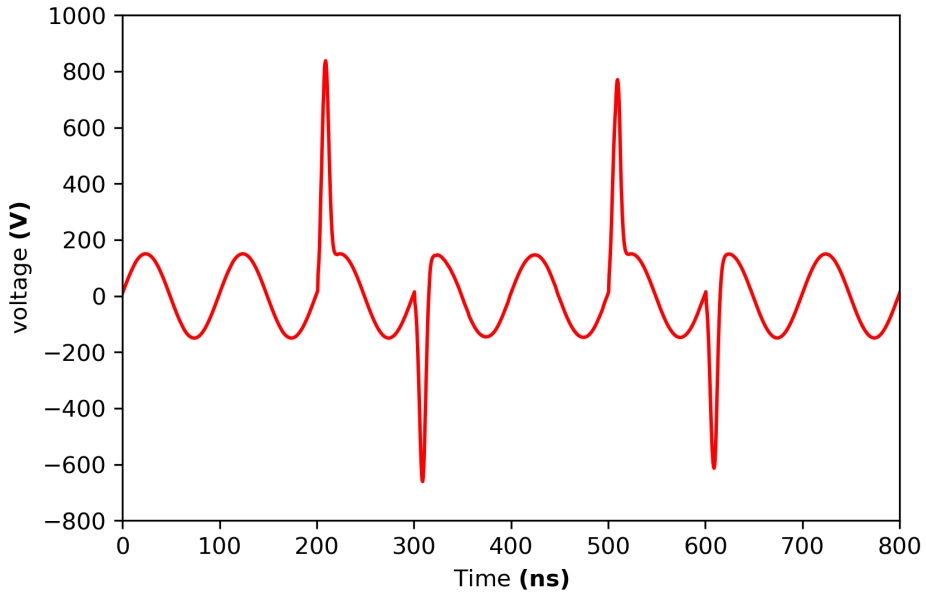

Figure 3.12: Sinusoidal-superposed gaussian waveform modeled for the DMD cases.

$$\omega_D = \omega\sqrt{1-\xi^2} \tag{3.30}$$

Two waveforms are studied for the sinusoidal damped waveforms in the first study: one with a damping factor of $\xi = 0.25$ and the other with a damping factor of $\xi = 0.1$. A value of 3×10^8 is utilized for the natural frequency. Figure 3.12 visually represents these ignition waveforms. For the second study, only a sinusoidal damped waveform with $\xi = 0.25$ is used. For the Gaussian-assisted sinusoidal waveform, the Gaussian waveform is superimposed depending on the configuration of interest. Nonetheless, equations 3.31 and 3.32 relate the sinusoidal, Gaussian distribution, and superposed form at the specified duty cycle.

$$f(x) = \frac{v_g}{\max(\mathrm{f(x)})}\frac{1}{\sigma\sqrt{2\pi}}\exp\frac{-(x-\mu)^2}{2\sigma^2} \tag{3.31}$$

$$\mathrm{v(t)} = \begin{cases} v_0\sin(2\pi ft) + f(x), & \mathrm{t} \leq \mathrm{D_{duty}} * \frac{1}{\mathrm{f}} \\ v_0\sin(2\pi ft), & \mathrm{t} \geq \mathrm{D_{duty}} * \frac{1}{\mathrm{f}} \end{cases} \tag{3.32}$$

Where $\mathrm{v_g}$ is the maximum desired peak of the Gaussian distribution, μ is the median of the normal distribution, and σ^2 is the variance, which is controlled as a function of the duty cycle such that 99.7% of the data is collected. v(t) represents the control of the voltage as a function of the duty cycle.

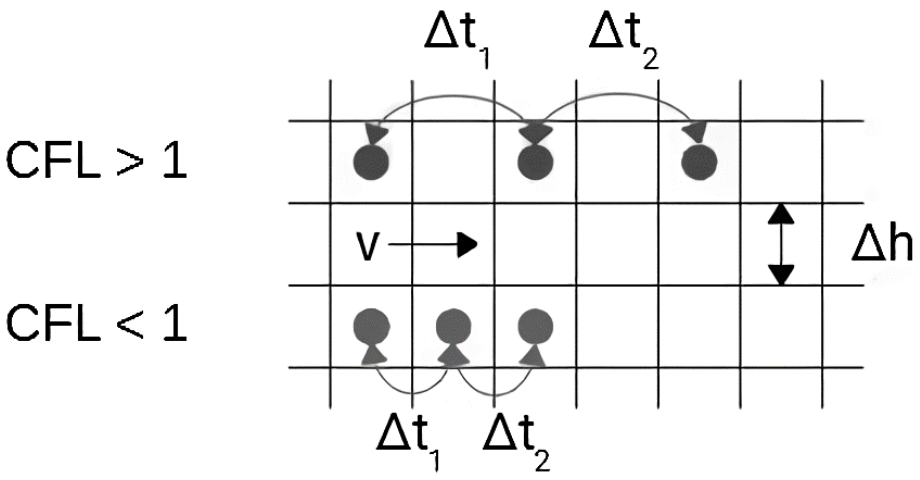

Figure 3.13: Courant controls and effects in numerical models.

3.5 Time controls

To speed up the simulation while ensuring system stability, a Courant condition is used to adjust the time step at each instance as the simulation progresses. The Courant condition specifies that the distance any information travels during the time step within the mesh must be less than the distance between elements [92]; in other words, the information from a given mesh element must propagate only to its immediate neighbors. Figure 3.13 illustrates the relationship between the Courant number and the propagation of information within the mesh. The Courant number is defined in equation 3.33 as

$$\text{Courant number} = \frac{U\Delta t}{\Delta x} \tag{3.33}$$

where U is the velocity vector, Δt is the time step, and Δx is the characteristic size of the mesh [93]. Since the drift-diffusion model calculates the flux of electrons rather than the velocity, the Courant number is expressed as:

$$\text{Courant number} = \frac{1}{2}\frac{\Gamma\Delta t}{\Delta x} \tag{3.34}$$

where Γ is the flux of electrons. A Courant number of 0.7 strikes a balance between stability and speed [94], while a Courant number of 0.5 is used for highly diffusive systems [95]. The time step is determined by comparing the minimum of the calculated time step from the Courant number from equation 3.34 to a user-defined maximum allowed time step. A second calculation compares the maximum between the user-defined minimum allowed time step and the previous comparison.

Chapter 4

Setup of simulation and external tools

4.1 Chemical considerations

The cases studied utilize argon and helium as feedstock gases. As each gas has different reaction profiles and coefficients for parameters such as mobility and drift-diffusion coefficient, it is necessary to provide these profiles for each feedstock gas since the characterization of the plasma depends on these properties. As seen in the governing equations and boundary conditions, the utilization of these different coefficients is ubiquitous. The mobility coefficients are obtained from experimental data referenced in the literature for the ions [96, 97, 98, 99]. For electrons, depending on the feedstock gas being utilized, an empirically obtained cross-sectional area for reaction i of the feedstock gas of the plasma of interest is used and solved using an external Boltzmann solver to determine the electron mobility. The cross-sectional area can be defined as the probability of an particle hitting another particle. The mobility for i charged species is defined as

$$\mu = \frac{q}{m\nu_m} \tag{4.1}$$

Where q is the charge of the species, v_m is the momentum-transfer collision frequency defined as the frequency of collision between ions and neutral species [66], and m is the mass of species i. As such, mobility is a function of a reduced electric field, which relates the electric field within the system to the density of the background gas [66]. The mobility and drift-diffusion are related by equation 2.18, where the diffusion coefficient relates the diffusion of the charged particles within a system to its electrical characterization and temperature of active species i. Mobilities and drift-diffusion are tabulated in table 4.1 and 4.2 for the ions and electrons of both argon and helium.

Table 4.1: Mobility/drift diffusion coefficients and species weights that compose the argon plasma. DD stands for drift diffusion coefficient.

Specie	**Molecular Weight**	**Mobility/DD-coefficient**	**References**
Ar	39.99	-	[100]
Ar^+	39.99	μ_{Ar^+}	[100, 96]
Ar_2^+	79.89	$\mu_{Ar_2^+}$	[100, 96]
Ar*	39.99	1.65×10^{-5}	[100, 96]
e^-	5.48×10^{-4}	μ_{e^-}	[100, 101]

Table 4.2: Mobility/drift diffusion coefficients and species weights that compose the helium plasma. DD stands for drift diffusion coefficient.

Specie	**Molecular Weight**	**Mobility/DD-coefficient**	**References**
He	4.00	-	[100]
He_2^*	8.00	4.73×10^{-5}	[100, 69]
He*	4.00	1.64×10^{-4}	[100, 69]
He_2^+	8.00	$\mu_{He_2^+}$	[100, 69]
He^+	4.00	μ_{He^+}	[100, 69]
e^-	5.48×10^{-4}	μ_{e^-}	[100, 101]

The reaction rates need to be calculated to calculate the sink and source terms for plasma reactions. While in many instances, the reaction rates can be calculated using the Arrhenius form if the gas is assumed to have a Maxwellian distribution for the velocities of the particles, the Maxwellian distribution falls short when modeling non-thermal plasmas due to differences in energy between the electrons and the neutral particles [102]. To overcome these deficiencies, the Boltzmann equation can be further developed by using spherical coordinates, alongside a two-term expansion, to calculate the distribution function [101]. As described by Hagelaar, while Boltzmann solvers have usually been developed with high accuracy (up to seven expansion terms to verify experimental data), for a fluid model, there are different requirements, including being able to work over a large range of discharge conditions, fast numerical convergence, and a larger tolerance for errors in the calculation of derived quantities such as mobilities and reaction rates. The end goal is not to compare against specific experiments but to be useful for a large range of modeling conditions. As such, BOLSIG+, a Boltzmann solver developed by Hagelaar, is utilized to obtain the electron energy distribution function (EEDF) and derived quantities such as reaction rates and electron mobilities of the plasma [101]. For the electron mobilities, as the background gas number density is 1 Torr in BOLSIG+, and since the plasmas presented are op-

Table 4.3: Reaction set used in the argon cases, excluding the DMD database. Rates in $cm^3 \cdot s^{-1}$ and $cm^6 \cdot s^{-1}$ for two- and three-body collisions, respectively. T_e and T in K.

	Reaction	**Reaction Rate**	$\Delta\epsilon$	**Ref.**
		$cm^3 \cdot s^{-1}$ or $cm^6 \cdot s^{-1}$	**eV**	
R1	e + Ar ⇒ 2e + Ar^+	σ^1	15.76	[101]
R2	e + Ar ⇒ e + Ar*	σ^a	11.55	[101]
R3	e + Ar* ⇒ 2e + Ar^+	σ^a	4.14	[101]
R4	2Ar* ⇒ e + Ar^+ + Ar	$1.2 \times 10^{-9}(300/T)^{1/2}$	-	[104]
R5	Ar^+ + 2Ar ⇒ Ar_2^+ + Ar	$2.5 \times 10^{-31}(300/T)^{3/2}$	-	[105]
R6	e + Ar_2^+ ⇒ Ar* + Ar	$7 \times 10^{-7}(300/T_e)^{1/2}$	-	[106]
R7	Ar* ⇒ Ar + hv	5×10^5	-	[107]
R8	e + Ar ⇒ e + Ar	σ^a	-	[101]

Table 4.4: Reaction set used in the argon cases, excluding parametrization cases. Rates in $cm^3 \cdot s^{-1}$ and $cm^6 \cdot s^{-1}$ for two- and three-body collisions, respectively. T_e and T in K.

	Reaction	**Reaction Rate**	$\Delta\epsilon$	**Ref.**
		$cm^3 \cdot s^{-1}$ or $cm^6 \cdot s^{-1}$	**eV**	
R1	e + Ar ⇒ 2e + Ar^+	σ^2	15.76	[101]
R2	e + Ar ⇒ e + Ar*	σ^a	11.55	[101]
R3	e + Ar* ⇒ 2e + Ar^+	σ^a	4.14	[101]
R4	Ar* + e ⇒ Ar + e	1.7×10^{-9}	-11.55	-
R5	Ar* + Ar* ⇒ Ar^+ + e	2.8×10^{-10}	-	-
R6	Ar* + Ar ⇒ Ar + Ar	3.0×10^{-15}	-	-

erated at 760 Torr except for the argon plasma where the DMD method is applied, the mobilities have to be adjusted accordingly [103]. To do so, the mobility provided by BOLSIG+ is divided by the number density at 1 Torr and room temperature, then multiplied by a number density corresponding to the operating conditions. The mobility is calculated in BOLSIG+ in equation 4.2.

$$\mu N = -\frac{\gamma}{3}\int_0^\infty \frac{\epsilon}{\widetilde{\sigma_m}}\frac{\partial F_0}{\partial \epsilon}d\epsilon \tag{4.2}$$

Where ϵ corresponds to the electron energy, F_0 is the isotropic part of the distribution function, $\widetilde{\sigma_m}$ is the effective total momentum-transfer cross-section, and γ is a constant coefficient relating the electron charge to the mass.

Table 4.5: Reaction set used in the helium case. Rates in $cm^3 \cdot s^{-1}$ and $cm^6 \cdot s^{-1}$ for two- and three-body collisions, respectively. T_e in K.

	Reaction	**Reaction Rate**	$\Delta\epsilon$	**Ref.**
		$\mathbf{cm^3 \cdot s^{-1}}$ **or** $\mathbf{cm^6 \cdot s^{-1}}$	**eV**	
R1	$e + He \Rightarrow He^* + e$	$2.308 \times 10^{-10} T_e^{0.31} \exp\left(-\frac{2.297 \times 10^5}{T_e}\right)$	19.8	[108, 109]
R2	$e + He^* \Rightarrow He + e$	$1.099 \times 10^{-11} T_e^{0.31}$	-19.8	[108]
R3	$e + He \Rightarrow He^+ + 2e$	$2.584 \times 10^{-12} T_e^{0.68} \exp\left(-\frac{2.854 \times 10^5}{T_e}\right)$	24.6	[108, 109]
R4	$e + He^* \Rightarrow He^+ + 2e$	$4.661 \times 10^{-10} T_e^{0.6} \exp\left(-\frac{5.546 \times 10^4}{T_e}\right)$	4.87	[108, 109]
R5	$e + He_2^* \Rightarrow He_2^+ + 2e$	$1.268 \times 10^{-12} T_e^{0.71} \exp\left(-\frac{3.945 \times 10^4}{T_e}\right)$	3.4	[108]
R6	$e + He_2^+ \Rightarrow He^* + He$	$5.386 \times 10^{-7} T_e^{-0.5}$	-	[108]
R7	$He^* + 2He \Rightarrow He^*_2 + He$	1.3×10^{-33}	-	[108]
R8	$He^+ + 2He \Rightarrow He_2^+ + He$	1.0×10^{-33}	-	[108]
R9	$e + He_2^+ \Rightarrow 2He$	1.0×10^{-9}	-	[110]
R10	$e + He_2^+ + He \Rightarrow 3He$	2.0×10^{-27}	-	[110]

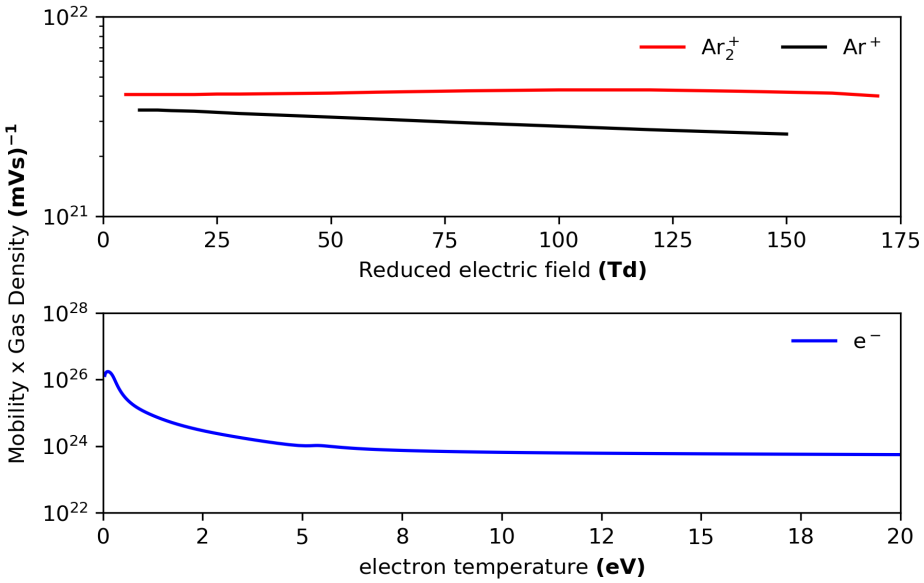

Figure 4.1: Mobilities of active species for argon.

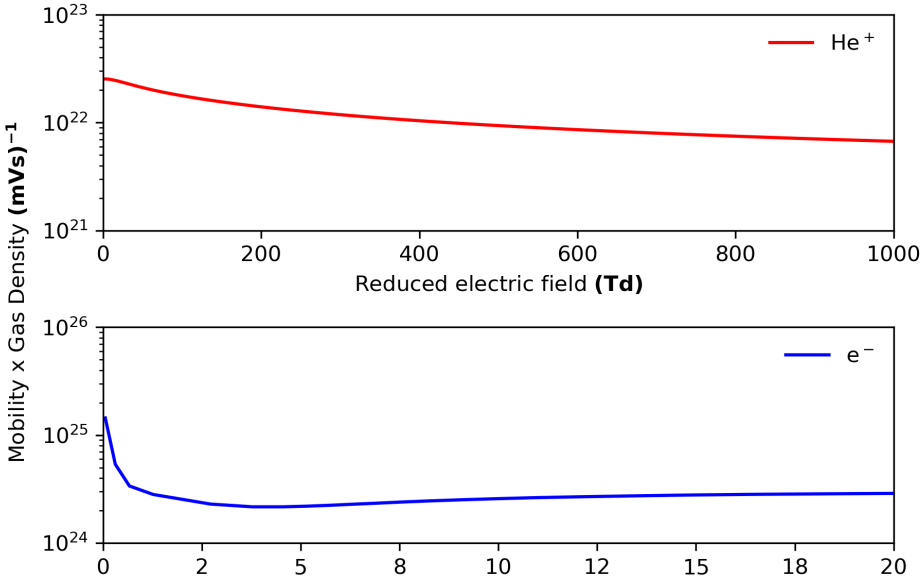

Figure 4.2: Mobilities of active species for helium.

Tables 4.3, 4.4 and 4.5 correspond to the reaction rate profiles for the argon and helium plasmas. For argon, two reaction profiles were provided. Table 4.3 is used for the parametric studies of APGD plasmas operating at atmospheric pressure, while table 4.4 is used to create a database of different simulations and train a DMD model for parametrizing operating conditions. The reason for different argon reaction profiles is due to the simplicity of the second reaction profile for argon shown in table 4.4, which allows the study of DMD algorithms regarding feasibility before upscaling usage of DBD to more complicated plasma models. For table 4.4, reactions 5 thru 9 are provided by the experience garnered thru modeling argon plasma, making educated assumptions for such reaction rates. For helium, as Lui [38] was able to accurately simulate helium plasmas at atmospheric pressure using a Maxwellian approach, the reaction rates for the active species are calculated using the Arrhenius form as seen in table 4.5. However, unless noted otherwise, such an instance is not the case for nonthermal-atmospheric plasmas, preferring a Boltzmann approach to the calculation of plasma parameters [102]. The EEDF distribution was solved using BOLSIG+ for the electrons.

The mobility profiles, as a function of the E/N applied as a function of average energy (which is a function of the E/N calculated), are plotted in the figures 4.1 and 4.2 for argon and helium. The average electron energy and reaction rate for argon are calculated utilizing equation 4.3 and equation 4.4.

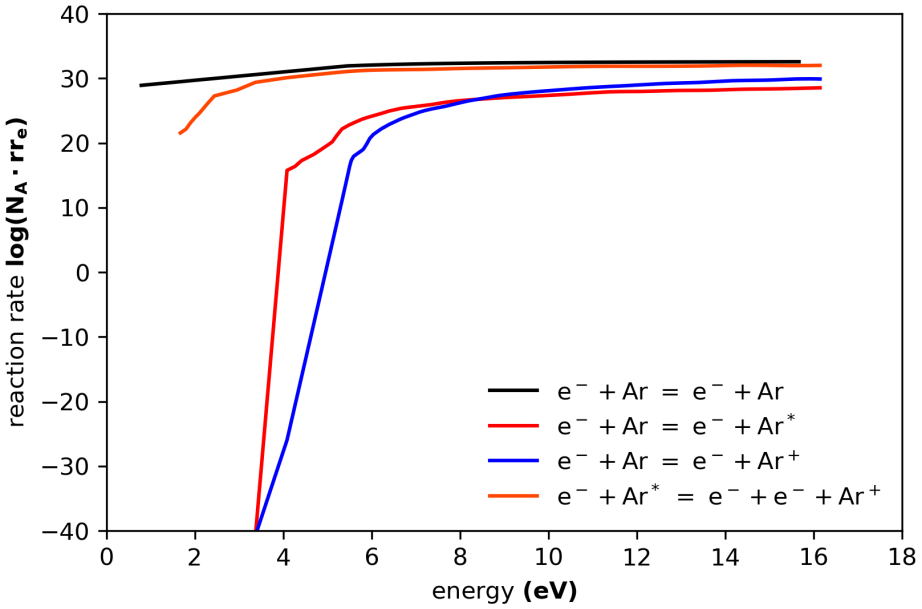

Figure 4.3: Reaction rates for argon calculated by BOLSIG+.

$$n_\epsilon = n \int_0^\infty \epsilon^{3/2} F_0 d\epsilon \equiv n\bar{\epsilon} \tag{4.3}$$

These values will be used to match the properties in the system with the average electron energy calculated using the FVM method. While a concern with the BOLSIG+ model is the increase in anisotropy in the distribution profile as the E/N increases [101], the relatively low operating electron temperature (up to 10 eV in some cases for argon and helium plasmas) precludes this from being an issue for the plasmas being studied. However, this might not be the case in all instances, and special care might be needed when dealing with high E/N values to ensure acceptable accuracy in the calculated variables.

$$k_k = \gamma \int_0^\infty \epsilon \sigma_k F_0 d\epsilon \tag{4.4}$$

4.2 Generation of mesh

All the cases in these studies consisted of one-dimensional simulations. Therefore, a mesh must be provided to ensure that somaFOAM can interpret it as a one-dimensional, orthogonal mesh. For dielectric cases, the mesh must be coupled with the

primary mesh. While meshes can be constructed using built-in tools like `blockMesh` [111], these tools are tedious and have limited usability for more complex meshes. Thus, Gmsh, an open-source meshing tool [112], generates the meshes. Gmsh's capabilities include labeling boundary conditions, defining volume spaces, and mesh refinement in both structured and unstructured meshes, among other functions. A noteworthy feature of Gmsh is its ability to create meshes using both the GUI and scripting, allowing for fine-tuned refinement and automation of the mesh generation process when needed. Sample code used to generate meshes for argon and helium plasmas is shown in figure 4.4.

By default, somaFOAM defines the mesh in a three-dimensional (3D) space. Unless specified otherwise by the user, the mesh defaults to a 3D space. Figure 4.5 showcase the generation of the mesh defined by the script in Figure 4.4. Lines 1 to 4 represent the points defining the physical boundaries of the mesh, where the mesh will be generated between these points. Lines 6 to 9 represent the lines connecting the points to bind the mesh. Lines 11 to 13 define the physical extent of the mesh and set up the mesh gradient within the defined geometry, with a resolution of 800 cells. Lines 14 and 16 define the mesh as structured, ensuring orthogonality, while lines 17 to 21 define the volume of the mesh to ensure compliance with OpenFOAM. Lines 23 to 26 define the boundary labels and the volume of the mesh.

After using Gmsh, the mesh is converted to a format compatible with somaFOAM using the command `gmshToFoam` in the terminal, followed by `transformPoints -scale "(0.001 0.001 0.001)"`, which scales the mesh in the x, y, and z directions accordingly. In the dielectric case, Figure 4.6 shows the coupling of the plasma mesh to the dielectric mesh, where the `directMappedPatch` boundary condition is used to couple the dielectric mesh to the plasma mesh. The boundary conditions are defined within the mesh files in somaFOAM, as seen in 4.7, where `patch` indicates a base-type boundary condition further defined in the `0` folders within the case directory. To define the dimensions of the mesh, `empty` indicates an empty boundary condition.

This approach ensures that the meshing process is efficient and adaptable, providing a robust framework for simulating plasma phenomena with somaFOAM. The use of Gmsh for mesh generation and subsequent conversion for somaFOAM compatibility streamlines the setup, allowing for precise control and customization according to the specific requirements of each simulation.

4.3 Dynamic mode decomposition

One of the main limitations of parametric studies is the large number of simulations required to consider the expansive ranges of the studied variables. Depending on the parametrization required and how many variables are to be parametrized, these databases can be expensive in size and computational runtime. They require many processors if run in serial mode, alongside significant storage requirements if high

```
Point(1) = {0, 0, 0, 1.0};
Point(2) = {0.40, 0, 0, 1.0};
Point(3) = {1.60, 0, 0, 1.0};
Point(4) = {2, 0, 0, 1.0};
Point(5) = {0, 20, 0, 1.0};
Point(6) = {0.40, 20, 0, 1.0};
Point(7) = {1.60, 20, 0, 1.0};
Point(8) = {2, 20, 0, 1.0};

Line(1) = {5, 1};
Line(2) = {1, 2};
Line(3) = {2, 6};
Line(4) = {6, 5};
Line(5) = {6, 7};
Line(6) = {7, 3};
Line(7) = {2, 3};
Line(8) = {3, 4};
Line(9) = {4, 8};
Line(10) = {8, 7};

Line Loop(1) = {1, 2, 3, 4};
Plane Surface(1) = {1};
Line Loop(2) = {7, -6, -5, -3};
Plane Surface(2) = {2};
Line Loop(3) = {10, 6, 8, 9};
Plane Surface(3) = {3};
Transfinite Line {4, 2, 8, 10} = 100 Using Progression 1;
Transfinite Line {5, 7} = 25 Using Progression 1;
Transfinite Surface {1};
Transfinite Surface {2};
Transfinite Surface {3};
Recombine Surface {1, 2, 3};

Extrude {0, 0, 400} {
  Surface{1}; Surface{2}; Surface{3};
  Layers{1};
  Recombine;
}

Physical Surface("otherFaces") = {54, 32, 76, 1, 2, 3, 49, 31, 63, 23, 41, 71};
Physical Surface("electrode") = {19};
Physical Surface("ground") = {75};
Physical Volume("internalfield") = {2, 1, 3};
```

Figure 4.4: gMesh scripting of 1D mesh.

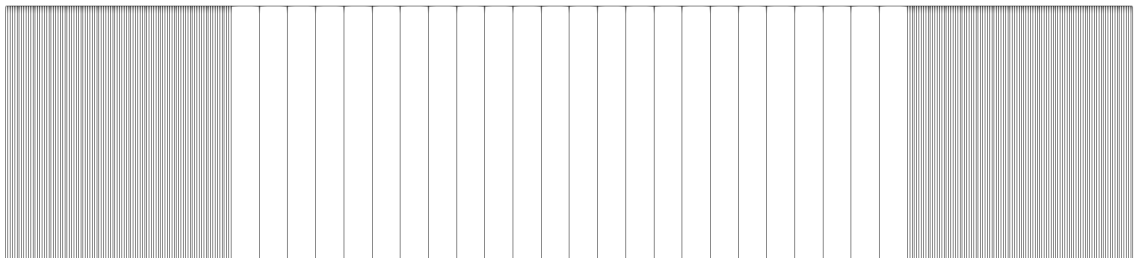

Figure 4.5: Mesh representation for the bare electrode cases.

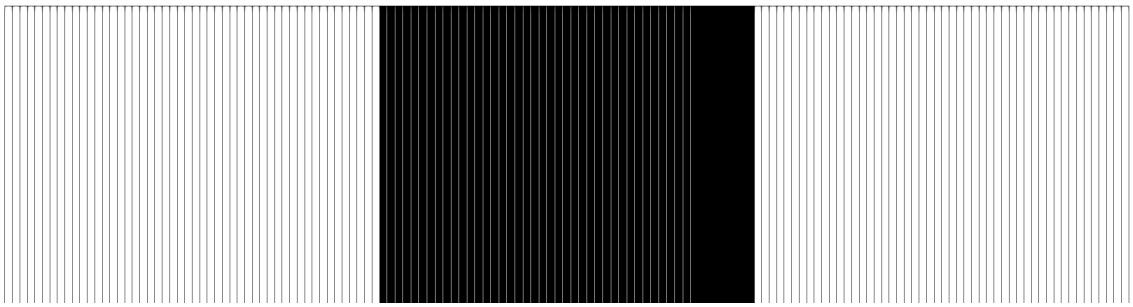

Figure 4.6: Mesh representation of the DBD cases.

```
3
(
    otherfaces
    {
        type            empty;
        nFaces          888;
        startFace       221;
    }
    electrode
    {
        type            patch;
        nFaces          1;
        startFace       1109;
    }
    ground
    {
        type            patch;
        nFaces          1;
        startFace       1110;
    }
)
```

Figure 4.7: Boundary condition definition in `foam` mesh format.

resolution is needed. Thus, it is beneficial to implement data learning methodologies that can accurately predict parametrized behavior within a set of ranges of interest while minimizing large storage requirements and computational downtime. It is worth investigating the feasibility of utilizing data-driven algorithms such as DMD [113]. A training model can be developed to obtain intermediate values without actual simulations by running an initial dataset of ranges of interest within the parametrization [60]. This possibility would allow efficient and rapid data output, accelerating research interests [114]. The aforementioned studies on the parametrization of the voltage for argon plasmas indicate a need for such algorithms, as the parametrization required multiple servers and storage space to obtain a solution. Hence, the utilization of DMD in these studies is necessary.

DMD, developed by Schmid in fluid mechanics to study fluid phenomena [65], allows for a data-driven approach to complex phenomena based on spatiotemporal coherent structures. One of the main advantages of the DMD method is that it is independent of the governing equations used to model the trained data; rather, data is the driving method [59]. Applications where the DMD method has shown interest include neurosciences [115], blood flow [116], epidemiology [117], robotics [118], finance [119], among others, where the commonality is the highly nonlinear nature of the data in both time and space [120, 121, 122]. Thus, DMD offers attractive applications within the plasma field, where plasmas, regardless of their mode of operation, are highly nonlinear in both time and space, as it is often required to have an educated assumptions to simplify the plasma model while ensuring a baseline level of fidelity within the data. While the scope of DMD for the following study is towards numerical models [114], there is a compelling argument for using DMD methods for experimental data [65]. DMD can filter data noise [123], provide predictions independent of an initial set of parameters, and predict model behavior for all time in the future, provided the model baseline is in a cyclical quasi-steady state [62].

When processing a dataset, the DMD approach utilizes a singular value decomposition (SVD) [62] approach and expands upon it. The SVD approach allows the capture of the dominant patterns within the data while discarding weakly correlated data by calculating the strengths of the correlations when determining the eigenvalues of the orthonormal coefficient matrix [124]. The SVD algorithm is used in processes involving data compression and noise reduction. The SVD is calculated by expressing the dataset X, as seen in equation 4.5, in terms of its left-singular vectors ($\widetilde{\mathbf{U}}$), right-singular vectors ($\widetilde{\mathbf{V}}$), and singular values ($\widetilde{\mathbf{\Sigma}}$) as seen in equation 4.6, which arrange the diagonal from the strongest to the weakest correlation, expanded in equation 4.7, where σ_{k} is the k^{th} diagonal entry of $\widetilde{\mathbf{\Sigma}}$, $\mathbf{u_k}$ the k^{th} columns of $\widetilde{\mathbf{U}}$ and $\mathbf{v_k}$ the k^{th} column of $\widetilde{\mathbf{V}}$. The tilde corresponds to a truncated singular value dataset if truncated. The SVD size can be truncated to retain 90-95% of the total variance, as seen in equation 4.7, where the data is organized in terms of the strength of their singular values, from

larger to smaller, with the goal of compressing the data, minimizing computational overhead, and accurately representing the analyzed data [124, 125].

$$\mathbf{X} = \begin{bmatrix} | & | & | & & | \\ \mathbf{x_1} & \mathbf{x_2} & \mathbf{x_3} & ... & \mathbf{x_m} \\ | & | & | & & | \end{bmatrix} \tag{4.5}$$

$$\mathbf{X} \approx \tilde{\mathbf{U}}\tilde{\mathbf{\Sigma}}\tilde{\mathbf{V}}^T \tag{4.6}$$

$$\mathbf{X} = \sum_{k=1}^{m} \sigma_k \mathbf{u}_k \mathbf{v}_k^T = \sigma_1 \mathbf{u}_1 \mathbf{v}_1^T + \sigma_2 \mathbf{u}_2 \mathbf{v}_2^T + ... + \sigma_m \mathbf{u}_m \mathbf{v}_m^T \tag{4.7}$$

The DMD algorithm expands upon the SVD algorithm to allow for time evolution analysis of the system. This is done by storing the time evolution of the data into data matrices X and X' as seen in equation 4.8 and 4.9, where each column of X represents an n-dimensional state vector at a time step t_k, and X' represents the state at time t_{k+1} [62].

The DMD algorithm finds the optimal linear transformation approximating the data at each time step [59] first by calculating a reduced best-fit matrix, $\tilde{A}$, by utilizing a pseudo-inverse matrix of the time evolution [124] through the SVD method [62, 124] in rank-r truncated SVD modes to solve the minimization problem as seen in equation 4.10. A represents the full matrix of $\tilde{A}$ in where further manipulation is done as seen by the end result of equation 4.10, reduced by a rank-r.

$$\mathbf{X} = \begin{bmatrix} | & | & | & & | \\ \mathbf{x_1} & \mathbf{x_2} & \mathbf{x_3} & ... & \mathbf{x_{m-1}} \\ | & | & | & & | \end{bmatrix} \tag{4.8}$$

$$\mathbf{X'} = \begin{bmatrix} | & | & | & & | \\ \mathbf{x_2} & \mathbf{x_3} & \mathbf{x_4} & ... & \mathbf{x_m} \\ | & | & | & & | \end{bmatrix} \tag{4.9}$$

$$\tilde{A} = \tilde{U}^T A \tilde{U} = \tilde{U}^T X' \tilde{V} \tilde{\Sigma}^{-1} \tag{4.10}$$

After obtaining $\tilde{A}$, the eigendecomposition is performed to obtain the DMD spatial modes and their dynamics as shown in equation 4.11 for $\tilde{A}$. The diagonal matrix Λ contains the eigenvalues coinciding with the leading eigenvalues of $\tilde{A}$. The eigenvectors W corresponding to the eigenvectors of $\tilde{A}$ as seen in equation 4.11. Finally, the reconstruction of the eigendecomposition of A is done from Λ and W, with the eigenvalues of A given by Λ and the eigenvectors of A (which are the DMD modes) by columns of Φ as shown in equation 4.12. The reconstructed time series from the DMD modes is obtained in equation 4.13, with $\Phi^\dagger$ representing the pseudo inverse matrix of the DMD modes.

$$\widetilde{\mathrm{A}}\mathrm{W} = \Lambda\mathrm{W} \tag{4.11}$$

$$\Phi = \mathrm{X}'\mathrm{V}\Sigma^{-1}\mathrm{W} \tag{4.12}$$

$$x_{k+1} = \Phi\Lambda^{k}\Phi^{\dagger}x_1 \tag{4.13}$$

Chapter 5

Benchmarking and validation

5.1 Validation and benchmark for argon and helium

A benchmark comparison between somaFOAM and published results is essential to establish the reliability of the findings. Figures 5.1 and 5.2 depict the time-averaged number density of active species obtained by Balcon, compared to the results obtained by somaFOAM. Notably, the calculated number densities of e^- and Ar_2^+ exhibit a correspondence with Balcon's results. Although differences exist in the sheath region due to the discretization and solution methods used, the overall trends show a high level of agreement between somaFOAM and Balcon's findings. However, for Ar^+, the correspondence is less explicit than that observed for e^- and Ar_2^+.

The observed discrepancy between the benchmark and somaFOAM for Ar^+ can be attributed to the chosen boundary conditions for the ions and the interactions with processes involving electrons, as detailed in table 4.3. In comparison, the generation of Ar_2^+ in the argon plasma depends on the presence of Ar^+ in reaction R5, which is tied to the bulk background temperature and remains unaffected by electron energy. Conversely, the electron temperature influences the sink reaction R6 for Ar_2^+. While the sink reaction reduces the number density distribution of Ar_2^+ within the sheath region, the implications are more pronounced for Ar^+ as Ar^+ collision frequency is larger than that of Ar_2^+, where as such, the electric field effects on the boundary condition of Ar_2^+ becomes more pronounced. At the same time, the bulk region number density is in agreement between models, further indicating the factors mentioned above as the source of discrepancy.

Figure 5.3 displays the time-averaged electron energy for the helium case. The electron energy was selected as the benchmark metric based on the data provided by Lui et al. The results indicate a strong agreement between somaFOAM and Lui et al. in the bulk region of the plasma. However, notable discrepancies are evident in the sheath region, where the values derived from somaFOAM significantly diverge from

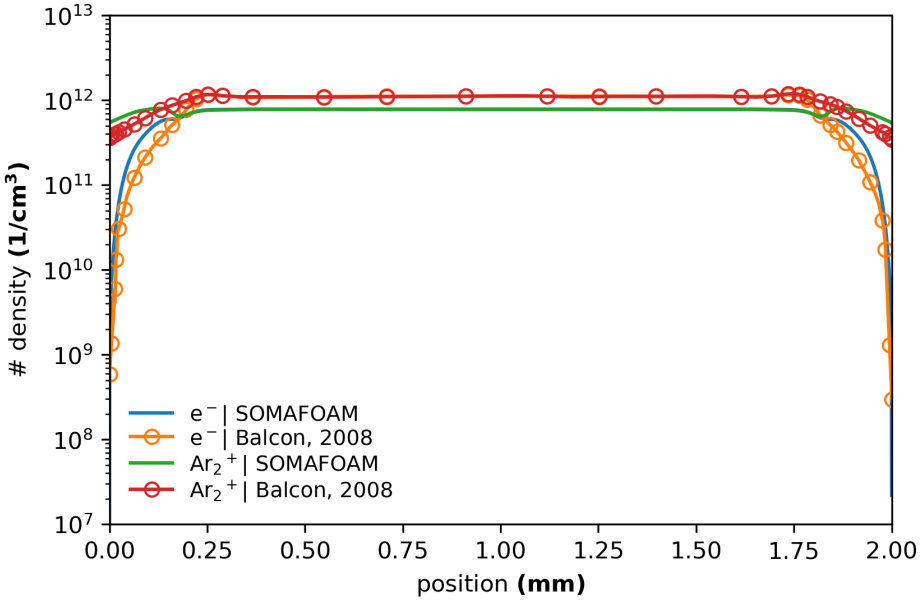

Figure 5.1: Results obtained from somaFOAM for an argon plasma compared to the numerical results of Balcon et al. e^- and Ar_2^+ timed-averaged profiles are compared.

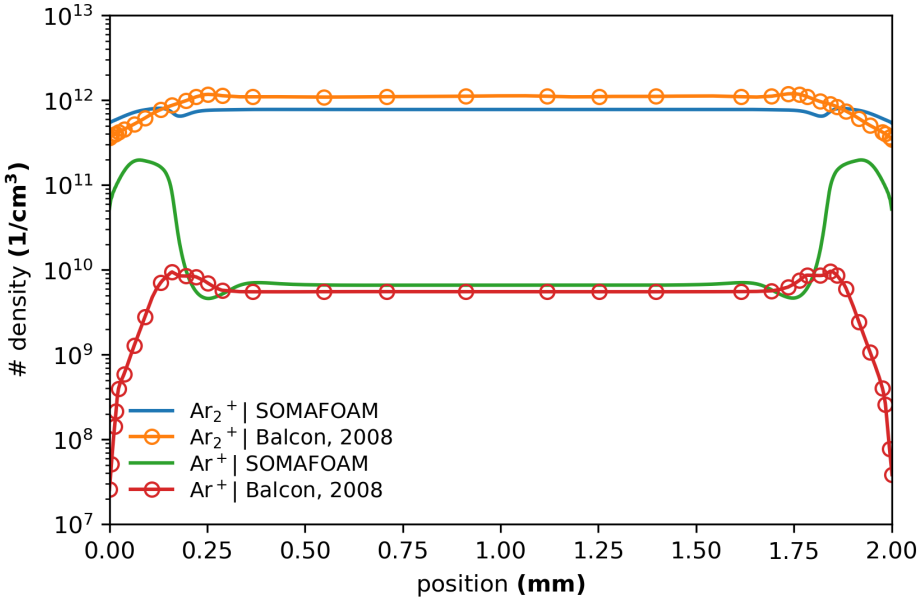

Figure 5.2: Results obtained from somaFOAM for an argon plasma compared to the numerical results of Balcon et al. Ar^+ and Ar_2^+ timed-averaged profiles are compared.

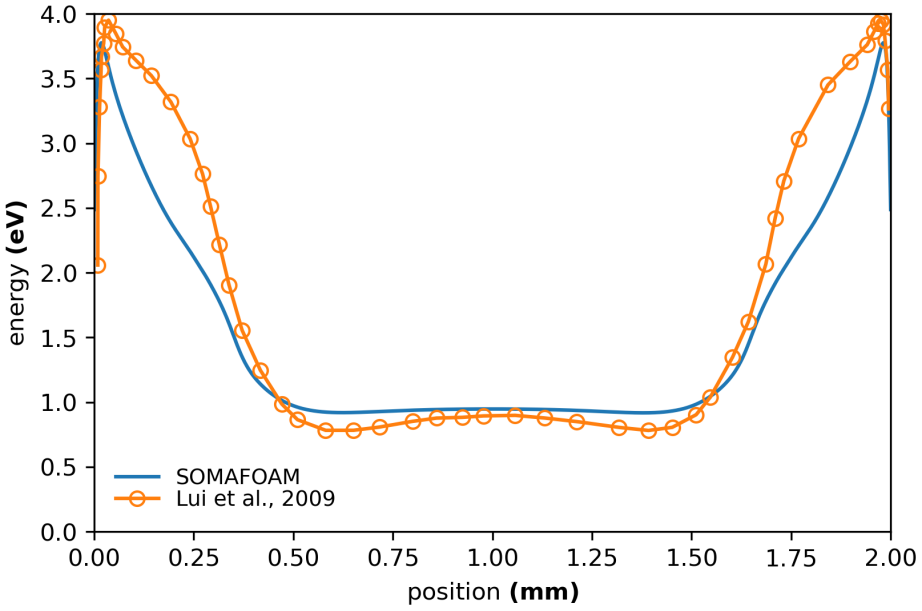

Figure 5.3: Helium benchmark case using timed-averaged electron energy distribution.

those reported by Lui. These observed differences can be attributed to the distinct models employed for comparison. somaFOAM is an FVM model crafted to simulate plasma efficiently while conserving computational resources.

In contrast, Lui et al. adopted a hybrid model, combining a fluid model with a PIC approach for electron modeling. This hybrid approach strikes a balance between accuracy and computational efficiency. Consequently, directly comparing somaFOAM with Lui's numerical results in the sheath region is inappropriate due to the distinct simulation methods employed. Nonetheless, indirect comparisons can be utilized to assess somaFOAM's performance. An examination of the RMS voltage and current curves presented in figure 2 of Lui's paper reveals that the plasma is categorized as weak, indicated by a need of significant voltage increase before transitioning into the unstable region (i.e., the γ region). Additionally, figure 5.4 corroborates the classification of the plasma as weak, evidenced by the lower ionized species number density, situated in the vicinity of 10^{-11} cm^{-3}.

Other validation parameters, such as the input voltage at the electrode and the peak current in the bulk plasma, were considered for the argon case in the benchmark. The values derived were 428 V and 103 mA/cm^2, respectively. The percentage differences were 0.46% and 7.0%, respectively, highlighting a high confidence level in the somaFOAM algorithms' accuracy. These parameters offer valuable insights into the plasma system's behavior and characteristics. The close agreement between the input voltage and peak current values from somaFOAM and those provided by Bal-

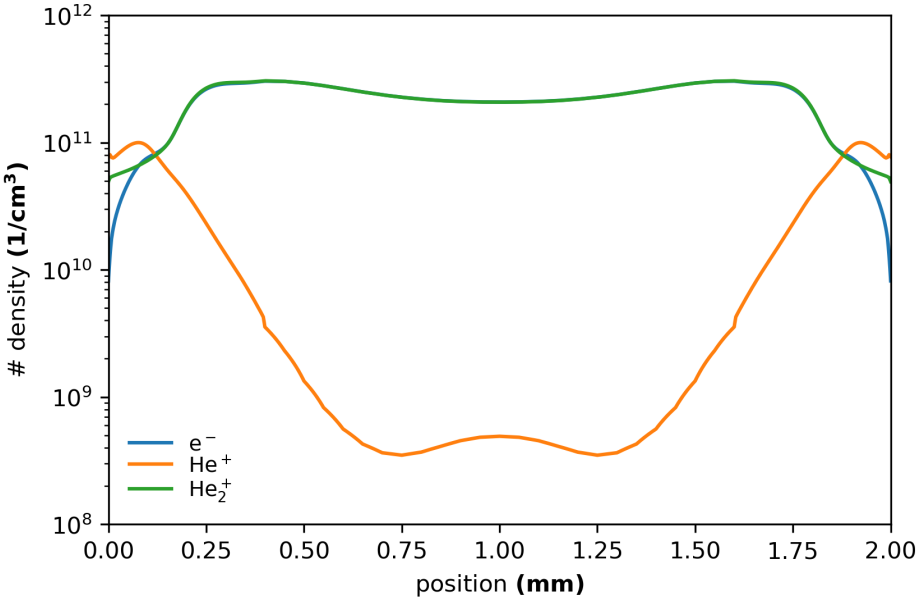

Figure 5.4: Timed-averaged number density of SOMAFOAM benchmark for a helium feedstock gas. The following plots showcase a relatively weak plasma, with e^-, He_2^+ and He^+ number densities in the bulk plasma being 2×10^{11} cm^{-3} and 2×10^{8} cm^{-3}.

con bolsters confidence in somaFOAM's foundational components. These validation results firmly underpin the findings presented in this paper. In the case of helium, a direct comparison of input voltage and bulk current density would not be suitable since Lui only provided numerical data for the temperature profiles. However, the input voltage of 218 V determined by somaFOAM following plasma breakdown can be related to the experimental breakdown voltage of 375 V. While the breakdown voltage is expected to be larger than the post-breakdown voltage, this comparison provides insight into the post-breakdown voltage, suggesting an operating voltage close to the input voltage calculated in the simulation.

Based on these benchmarking results, somaFOAM is suitable as a numerical package for analyzing argon and helium plasmas under RF and APGD conditions. While discrepancies were present in the sheath region, overall, somaFOAM showed agreement with the benchmarks in characterization and plasma behavior. This allows somaFOAM to be utilized and relied upon for the analyses of interest in this paper.

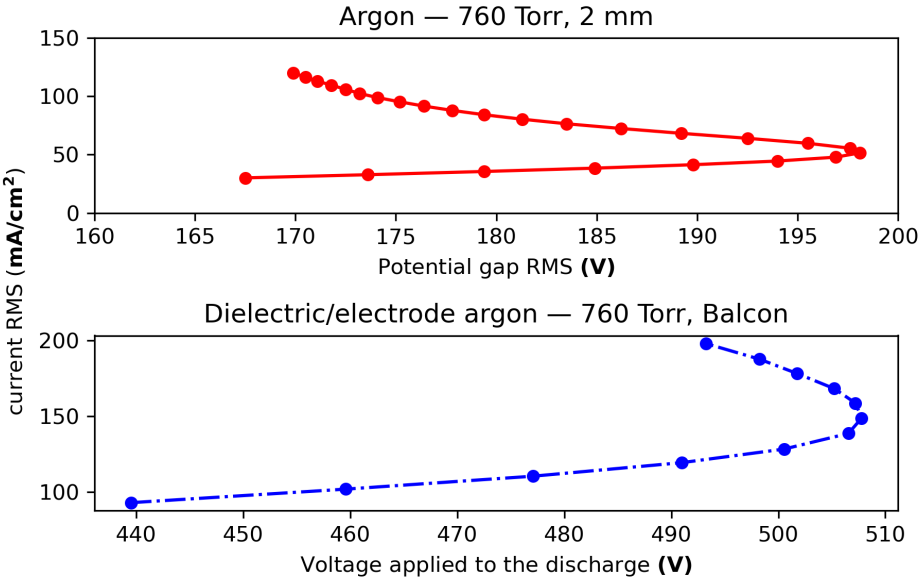

Figure 5.5: Validation of Balcon's argon model compared to somaFOAM.

5.2 Validation of the external resistance circuit

While the validation provided by comparing somaFOAM against models developed by Balcon [126] and Kong [58] shows good agreement utilizing the power-coupled algorithm, the power-coupled algorithm is limited in accurately modeling the effects external system into the plasma because they do not account for the external impedance due to the power supply coupled to the plasma. Alternatives, such as cycle-constant voltage input, would cause divergence in the model as the number density would increase without any resistive element limiting such growth. This is inaccurate in experimental setups since external power supplies are not ideal voltage sources, and the external impedance effectively acts as a ballast. Therefore, as previously discussed, an external, semi-implicit resistive element is considered. To validate that the implementation of Balcon's algorithm matches the expected behavior, figure 5.5 and 5.6 compare the behavior to that of Balcon's resistor-dielectric configuration and those obtained experimentally by Kong.

It should be noted that Balcon's configuration consists of a resistor-dielectric-electrode-plasma-ground. In contrast, the configuration utilized for modeling the argon plasma utilizing somaFOAM is a resistor-plasma-ground, which will yield lower number densities as the dielectric as an electrical element stabilizes the plasma and allows for a larger generation of number densities. At the same time, because the α-γ mode is dependent on the boundary conditions being utilized, the boundary condition utilized for Balcon omits the electric field when considering the ions within

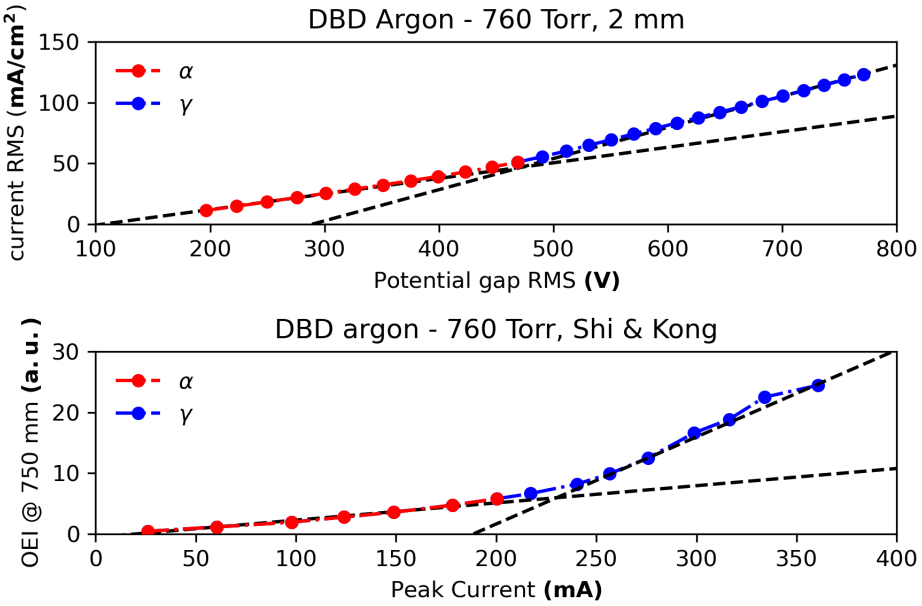

Figure 5.6: Validation of Kong's experimental data compared to somaFOAM in the presence of a dielectric.

the plasma, causing overestimation of the density within the plasma at the critical point. Nonetheless, it is observed that the same behavior is present for both, indicating that the plasma in dielectric-plasma-electrode or electrode-plasma-electrodes operates with a positive differential in the α mode of operation. In contrast, as the plasma approaches the critical point and the γ mode of operation, the differential conductivity changes to that of negative. To demonstrate that the SEE is responsible for the mode of operation, figure 5.7 showcases the effects of a SEE of 0.1 to 0. In the case of an RF-DBD configuration, the α-γ modes of operation are compared to experimental results [58], where the behavior of the plasma in the simulation in comparison to the experiment matches, indicating that the resistive algorithm in somaFOAM is adequate to model DBD systems.

5.3 Validation of DMD model

Before utilizing the DMD method for assisting in the ignition of the plasma, a simple validation was done comparing the evolution of the electron number density during a cycle operated at 10 MHz and 1 Torr, utilizing the argon profile as shown in table 4.4. For the DMD model, nine data points corresponding to the ignition voltages (150 V, 200 V, 225 V, 230 V, 240 V, 245 V, 250 V, 300 V, 450 V) at a time step of

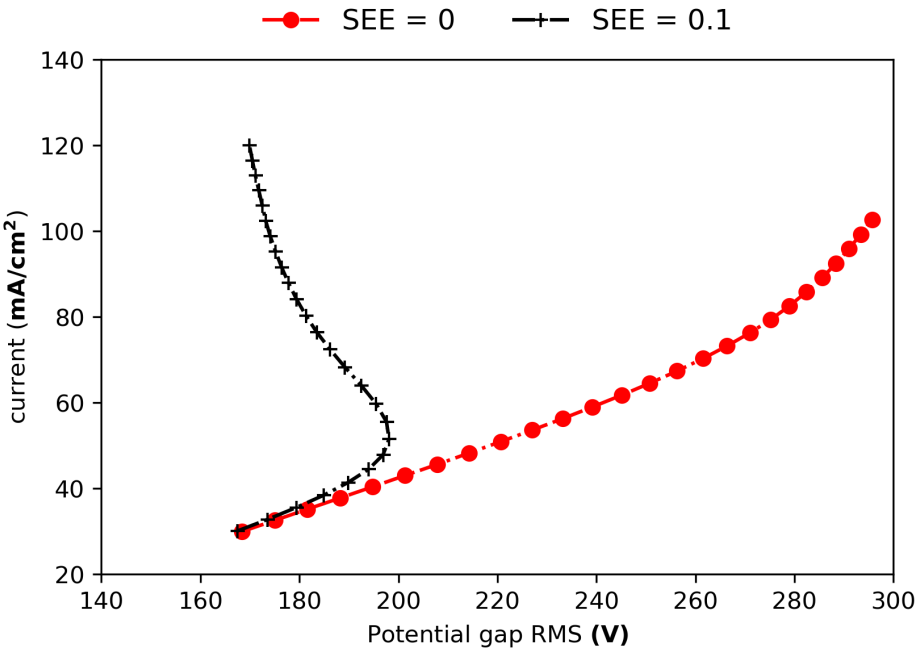

Figure 5.7: Investigation of the effects of SEE on plasma behavior.

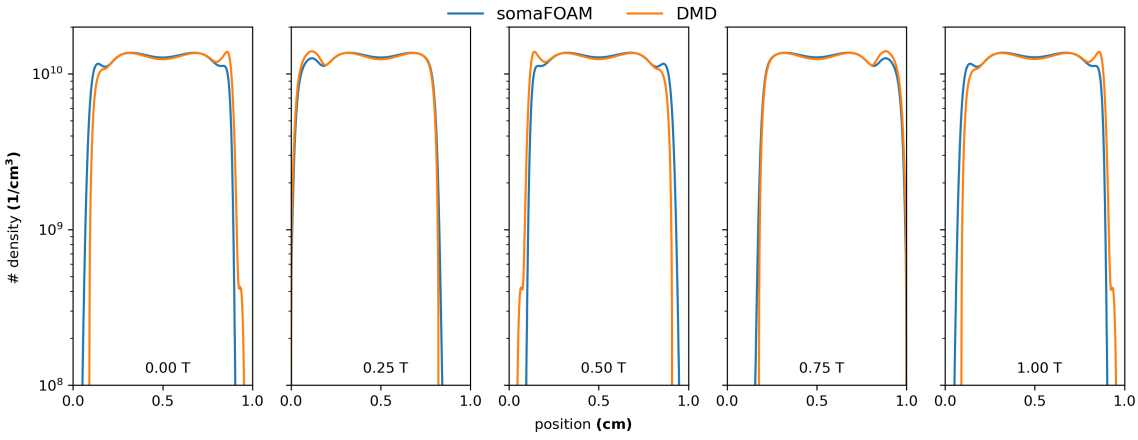

Figure 5.8: Comparison of DMD model to somaFOAM for a sinusoidal-ignited plasma operating at a voltage of 300 V, 1 Torr, 1 cm under an argon feedstock gas. The different plots corresponds to different times within a cycle.

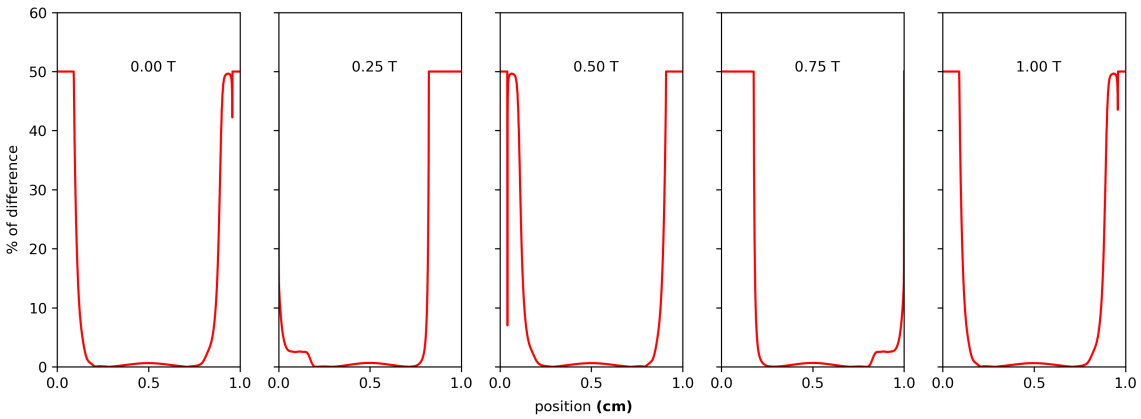

Figure 5.9: Percentage of differences between DMD and somaFOAM for figure 5.8.

5×10^{-5} s and a mesh size of 1000 data points within the time step were utilized. For the DMD itself, a monolithic fit was used [60]. As showcased in figure 5.8, while the profiles show relatively good agreement, the percentage of difference of the mean is 13.79%, 20.32%, 13.79%, 20.18%, and 13.79%, respectively. While these percentages might seem large, it must be considered that the DMD method reduces the data being trained upon by the strength of the singular values to maximize efficiency at the cost of some accuracy, which is acceptable in this instance. The spatial difference is shown in figure 5.9. One common misconception of machine learning and artificial intelligence is that they will provide results as accurate as traditional CFD methods. This is not the goal; rather, the goal is to obtain an acceptable solution that showcases the model's behavior. If needed, the CFD model can be run to extract more details from the solution. Otherwise, data-driven models allow for a solution to be obtained in a fraction of the time, reducing hours to seconds in this instance.

As the solution is analyzed during its cycle, two main behaviors are observed. First, at a quarter of the cycle, the DMD model overestimates the electron density of the sheath region. Second, the symmetry of the plasma at the half cycle, end, and finish does not exactly match, with the DMD model skewing towards the sheath region where the electric field is the strongest. However, taking this into consideration, it can be said that the DMD model for the electrons still maintains the main characterization of the plasma profile as a function of time, despite the discrepancies. While this model was trained using voltages that do not break down the gas, voltages that do break down the gas (245 V) were also included in the training of the DMD algorithm to distinguish between regions where the gas does not break down and where it does. While other data could have been trained, such as ions, electrons were selected because they represent the strongest non-linearity effects within the system, pushing the envelope with DMD. It must be mentioned that while DMD has been able to

accurately model the general behavior of the plasma, it struggles with accurately modeling the sheath regions. In this particular instance, the small dataset could have contributed to the overestimation and the mentioned asymmetry. However, running a large dataset could hamper one of the advantages of using DMD, which is relatively accurate results with minimal downtime, as the results are data-driven independent of the physics of the problem itself. Nonetheless, a trend in the characterization of the sheath region for the DMD algorithm still follows somaFOAM results, showing good agreement in the trend of the sheath characterization.

Chapter 6

Diagnostic of helium and argon plasmas

6.1 Setup of simulations

The operating conditions for the argon and helium plasma cases consist of the chemical profiles shown in tables 4.3 and 4.5. A one-dimensional mesh is utilized for the geometrical considerations, consisting of 800 cells with an electrode area of 78.15 cm^2 for the argon plasma and 3.14 cm^2 for the helium plasma. A power of 3 W and 915 W was applied in the waveforms described in figure 3.11, ensuring that the waveforms are ignited under the same power conditions. The goal is determining whether different number densities are obtained at constant power. The power-coupled algorithm is described in figure 3.8, showcasing its utilization.

The boundary conditions for argon match those of Balcon [39], with a SEE of 0.1 and secondary electrons provided with an energy of 0 eV. The background gas temperature is 300 K, with an operating pressure of 760 Torr. A SEE of 0.1 is utilized for the helium plasma, coupled with an energy of 5 eV, a background temperature of 350 K, and an operating pressure of 760 Torr, following Lui's boundary conditions [38]. A Courant-dependent time step ranges from 1×10^{-10} to 1×10^{-15} seconds, depending on a maximum Courant number of 0.7. The discretization schemes and solution of the numerical model are described in section 3.2.

6.2 Results for helium

While argon is a low-cost alternative to helium [56], helium has been the benchmark when studying plasma characterization basics because of its ease of ignition and stability [41]. Thus, studying the parametrization of helium gas is important as it provides a starting point. Time-averaged, spatially averaged profiles for helium plasmas using sinusoidal, pulsed, and sinusoidal decay ignition waveforms are shown

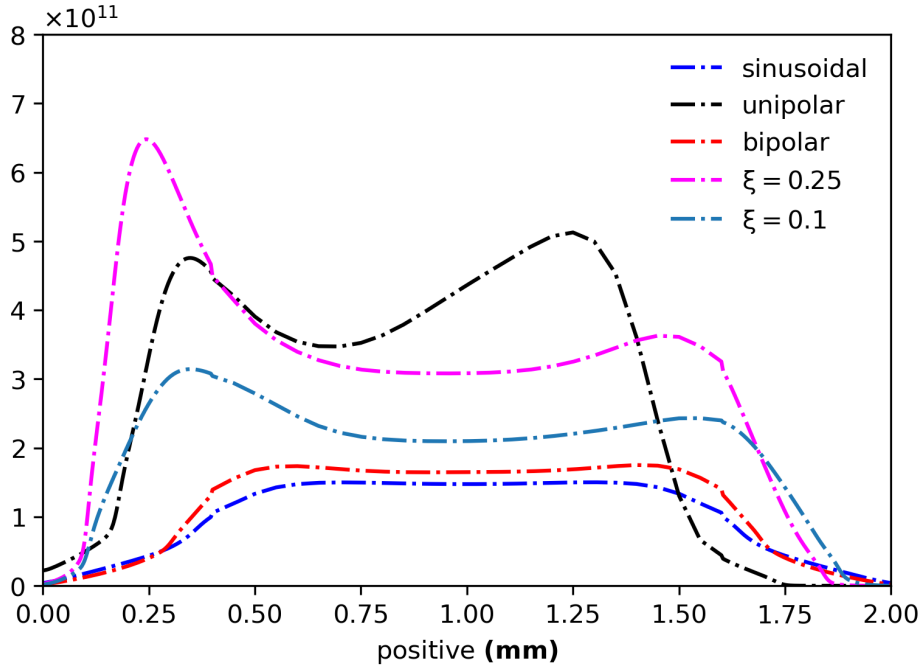

Figure 6.1: Spatio-temporal averaged number densities for e^- under different ignition waveforms.

in figure 6.2. The bulk number densities of e^- are 1.01 x 10^{11} cm^{-3}, 1.16 x 10^{11} cm^{-3}, 2.72 x 10^{11} cm^{-3}, 2.96 x 10^{11} cm^{-3}, and 1.95 x 10^{11} cm^{-3} for plasma ignited using sinusoidal, bipolar, unipolar, and sinusoidal decay waveforms with damping factors of 0.25 and 0.1, respectively. In other words, the sinusoidal decay waveform ($\xi = 0.25$) generates the strongest plasma, followed by unipolar, sinusoidal decay waveform ($\xi = 0.1$), sinusoidal, and bipolar. From an efficiency standpoint, aiming to generate the strongest plasma, the sinusoidal decay waveform ($\xi = 0.25$) is the most effective. Nevertheless, a more comprehensive understanding of operational mechanisms is required, extending beyond mere number densities. A thorough electrical and electron characterization will provide deeper insight into plasma properties and resultant intensity.

Figures 6.2, 6.3, and 6.4 depict the electrical characterization of sinusoidal decay waveforms ($\xi = 0.25, 0.1$) and sinusoidal waveforms at the midpoint of the gap, corresponding to the bulk plasma. By measuring the phase shift between the bulk voltage and current, shifts of 63.59°, 56.63°, and 79.14° were obtained. While the sinusoidal waveform operates in the α mode, the sinusoidal decay waveform shift angle suggests operation in the γ mode [22, 127], characterized by a decreased shift angle, indicating a transition from a capacitive to a resistive mode. The bulk electron evolution in

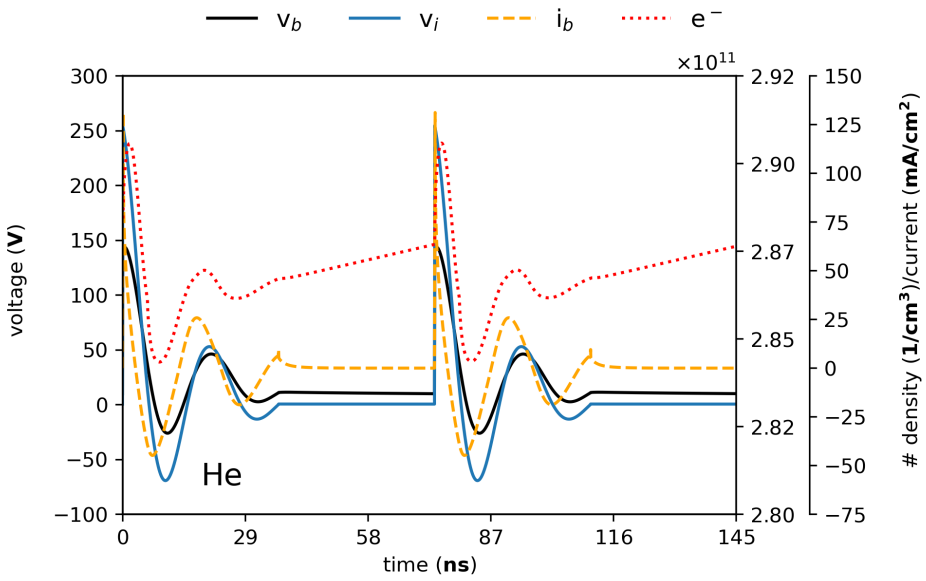

Figure 6.2: Voltage, current density, and number density of electrons for plasmas driven by a sinusoidal decay waveform ($\xi = 0.25$). v_b, v_i, i_b and e^- correspond to the bulk plasma voltage, input plasma voltage, bulk plasma current and electron number density, respectively.

figures 6.2, 6.3 suggest this. Comparing the sinusoidal and bipolar electron profiles to the damped profiles shows an uptick in electron activity in the bulk plasma after the input voltage is cut off, indicating domination by SEE as even without an external source, because of the energy within the system, the SEE is still dominant.

Notably, although operating plasmas in the γ mode are often considered ineffective due to the risk of arcing, the fact that the ignition waveforms utilized operates at the same power indicates that the sinusoidal decay waveforms can operate more efficiently than both sinusoidal and pulsed waveforms. Additionally, the shift angle of the sinusoidal decay waveform ($\xi = 0.25$) is observed to be larger than that of its ($\xi = 0.1$) counterpart. This suggests that a stronger damping factor, while allowing for higher plasma number density, also provides greater stability than a plasma driven by a lower damping factor. Therefore, higher damping is favorable. However, operating the plasma at the same power does not provide insight into its stability, with further investigation into the waveforms' stability necessary to optimize plasma density and prevent constriction and arcing. While both sinusoidal decay waveforms operate at a frequency of 13.56 MHz, they fundamentally function at 50 MHz. This higher frequency allows for more nuanced control over plasma characterization since increasing the frequency appears to raise the critical point between the α and γ modes [38, 31].

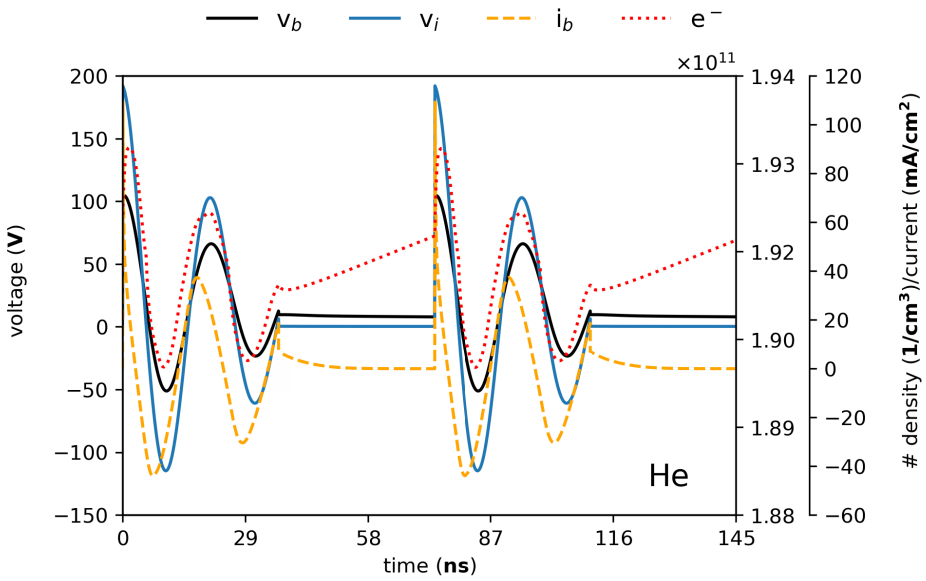

Figure 6.3: Voltage, current density, and number density of electrons for plasmas driven by a sinusoidal decay waveform ($\xi = 0.1$). v_b, v_i, i_b and e^- correspond to the bulk plasma voltage, input plasma voltage, bulk plasma current and electron number density, respectively.

The operating mode of the unipolar pulsed waveform resembles a DC discharge, especially when observing the cathode fall in figure 6.5 [37, 128, 129, 130, 131]. However, the characterization cannot be fully equated to a DC discharge due to the sheath region in the anode. Nevertheless, similarities exist. In the case of the bipolar pulsed discharge, a behavior similar to a sinusoidal glow discharge is characterized by the symmetry of the sheaths. Figure 6.6 displays the electrical characterization of both unipolar and bipolar ignited plasmas. When comparing the bulk electron density for plasmas driven by a unipolar waveform to a bipolar waveform, a notable observation is the continuous increase in the bulk electron density after the pulsed event. In contrast, the bipolar pulse discharge's bulk electron number density decreases after the input and bulk voltage match, or 17.57 nanoseconds (ns) following this event. Another disparity lies in the bulk voltage: the voltage of unipolar-driven plasma climbs with a positive differential until it matches the input voltage. Meanwhile, the bipolar-driven plasma's voltage initially aligns with the bulk and input voltages at the pulsed event. However, it fluctuates after the pulsed event until the bulk voltage synchronizes with the input voltage 31.20 ns post-pulsation. These variations in bulk voltage evolution are ascribed to the capacitive nature of plasmas operating in the α mode, contrasting with the resistive plasma when operating in the γ mode.

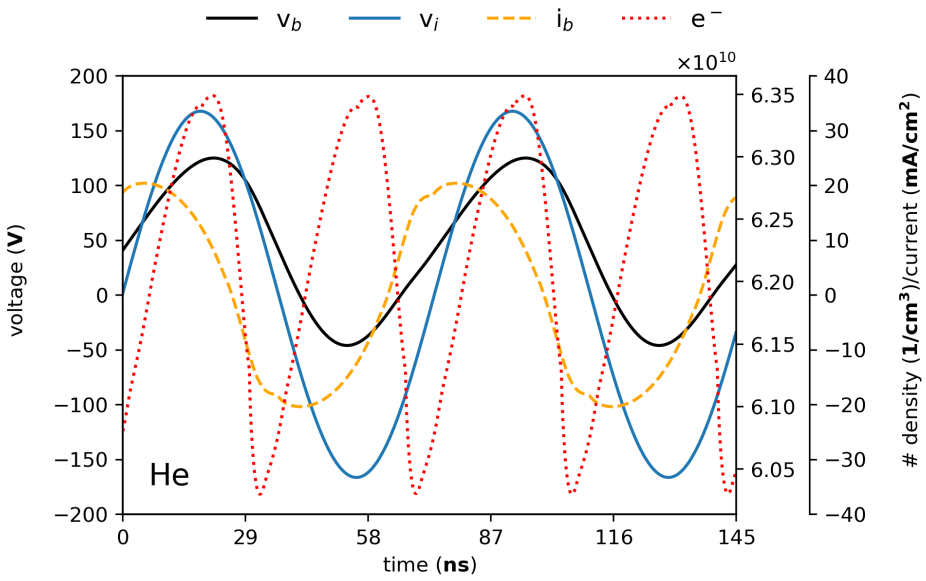

Figure 6.4: Voltage, current density, and number density of electrons for plasmas ignited using a sinusoidal waveform. v_b, v_i, i_b and e^- correspond to the bulk plasma voltage, input plasma voltage, bulk plasma current and electron number density, respectively.

As such, the bulk voltage evolution from unipolar and pulsed discharges can be described as a consequence of their modes of operation. While the unipolar pulsed discharge bulk voltage increment is positive throughout the event, the bulk voltage in the bipolar discharge experiences a decrease followed by an increase until it matches the input voltage. This behavior could indicate that in the α mode, despite a sudden surge of energy, the plasma structure resists sudden changes, as the conductivity is less than that in the γ mode. Such is not the case with the unipolar discharge due to the dramatic increase in conductivity because of its operation in the γ mode, where the impedance encountered is minimized. While the plasmas being analyzed are essentially capacitive due to the frequency of operation, the unipolar and bipolar voltage waveforms illustrate these effects best. As seen in the figure 6.6, the increase in bulk voltage coincides with the drop in bulk current, effectively confirming the nature of the plasma analyzed.

When considering plasma parameters such as displacement current, electron temperature, and sources/sinks within the gap, the spatio-temporal profiles can further verify the modes of operation for the plasma. For the sinusoidal and bipolar pulses, both cases present a clear electron temperature profile with maximum electron energies of 3.63 and 3.40 eV, respectively, and a time-averaged bulk electron energy of 0.50

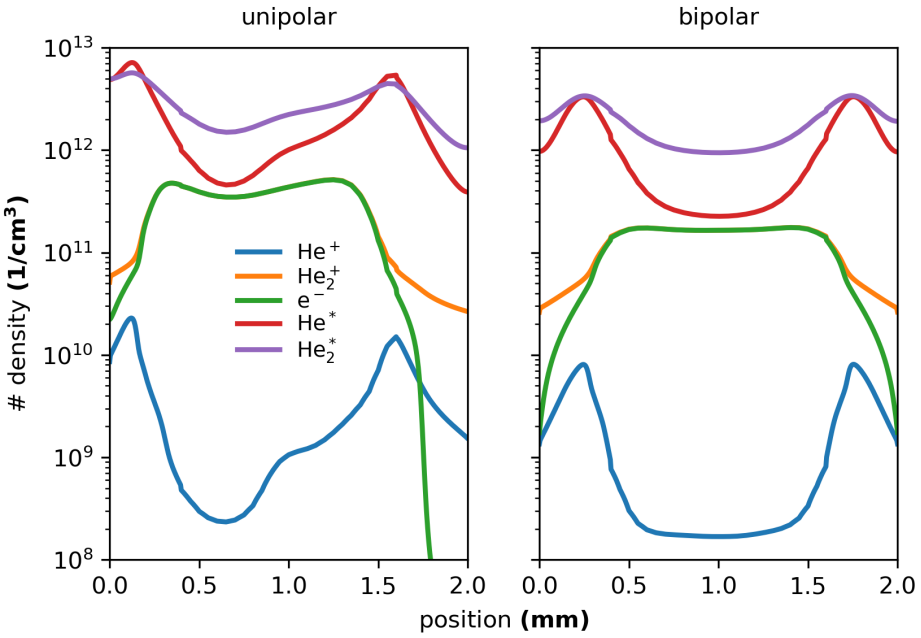

Figure 6.5: Number densities of the helium reaction profile for a unipolar and bipolar ignited plasma.

eV. A sheath/bulk ratio of 7 and 6 is encountered, with the spatio-temporal profiles for both plasmas in the figure 6.7 showing a volumetric distribution. However, in the case of the sinusoidal decay and unipolar waveforms, the maximum electron energy for the sinusoidal decay waveforms (ξ = 0.25, 0.1) and the unipolar-driven plasma corresponds to 5, 4.75, and 4.50 eV, with time-averaged bulk electron energies of 0.25, 0.35, and 0.30 eV, respectively, and sheath/bulk ratios of 20, 14, and 15, respectively. Comparing both ratios, it is evident that the ratios for the plasmas operating in the γ mode are three times that of those in the α mode.

At the same time, figure 6.7 showcases the sinusoidal decay and unipolar-driven plasmas' electron energy distribution localized to the sheath region, in stark contrast to the volumetric distribution shown for the sinusoidal and bipolar plasmas [47]. The electron source/sink spatio-temporal distribution, shown in figure 6.8, highlights significant differences in the intensity of electron activity within the bulk plasma. For the sinusoidal and bipolar plasmas, the bulk region where electron generation occurs has widths of 244.67 μm and 676.13 μm, respectively, with averaged source rates of 10^{15} and 10^{16} cm^{-3} s^{-1}. However, for the sinusoidal decay (ξ = 0.25, 0.1) and unipolar plasmas, the widths of the bulk region where electron generation occurs are 1025.09 μm, 867.36 μm, and 701.51 μm, with averaged source rates of 10^{18}, 10^{17}, and 10^{17} cm^{-3} s^{-1}, respectively. These differences, marked by an increase

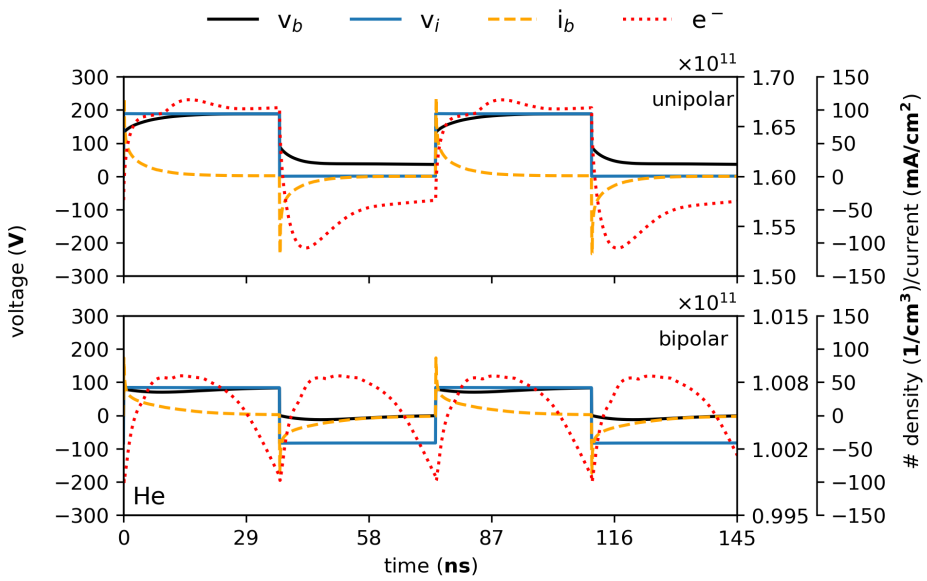

Figure 6.6: Voltage, current density, and number density of electrons for plasmas driven by unipolar and bipolar waveforms. v_b, v_i, i_b and e^- correspond to the bulk plasma voltage, input plasma voltage, bulk plasma current and electron number density, respectively.

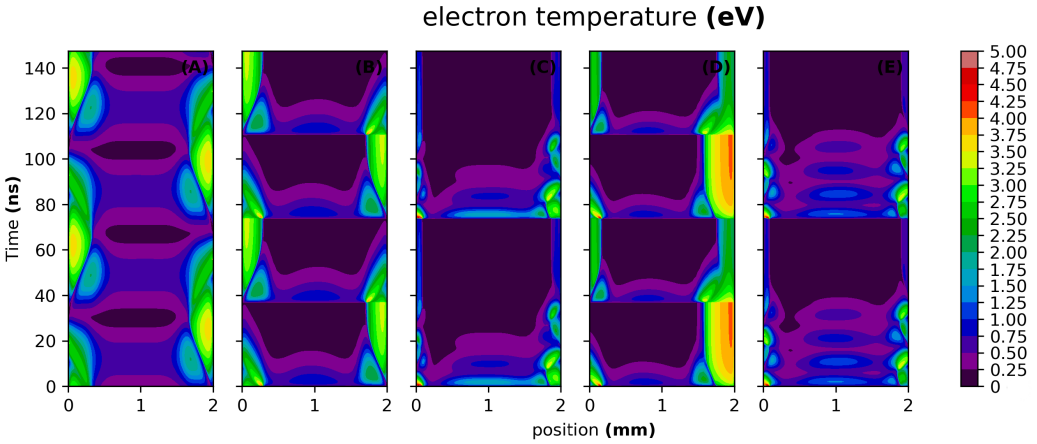

Figure 6.7: spatial-temporal distribution for the electron energy within the helium plasma with different ignition waveforms. **(A)** sinusoidal, **(B)** bipolar, **(C)** sinusoidal decay: $\xi = 0.25$, **(D)** unipolar, **(E)** sinusoidal decay: $\xi = 0.1$.

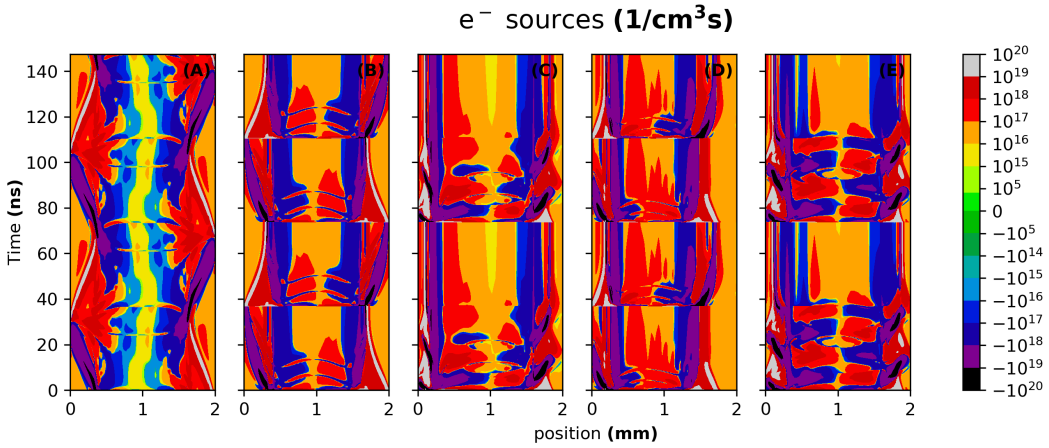

Figure 6.8: spatial-temporal distribution for the source/sink terms for the electron within the helium plasma with different ignition waveforms. **(A)** sinusoidal, **(B)** bipolar, **(C)** sinusoidal decay: $\xi = 0.25$, **(D)** unipolar, **(E)** sinusoidal decay: $\xi = 0.1$.

in the bulk region and intensity of the sources within the bulk region consistent with the decrease in the sheath length as the plasma transitions from the α to γ mode, also match with the increased activity of the bulk region, independently of whether the mode of operation changes from being dominated by the bulk plasma to the sheath region.

While the plasmas analyzed operate with the same average power, their modes of operation and power distribution within a cycle differ depending on the driving waveform. Understanding the power distribution within the plasma is, therefore, important. Figure 6.9 provides insight into the spatio-temporal power distribution within the plasmas. For the sinusoidal case, the generation and consumption of power alternate as the sheath alternates within each half cycle, with power consumption associated with the sheath bias at that moment of the cycle. A similar distribution is observed for its counterpart operating in the α mode, the bipolar-driven plasma. At each pulsed event, the bulk of the power consumption occurs in the sheath region, dependent on the input voltage.

A distinction from the bipolar plasma is that the bulk plasma region increases to an average power of 27 W/cm^3 but quickly dissipates to a power consumption of less than 10 W/cm^3. In contrast, the sinusoidally driven plasma's average power consumption in the bulk region never increases beyond 10 W/cm^3. This discrepancy is due to the pulsed nature of the bipolar discharge, where an instantaneous increase in voltage is encountered, briefly increasing the power distribution across the entire plasma.

In the case of the unipolar pulsed discharge, a higher intensity in the power dis-

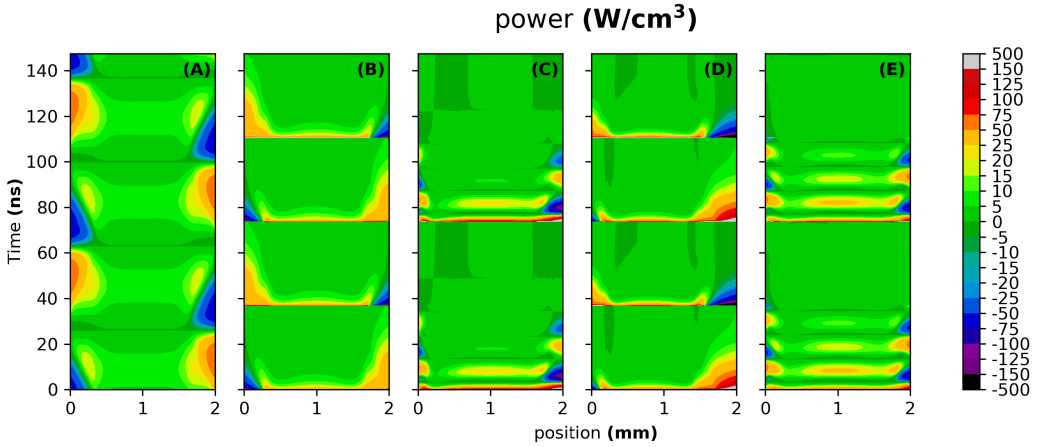

Figure 6.9: spatial-temporal distribution for the power density within the helium plasma with different ignition waveforms. **(A)** sinusoidal, **(B)** bipolar, **(C)** sinusoidal decay: $\xi = 0.25$, **(D)** unipolar, **(E)** sinusoidal decay: $\xi = 0.1$.

tribution across the entire gap is observed, with sheath consumption reaching values close to 500 W/cm^3 at each pulsed event, which then decreases as the ignition progresses. A notable distinction from the bipolar discharge is the quasi-uniformity in power consumption observed in the bipolar sheath, in contrast to the time-dependent changes in the unipolar-driven plasma. During the γ mode of operation, secondary electrons become the dominant source of electron generation due to secondary emissions, as evidenced by the power consumption exceeding 500 W/cm^3 at the onset of the pulsed event. An interesting aspect of unipolar-driven plasma is its lower energy consumption of bulk electrons following the pulsed event, when compared to the sinusoidal decay waveform ($\xi = 0.1$), despite a higher number density in the unipolar waveform. This phenomenon might be attributed to the fact that bulk electron energy is converted more efficiently to joule heating as frequency increases [38]. Such phenomenon is substantiated by sinusoidal decay waveforms operating at an effective frequency of 50 MHz, which display a bulk power of 125 W/cm^3 compared to the average bulk power of 2.5 W/cm^3 seen in unipolar plasma after the pulsed event [38].

As such, the increase in power in the bulk region at the voltage surge event for the sinusoidal decay and pulsed-driven plasmas manifests differently. For unipolar and bipolar waveforms, power consumption is minimized after the pulsed event. At the same time, the sinusoidal decay plasmas exhibit high power consumption in the bulk region after the voltage surge event. Although the sinusoidal decay waveforms' bulk region is more likely to exhibit enhanced joule heating, the increased activity in the bulk region, while enhanced by the increase in frequency, is also a result from the plasma operating in the γ mode. Figure 6.10 showcases the displacement

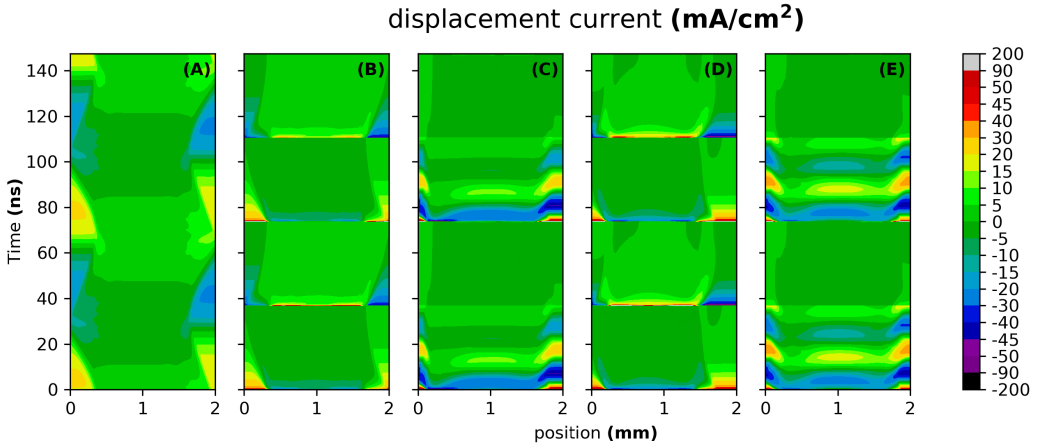

Figure 6.10: spatial-temporal distribution for the displacement current within the helium plasma with different ignition waveforms. **(A)** sinusoidal, **(B)** bipolar, **(C)** sinusoidal decay: $\xi = 0.25$, **(D)** unipolar, **(E)** sinusoidal decay: $\xi = 0.1$.

current of the plasma from a spatio-temporal perspective. It can be seen that while the bulk plasma displacement current is minimal for the sinusoidal waveform due to the quasi-neutrality of the bulk plasma, this is not the case for the sinusoidal decay waveforms, with current densities of 25 mA/cm^2 and 15 mA/cm^2 for the decay waveforms with damping factors of 0.25 and 0.1, respectively, suggesting a deviation from quasi-neutrality.

However, the spatio-temporal electric field distribution for the unipolar and sinusoidal decay discharges, showcased in figure 6.11, indicates that electric field intensity does not significantly increase compared to the sinusoidal and bipolar driver plasmas. While it has been established that the unipolar-driven plasma operates in the γ mode, the displacement current in the bulk plasma remains very low as seen in figure 6.10. This could indicate that while the unipolar-driven plasma operates in an unstable regime, the sinusoidal decay plasmas have effectively arced in the system.

The spatiotemporal electric fields in figure 6.11 establish a relationship between the sheath length of both electrodes and the ignition waveform. The following methodology is utilized to measure the sheath length [45, 130]. While the sinusoidal waveform, due to its operation in the α mode, possesses a sheath length of 0.61 mm, the sinusoidal decay waveforms ($\xi = 0.25$, 0.1) show sheath lengths of 0.35 mm and 0.31 mm, respectively, due to their operation in the γ mode. Simultaneously, figure 6.8 also serves to establish the structure of the plasma, with the sinusoidal waveform having a defined bulk, sheath, and presheath regions, while for the sinusoidal decay waveforms, their mode of operation is that of a plasma operating in the γ mode as these regions are more intertwined, the same being for the unipolar waveform. For

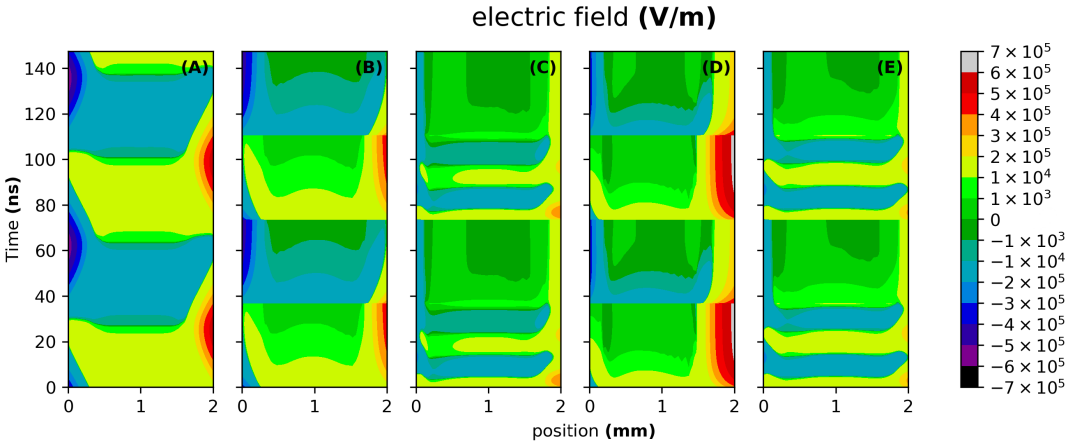

Figure 6.11: spatial-temporal distribution for the electric potential within the helium plasma with different ignition waveforms. **(A)** sinusoidal, **(B)** bipolar, **(C)** sinusoidal decay: $\xi = 0.25$, **(D)** unipolar, **(E)** sinusoidal decay: $\xi = 0.1$.

the bipolar-driven plasma, while the gradient distribution is similar to that of the unipolar-driven plasma, its intensity is not the same, nor is its sheath length, with a defined sheath region on both electrodes compared to the unipolar-driven plasma. At the same time, sheath length of the unipolar waveform is almost half the gap despite effectively operating in the γ mode, indicating the pulsed discharge operates like a DC glow discharge [37, 128, 129, 130]. Further evidence can be gathered by comparing the plasma distributions in figure 6.5 to typical DC discharges, where the sheath length is biased towards the ground electrode.

Although establishing a definitive difference between a DC and unipolar pulsed discharge is beyond the scope of this paper, the parametrization of frequency could provide insights. The bipolar pulsed discharge, while operating in α mode, generates the weakest plasma. Additionally, due to the symmetry of the waveform compared to the unipolar waveforms, both sheath lengths at the two electrodes from a time-averaged perspective are identical, similar to the sinusoidal waveform. However, because of the symmetry in the sheath region, the bipolar pulsed waveform does not operate like a DC glow discharge, in contrast to the unipolar waveform. The sinusoidal decay waveforms do not exhibit this sheath symmetry, biasing towards the ground electrode because of the charge disparity throughout the entire cycle, stemming from the asymmetrical nature of the waveform. Further studies on the parametrization of the frequency of the unipolar decay waveforms would need to be performed to assess a proper operational distinction between a DC and a unipolar pulsed waveform.

6.3 Results for argon

One of the main advantages of argon is that it is a low-cost alternative to helium. As plasma processes become more ubiquitous, expensive gases such as helium might not be viable except for resource intensive industries. Therefore, there is a strong interest in understanding argon characterization at atmospheric pressure. For argon, an operating power of 915 W over an area of 78.15 cm^2 is employed to initiate the argon plasma, the same power utilized to validate the argon simulation compared to the Balcon model [126]. Time-averaged spatial profiles for argon plasma using sinusoidal, pulsed, and sinusoidal decay waveforms are shown in figure 6.12. The bulk number densities of e^- are 6.42 x 10^{11} cm^{-3}, 7.51 x 10^{11} cm^{-3}, 5.40 x 10^{11} cm^{-3}, 1.27 x 10^{12} cm^{-3}, and 9.28 x 10^{11} cm^{-3} for plasma ignited using sinusoidal, bipolar, unipolar, and sinusoidal decay waveforms with damping factors of 0.25 and 0.1, respectively. In other words, the sinusoidal decay waveform with a damping factor of 0.25 generates the strongest plasma, followed by the sinusoidal decay waveform with a damping factor of 0.1, bipolar, sinusoidal, and unipolar. From an efficiency standpoint, aiming to generate the strongest plasma, the sinusoidal decay waveform ($\xi = 0.25$) is the most effective. However, compared to the helium plasmas, some differences exist, as the strength of the plasmas as a function of their waveforms does not follow the same order. In this instance, the sinusoidal decay waveform with a damping factor of 0.1 discharge is the second strongest plasma compared to the unipolar-driven plasma for the helium case. While different feedstock gases and reactor configurations are present, a possible explanation could be the feedstock gas utilized and the plasma characterization of such feedstock gas. Nevertheless, a more comprehensive understanding of operational mechanisms is required, extending beyond mere number densities. A thorough electrical and electron characterization will provide deeper insight into plasma properties and resultant intensity.

Following a methodology similar to that used when analyzing helium plasmas, the shift angle for the sinusoidal waveforms is calculated. Figures 6.13, 6.14, and 6.15 depict the electrical characterization of the sinusoidal decay waveforms ($\xi = 0.25$, 0.1) and sinusoidal waveforms at the midpoint of the gap, which corresponds to the bulk plasma. By measuring the phase shift between the bulk voltage and current, phase shifts of 61.54°, 53.46°, and 82.12° are obtained. These results are similar and comparable to those obtained for the helium waveform. This suggests that for the sinusoidal decay waveforms, the shape of the ignition wave has a more pronounced effect on the electrical characterization of the plasma than the feedstock gas studied.

A stark difference emerges when analyzing the electron number density in the bulk region as a function of time: the electron energy decreases as the pulse discharge diminishes in strength. This behavior suggests that the feedstock gas significantly affects the plasma characterization. Specifically, such outcomes are anticipated because argon plasma requires a larger ignition energy than helium plasma [38, 126]. However, the assumption that electron number density increases post-discharge is

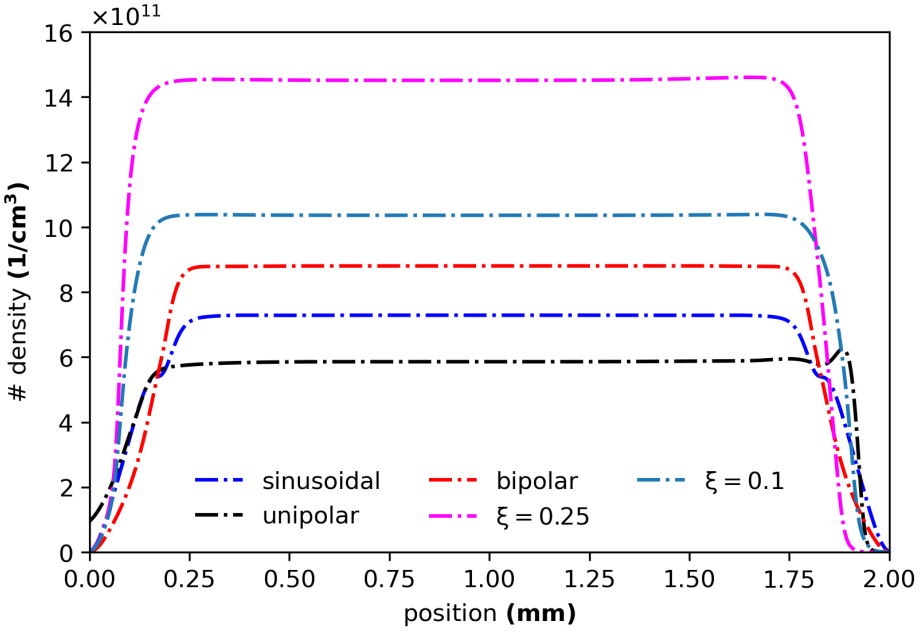

Figure 6.12: Spatio-temporal averaged number densities for e^- under different ignition waveforms.

valid only for the helium plasma under the given ignition conditions. While similar behavior might be observable in argon plasma, it might necessitate a higher power input. This assumption is because electrons in argon plasma lose their energy more rapidly than helium plasma.

The plasma distribution for unipolar and bipolar pulsed waveforms in argon does not resemble that of helium, as illustrated in figure 6.16. Although the unipolar-driven helium plasma is similar to DC discharges, this is not true for the argon-driven pulsed waveforms. For helium, examining the frequency modulation of its plasma might be used determine when the waveform ceases to act like a DC waveform. However, changing the feedstock gas and the power used to ignite the argon plasma alters this characterization. While the electrical characterization remains consistent for sinusoidal decay waveforms, this consistency does not hold for the pulsed waveforms.

A notable similarity between pulsed-driven argon plasma and bipolar-driven helium plasma is observed in the temporal evolution of the bulk plasma following the ignition event. For the bipolar waveform, the bulk plasma voltage matches the input voltage during ignition. It then decreases to its minimum before rising again to align with the input voltage. Figure 6.17 depicts this behavior: the bulk voltage hits its lowest point, 7.83 ns post-ignition, and matches the input voltage, 22.57 ns, after ignition. Apart from the temporal evolution of the bulk voltage, a similarity is also

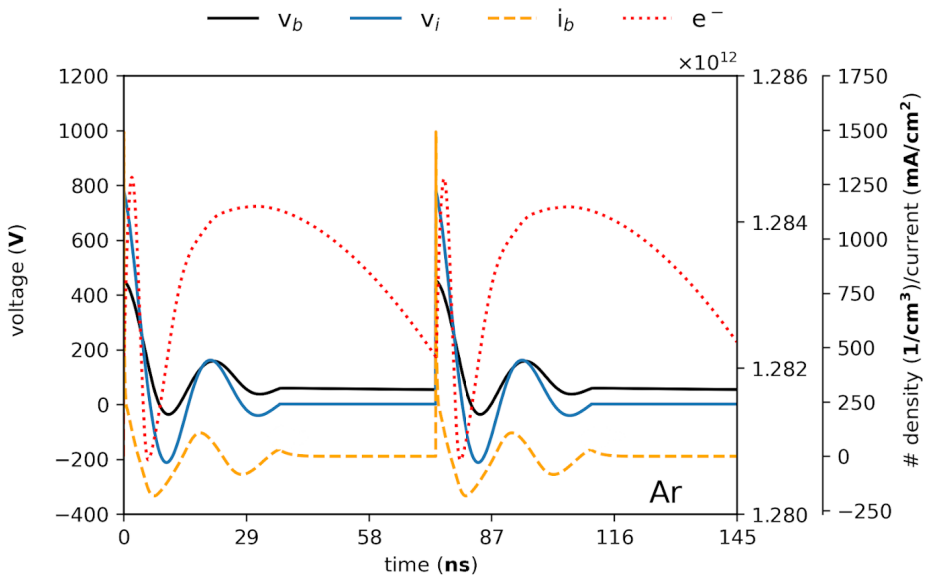

Figure 6.13: Voltage, current density, and number density of electrons for plasmas driven by a sinusoidal decay waveform ($\xi = 0.25$). v_b, v_i, i_b and e^- correspond to the bulk plasma voltage, input plasma voltage, bulk plasma current and electron number density, respectively.

observed in the electron temporal evolution for bipolar ignition waveforms. Thus, plasma behavior driven by the bipolar waveform seems largely independent of the feedstock gas, at least for argon and helium.

However, an anomaly is evident with the unipolar pulsed voltage: despite having a higher input voltage and bulk voltage, its number density is less than that of the bipolar pulsed waveform. This discrepancy can be attributed to the bulk voltage not matching the input voltage compared to the bipolar pulsed discharge and what, indirectly, the data in the helium cases suggest. This leads to the bulk electron temporal characterization diminishing just as the bulk voltage rises, which occurs at 11.12 ns post-pulsed event. Consequently, electron number density increases at 36.78 ns when the input voltage drops to zero upon completion of the duty cycle. In the case of helium, where both unipolar and bipolar waveforms match the input voltage, the power supplied to the argon plasma—although adequate for the bipolar waveform—might be insufficient for the unipolar waveform. This inconsistency can be attributed to argon losing energy more rapidly than helium, causing it to struggle to sustain the intra-plasma reactions. While the expectation of the temporal electron evolution of the argon unipolar-driven plasma might also be possible in helium, to achieve such similarity, less power needs to be supplied to the helium plasma. Nonetheless, a

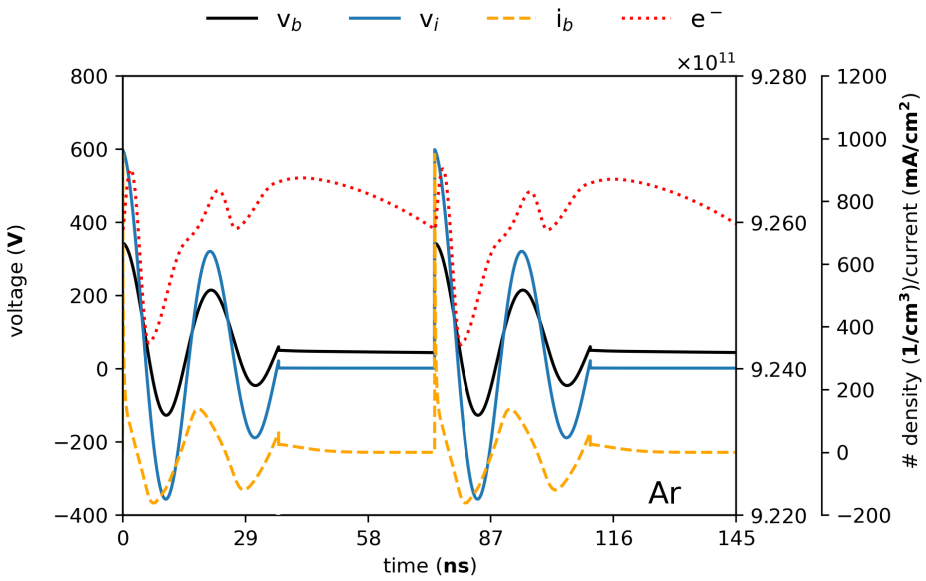

Figure 6.14: Voltage, current density, and number density of electrons for plasmas driven by a sinusoidal decay waveform ($\xi = 0.1$). v_b, v_i, i_b and e^- correspond to the bulk plasma voltage, input plasma voltage, bulk plasma current and electron number density, respectively.

consistent observation for both argon and helium plasmas is that the bulk voltage should match the input voltage to optimize the number of densities. However, it is imperative to exercise caution to prevent a transition from the α mode to the γ mode.

Figure 6.18 is utilized to determine whether the mode of operation observed in the argon plasma aligns with the electrical characterization and to gain a deeper understanding of the temporal bulk electron behavior in the plasma. Consistent with the electrical characterization, the sinusoidal and unipolar waveforms operate in the α mode, showing a volumetric spatiotemporal distribution in the sheath region. For the sinusoidal decay and unipolar waveforms, the energy distributions within the sheath are concentrated in what can be termed "hot spots" of heightened activity [47]. Comparatively, the argon plasma operates at a higher electron energy baseline than the helium plasma: from an average of 1 eV in the bulk plasma region for all waveforms in helium to 2.5 eV for all waveforms in argon. Simultaneously, the energy in the sheath region significantly increases, from an average of 3 eV in helium to 6 eV in argon—a twofold increment. However, the helium plasma remains more efficient in electron generation, requiring less energy to sustain and amplify the electron energy than the argon plasma.

Examining the bipolar waveforms, 7.83 ns post-ignition, we observe the electron

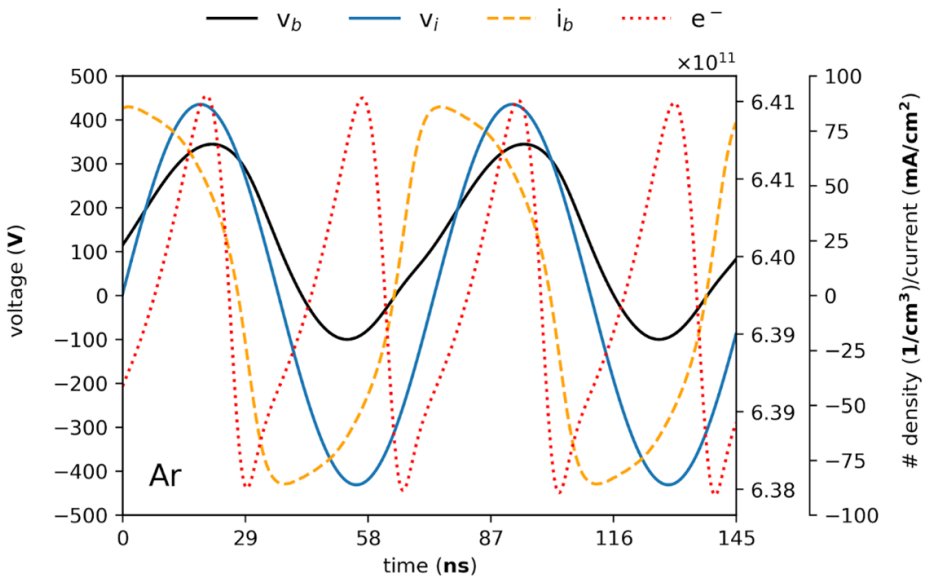

Figure 6.15: Voltage, current density, and number density of electrons for plasmas ignited using a sinusoidal waveform. v_b, v_i, i_b and e^- correspond to the bulk plasma voltage, input plasma voltage, bulk plasma current and electron number density, respectively.

temperature falling from 4.50 eV to a low of 1.25 eV in the bulk region. This decrease in energy aligns with the electron losses as the source reactions become dominated by sink reactions, as seen in table 4.3, effectively reducing electron number densities. In contrast, for the unipolar pulsed discharge, which is more active in the bulk region temporally, the electron number density starts declining 11.12 ns post-pulse, with electron energy dropping from 4.75 eV to 3.75 eV. However, despite observing an uptick in electron energy to 4.25 eV after the input voltage drops to zero at 36.78 ns, the energy in the bulk electron is insufficient to sustain rises in electron number density since its temperature is below 4.75 eV. Concurrently, at this juncture, an increase in electron energy to 5.25 eV is evident in the pre-sheath region of the plasma near the ground electrode. This increase of energy at the pre-sheath facilitates a surge in electron energy, boosting the number density of the bulk plasma as electrons transition from the sheath to the bulk, as seen in figure 6.17. For both unipolar and bipolar waveforms, the sheath plays a pivotal role in plasma generation and its intensity.

Regarding the sinusoidal decay waveforms, the shorter phase shift and reduced stability of the sinusoidal decay waveform with a damping factor of 0.1, compared to the one with a damping factor of 0.25, can be attributed to its heightened activity in the bulk region, both in terms of intensity and spatiotemporal distribution as seen in

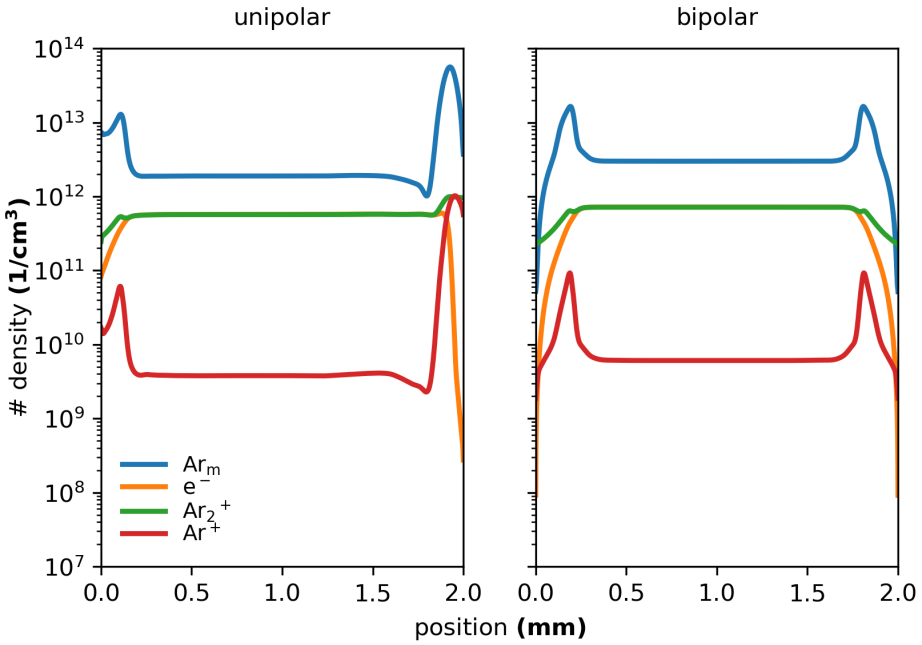

Figure 6.16: Number densities of the argon reaction profile for a unipolar and bipolar ignited plasma.

figure 6.18. A similar behavior is noted for helium, suggesting a consistency, at least between argon and helium plasmas, in the stability of the sinusoidal decay waveform based on its damping factor, favoring a larger damping ratio. Although increased frequency, as observed in helium, augments electron activity in the sheath region and thus joule heating, the damping factor ultimately dominates the observed outcomes.

Figure 6.19 displays the electron sources and sinks for argon. This figure shows distinct bulk, sheath, and presheath regions for sinusoidal and pulsed discharges. In contrast, a noticeable difference emerges when compared with the helium distribution: the electron sources in helium's bulk plasma are more intense than in argon, suggesting that helium plasma ignition is more efficient than argon's at a lower electron energy level.

The displacement current in argon when compared to helium, as seen in figure 6.20, for the sinusoidal decay waveform ($\xi = 0.25$) which generates the most intense plasma for both feedstock gas, it is observed that for argon an increase in displacement current by 40 mA/cm^2, with the sheath values increasing of 100 mA/cm^2, further confirming that the operational requirements of argon are larger than those of helium. At the same time, when assessing the electric field via figure 6.21, an increase in the electric field in the bulk region is observed for the sinusoidal decay waveforms ($\xi = 0.25$) at each ignition event, diverging from the behavior of helium plasma.

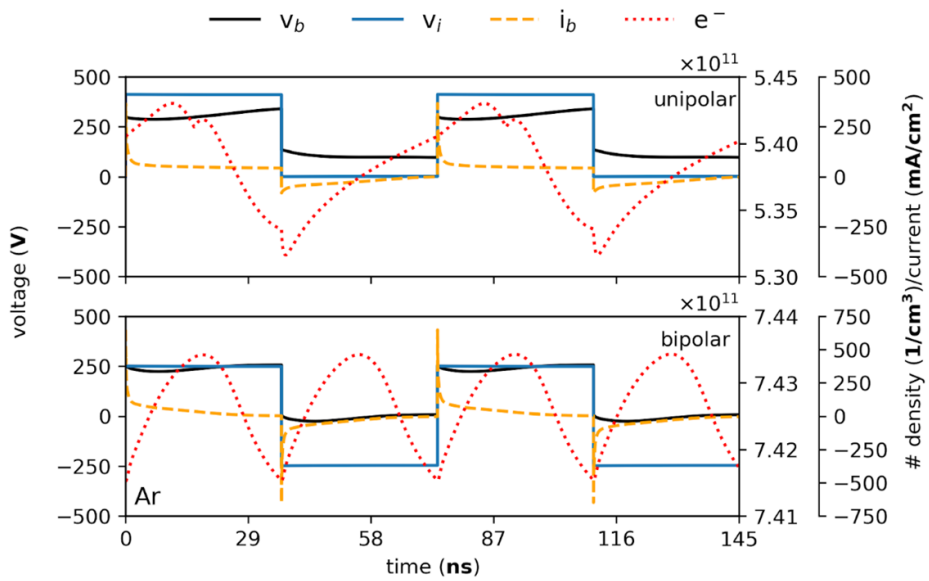

Figure 6.17: Voltage, current density, and number density of electrons for plasmas driven by unipolar and bipolar waveforms. v_b, v_i, i_b and e^- correspond to the bulk plasma voltage, input plasma voltage, bulk plasma current and electron number density, respectively.

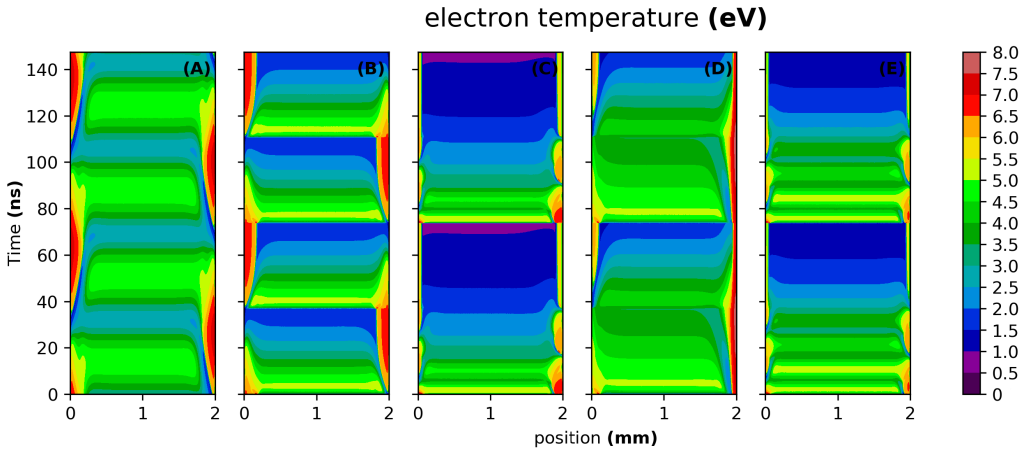

Figure 6.18: spatial-temporal distribution for the electron energy within the argon plasma with different ignition waveforms. **(A)** sinusoidal, **(B)** bipolar, **(C)** sinusoidal decay: $\xi = 0.25$, **(D)** unipolar, **(E)** sinusoidal decay: $\xi = 0.1$.

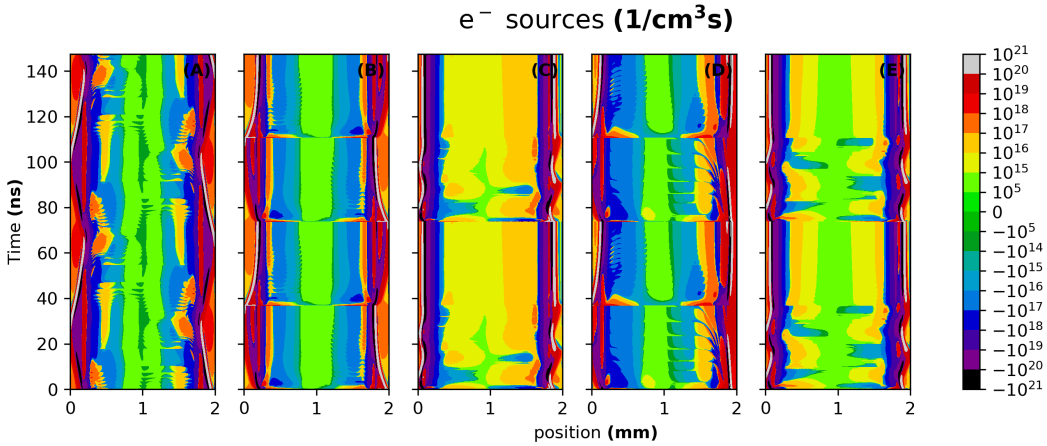

Figure 6.19: spatial-temporal distribution for the source/sink terms for the electron within the argon plasma with different ignition waveforms. **(A)** sinusoidal, **(B)** bipolar, **(C)** sinusoidal decay: $\xi = 0.25$, **(D)** unipolar, **(E)** sinusoidal decay: $\xi = 0.1$.

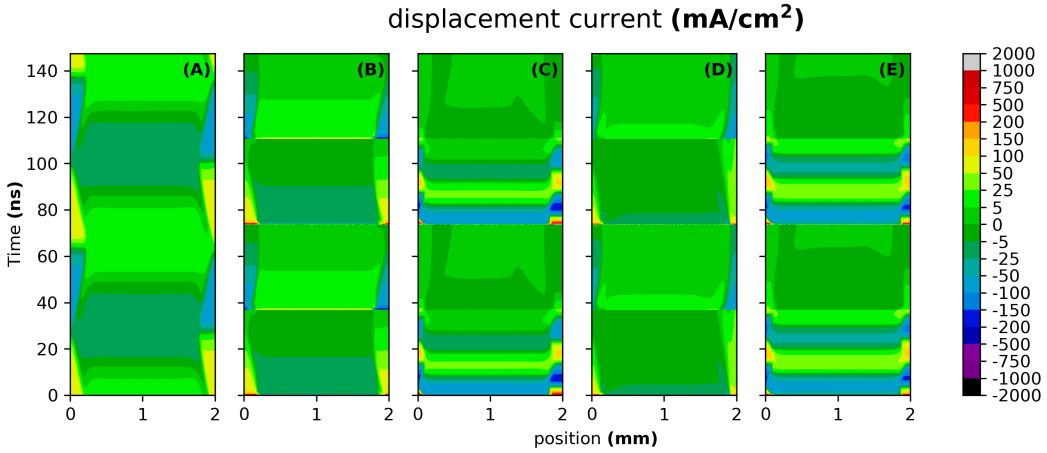

Figure 6.20: spatial-temporal distribution for the displacement current within the argon plasma with different ignition waveforms. **(A)** sinusoidal, **(B)** bipolar, **(C)** sinusoidal decay: $\xi = 0.25$, **(D)** unipolar, **(E)** sinusoidal decay: $\xi = 0.1$.

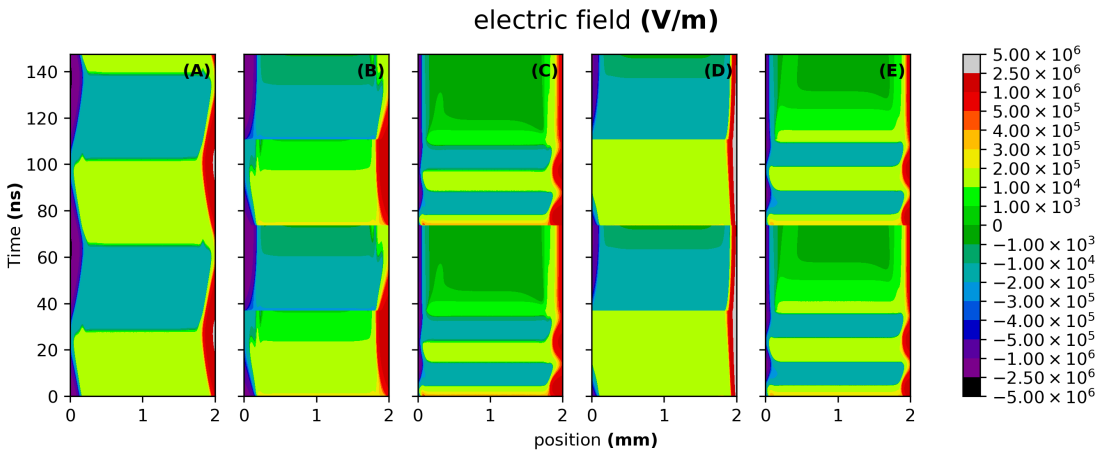

Figure 6.21: spatial-temporal distribution for the electric field within the argon plasma with different ignition waveforms. **(A)** sinusoidal, **(B)** bipolar, **(C)** sinusoidal decay: $\xi = 0.25$, **(D)** unipolar, **(E)** sinusoidal decay: $\xi = 0.1$.

6.4 Conclusion

This study of argon and helium plasmas driven by various ignition waveforms has facilitated the optimization and maximization of number densities. For certain applications, factors like electrical characterization are crucial considerations. A finding of interest was the presence of plasmas operating in the γ mode, identified in both helium and argon plasmas. A consistently observed behavior, irrespective of the feedstock gas employed, was the increased stability of the plasma with a rising damping factor and the stability of pulsed-driven plasmas, as determined by the bulk electron temporal evolution and bulk voltage temporal evolution.

Despite these similarities, differences arise due to the unique properties of the feedstock gases. Helium plasma ignites more easily than argon, requiring a less energetic system for achieving high electron activity in the form of sources and sinks. This distinction results in diverse behaviors in bulk electron temporal evolution, with the argon plasma electron density dropping as the electron energy decreases. Moreover, the argon plasma's higher power demand means that to equate to an area of 78.15 cm^2, a power input of 74.67 W for helium would be necessary — a staggering 12-fold power increment compared to helium. This discrepancy offers insights into the relationship between unipolar and bipolar discharges, emphasizing the importance of aligning bulk voltage with input voltage to maximize number densities.

While helium plasma driven by a unipolar waveform exhibits quasi-DC plasma characteristics, the same cannot be said for argon due to its greater power requirements. This variance underscores the inefficiency of argon plasma relative to helium

in harnessing the delivered power for plasma ignition. Challenges remain, particularly in identifying the boundary between stable and unstable modes of operation for the analyzed waveforms. The aim is to define the operational limits for these plasmas without risking constriction and arcing. Nevertheless, this research offers an exhaustive understanding of the impact of plasma waveforms independent of feedstock gas, providing valuable insights for optimizing plasma processes in various applications.

Chapter 7

α-γ mode of operation

7.1 Setup of simulations

In order to determine the limit between the α and γ modes of operation, an external circuit is set up to model operating conditions consistent with voltage drops after breakdown, as the RF power supply is not an ideal voltage source [126, 54]. If the input voltage at the electrode remains constant, there is a risk of divergence since the operating voltage drops after the breakdown voltage is achieved. Section 3.4 details the setup of the resistor boundary condition, with section 6.1 showcasing the boundary conditions. A resistance value of 50 Ω is used. In this instance, only argon is utilized due to the interest in studying argon as an alternative to helium, given the benefits of using argon over helium. The reactor gap for these simulations is the same as described in section 6.1, with the pressure, background gas temperature, and other conditions remaining constant. For the dielectrics, a dual dielectric configuration, as seen in figure 4.6, is utilized, with a length of 2 mm for each electrode.

For the bare electrodes using sinusoidal, unipolar, bipolar, and sinusoidal damped waveforms ($\xi = 0.25$), as seen in figure 3.11, voltage ranges from 500V to 1000V, 500V to 1000V, 300V to 1000V, and 1500V to 2500V are utilized, with an increment of 20V. For the dielectric case, using the same waveforms as the bare electrodes, the voltage ranges are 500V to 1850V, 500V to 1750V, 500V to 2200V, and 1500V to 4000V, with an increment of 100V for the sinusoidal damped waveform ($\xi = 0.25$) and 50V for the other waveforms.

7.2 Comparison of different ignition waveforms with bare electrodes

One of the main interests in studying the different waveforms is the relationship between power supplied by an external power supply and the critical point of operation

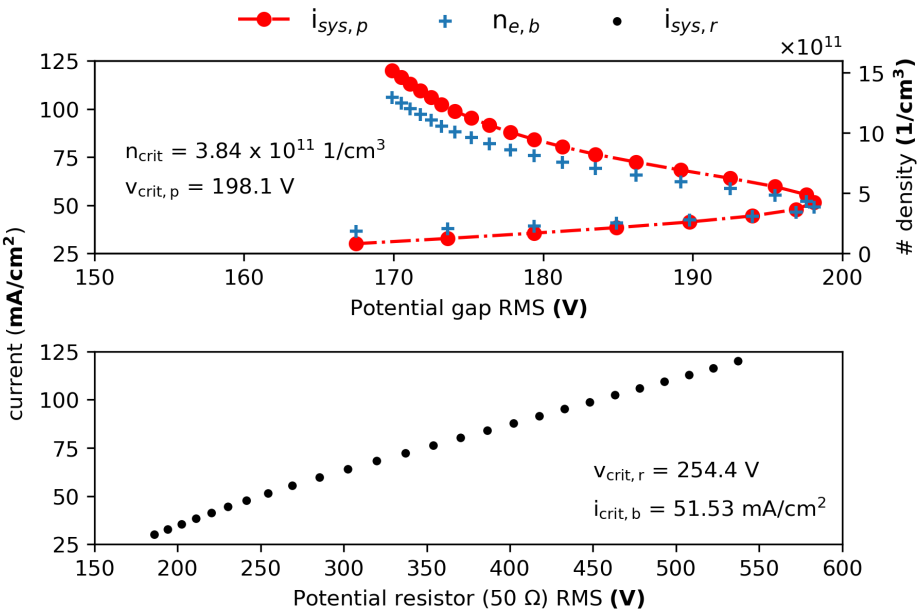

Figure 7.1: Sinusoidal driven plasma voltage and current in gap and resistor.

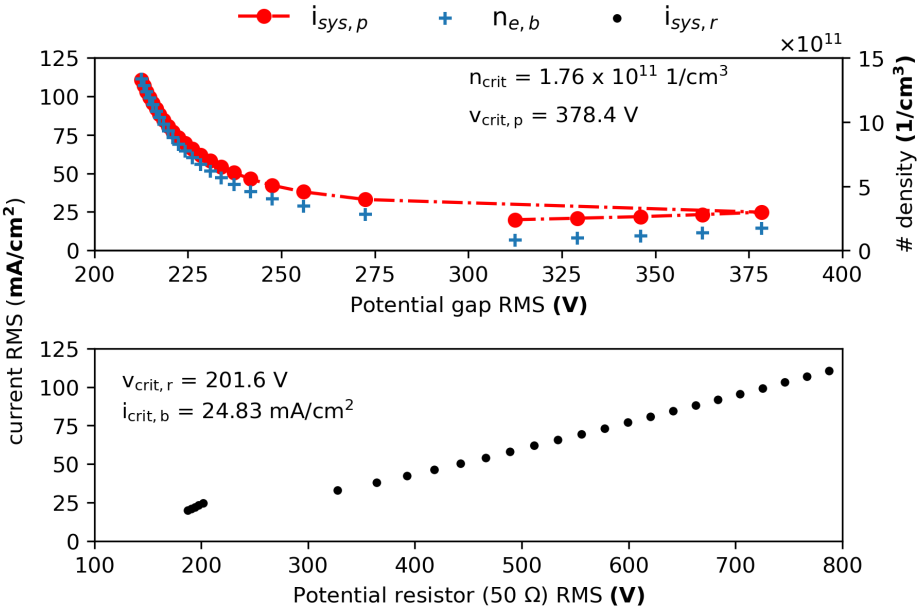

Figure 7.2: Unipolar driven plasma voltage and current in gap and resistor.

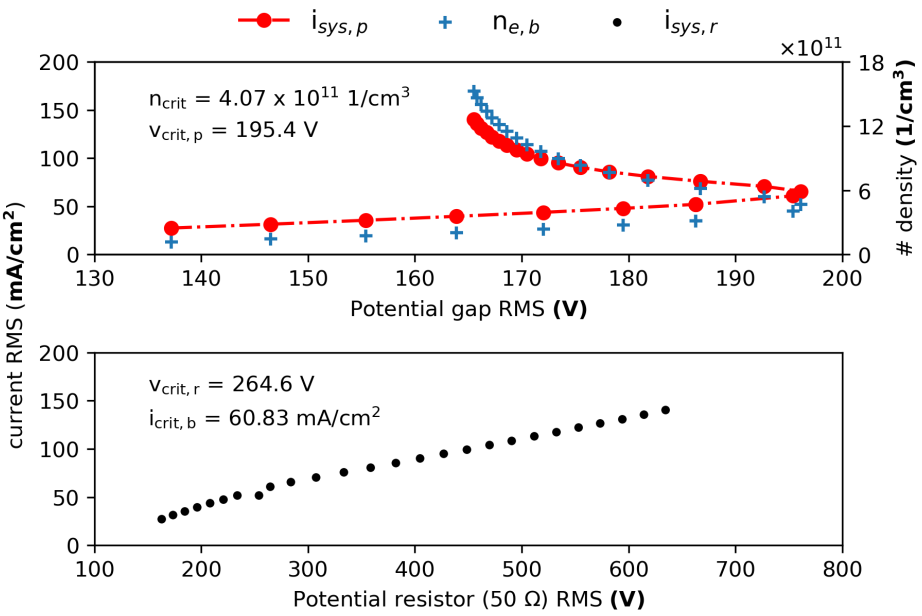

Figure 7.3: Bipolar driven plasma voltage and current in gap and resistor.

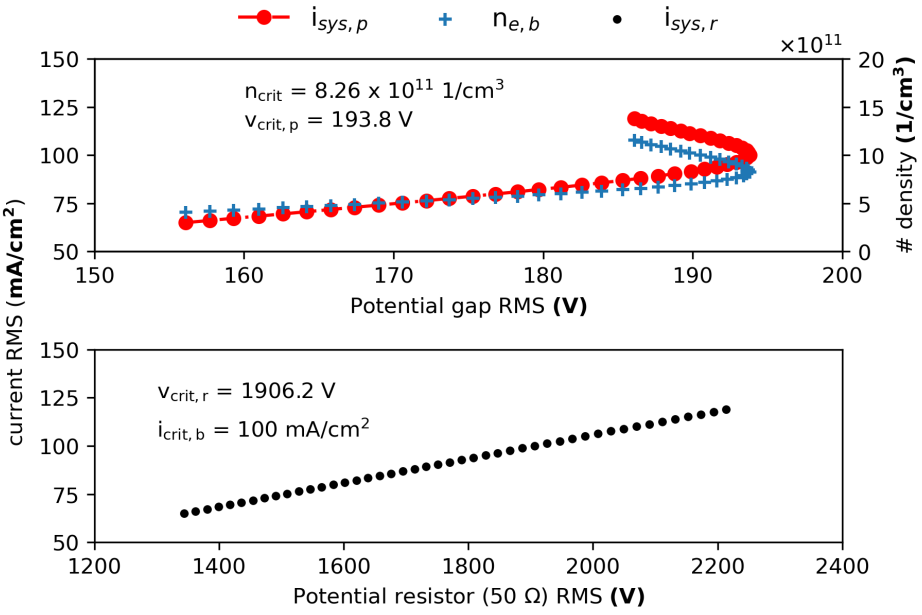

Figure 7.4: Sinusoidal damped ($\xi = 0.25$) driven plasma voltage and current in a DBD configuration.

within a plasma. It is important to minimize power consumption within the system while maximizing plasma number density to achieve power savings and extend the range of operations within a stable plasma. Figures 7.1, 7.2, 7.3, and 7.5 showcase the results for the different waveforms utilized. For the sinusoidal, unipolar, bipolar, and sinusoidal damped ($\xi = 0.25$) waveforms, the number densities at the critical point are 3.84×10^{11} cm^{-3}, 1.76×10^{11} cm^{-3}, 4.07×10^{11} cm^{-3}, and 8.26×10^{11} cm^{-3}, respectively.

It is observed that the sinusoidal damped ($\xi = 0.25$) waveform produces the plasma with the largest number density, allowing for a high range of control from the power supply before instabilities occur. However, power supplies to generate bipolar pulsed waveforms are more readily available compared to those for sinusoidal damped waveforms, which would require custom power supplies, thereby streamlining the plasma process and minimizing operational costs [132, 133, 134, 135]. Additionally, an added benefit of utilizing such waveforms is the granular control over the plasma, as the input voltage, duty cycle, and frequency can be parametrized as needed. Nevertheless, a comprehensive study of the different parameters within the plasma for the various waveforms is still necessary to understand their response to increases in voltage and their overall behavior.

As shown by Balcon and Kong [39, 58], the expected voltage-current profile matches that of figure 7.1, where the voltage gap in the sinusoidal-driven plasma increases until it reaches the critical point, effectively switching the differential conductivity to a negative one, where a decrease in voltage is observed. The same behavior is observed for the unipolar, bipolar, and sinusoidal damped waveform ($\xi = 0.25$), where an increase in voltage within the gap is observed until a critical point is reached, indicating a basic mode of operation regardless of the waveform. Likewise, when operating in the γ mode, the plasma mode of operation changes to one driven by the SEE, where arcing of the system is possible due to the surplus of electrons generated. However, this risk is not as apparent in the lower ranges of the plasma operated in the γ mode. For example, for the sinusoidal waveform, despite operating in the γ mode, the plasma can be pushed up to an input voltage of 720V ($V_{gap,rms} = 189.2$V) before arcing effects are seen, identified by a sudden increase in the differential conductivity [45]. Figure 7.5 showcases the differential of the voltage-current plots, where a steep increase in the slope is seen as the input voltage in the gap decreases. Similar results when studying the transition within the γ mode were also obtained by [45].

For figure 7.5, for the sinusoidal and bipolar waveforms, the plasma in the γ mode is considered stable until a minimum is encountered, from where the plasma starts to become unstable as the current density increases significantly. For the bipolar waveform, the point where the increment in current induces plasma instabilities for an input voltage is 520V ($V_{gap,rms} = 186.7$V). In the case of the unipolar pulsed waveform, while the decrease from a minimum to a maximum is not encountered, this could be due to the voltage stepping in the power supply being too large after the critical point, indicating a need for more data points. On the other hand, the unipolar pulsed

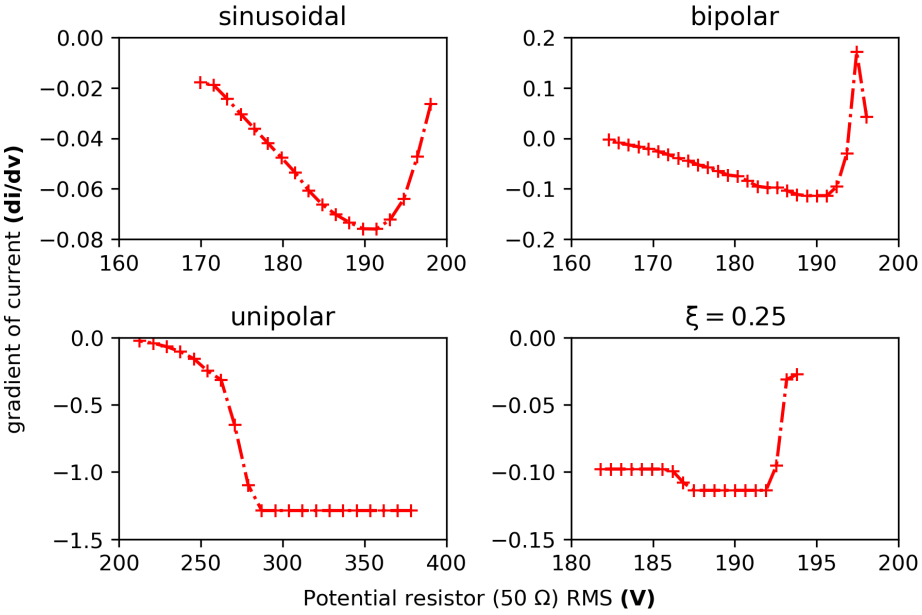

Figure 7.5: γ mode critical stable and unstable point of operation.

discharge reaches the critical point with the lowest number density, indicating that the unipolar pulsed discharge is quite unstable. At an input voltage of 600V ($V_{gap,rms}$ = 272.5V), a step increase of 20V is enough to destabilize the plasma, making it unstable. Referring to the previous study on argon and helium plasma in chapter 6, it was seen that operating at a defined constant power, while the sinusoidal helium discharge would generate a plasma in the α mode, the unipolar pulsed waveform would be operating in the γ mode of operation. The same operation regime was encountered in the argon plasma, indicating that the unipolar pulsed waveform is ineffective when igniting APGD plasmas due to their inherent instabilities. For the sinusoidal damped waveform, it seems there is a drop in the differential as the gap voltage is reduced, flatlining and rising to flatline again, suggesting that for this type of waveform, a very large input voltage from the power supply is required to observe constriction within the plasma. Figure 7.6 showcases the different modes of operation for a time-averaged electron profile. When comparing the sinusoidal damped waveform to the other waveforms, it is clear that the electron profile operating in the γ mode corresponds to a stable plasma in the γ mode of operation. The other plasmas, as seen in figure 7.6, can be distinguished by how they change from a stable plasma at the critical point to a plasma operating at the critical point of the γ mode to an unstable plasma in the γ mode of operation. All these plots can be distinguished by the increase of the electron density in the sheath region for the unstable γ mode of operation, indicating that SEE processes dominate the plasma [45, 47, 126].

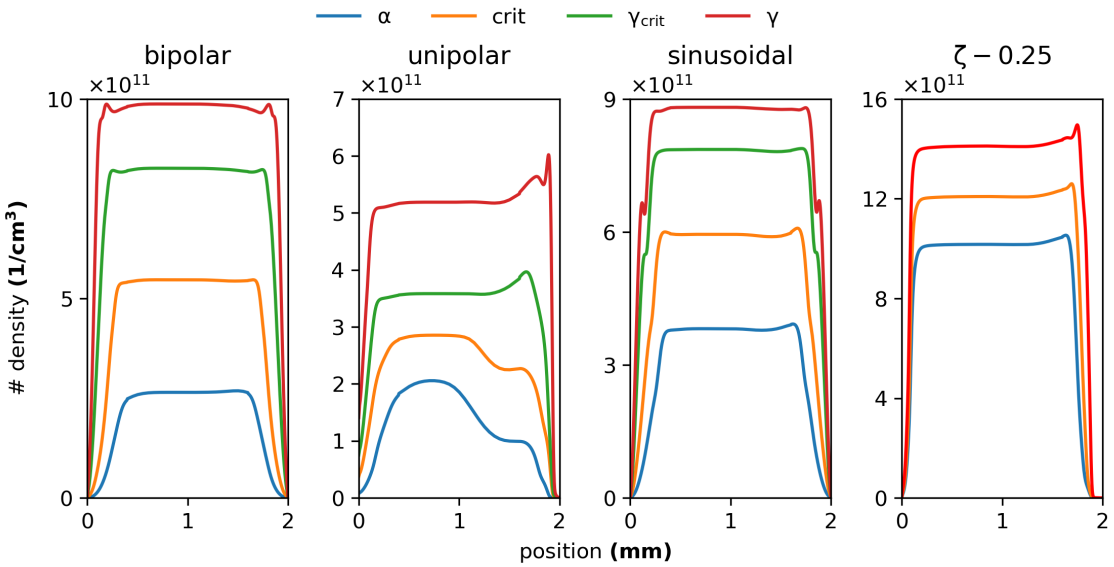

Figure 7.6: Time-averaged spatial profiles of electrons under different operational regimes under the operation of different waveforms. Note that γ for the sinusoidal damped waveform does not indicate instability of the plasma in comparison to the other plots, rather, it indicates operation in the γ mode.

While it was established that the relative instability of the unipolar pulsed discharge is due to the bias in sheath activity towards the ground electrode due to the nature of positively biased discharges [131], previous research also indicates a relationship between the difference in voltage of the bulk and the input electrode at the end of the duty cycle and the intensity of the discharge and mode of operation, as discussed in chapter 6. Although it was established that a bulk voltage matching the input voltage is optimal for maximizing number density, there were limitations with previous observations, particularly the limitation of the power-coupled algorithm, which matches the input voltage to the period-averaged power but fails to consider the effects of external circuits and power supplies as ideal systems. While the power-coupled algorithm provided important insights and agreed with the characterization of the waveforms and the critical number density in terms of constant power and number density obtained, the study was limited in scope regarding the relationship between the input and bulk voltage and its difference at the end of the cycle. Hence, there is a need to study both the electrical characterization of the pulsed waveforms and their bulk/input relationship.

Figure 7.7 and figure 7.8 showcase the plasma's bulk, electrode input voltage, and bulk current for unipolar and bipolar waveforms. A noted difference compared to the unipolar and bipolar electrical characterization from the previous study is

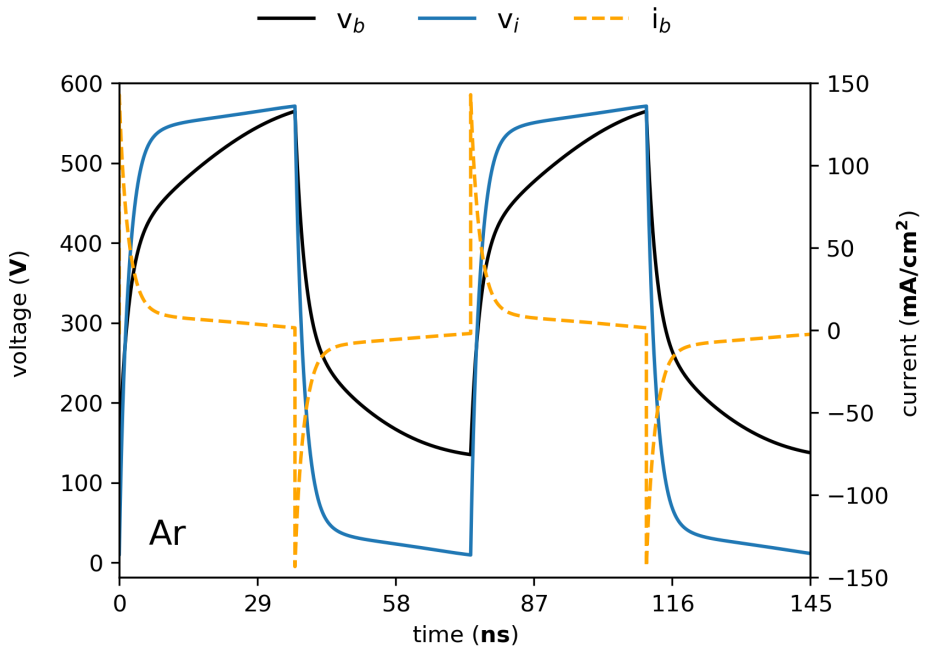

Figure 7.7: Unipolar pulsed discharge electrical characterization at the α-γ transition.

the rise of the input voltage. In the previous study, the input voltage responded instantaneously. In contrast, in this case, due to the presence of a resistive element, the input voltage increases exponentially and later tapers off as it stabilizes. A similar observation is seen with the bulk voltage, where instead of flatlining after the pulsed event, the bulk voltage follows that of the input voltage very closely. This indicates the importance of the resistive element algorithm in improving the modeling conditions of the plasma compared to a direct, power-coupled algorithm operating in an ideal fashion. Nonetheless, the unipolar pulsed discharge maintains a similar behavior to that of the previous study, where the input voltage rapidly stabilizes, and an inverse relationship exists as the bulk voltage matches that of the input voltage, effectively constricting the current density to 0 mA/cm^2 as the plasma, acting as a capacitor, becomes fully charged.

However, a distinctive difference with the power-coupled model is that the current density, when the input voltage is cut off to 0V, increases to the same magnitude as when the ignition event occurred. In contrast, the current response of the power-coupled model is rather weak. By carefully analyzing the plots from both the resistive and power-coupled driven plasmas, it can be seen that the resistance plays an important role, as the bulk voltage response is delayed after the input voltage is cut off to 0V, a byproduct of the input voltage also dropping to a value close to zero

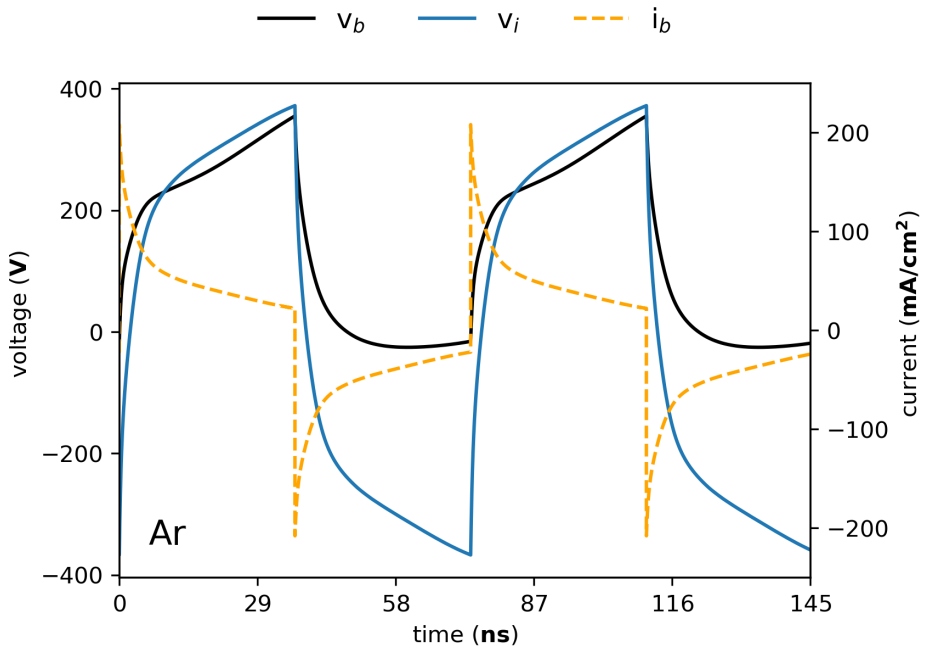

Figure 7.8: Bipolar pulsed discharge electrical characterization at the α-γ transition.

as the resistance delays such a response. As such, a more accurate representation is obtained that closely matches what is observed in experimental setups. In particular, for figures 7.7 and 7.8, which correspond to the critical point of operation before transitioning to the γ mode for both unipolar and pulsed discharges, the input voltage closely matches that of the bulk voltage, as needed to maximize number density for unipolar and bipolar discharges. However, for these two cases, the mode of operation is in the γ mode and the α mode for the bipolar and unipolar pulsed discharges when utilizing the power-pulsed algorithm as done in chapter 6, lacking the discernment if that is the case for the α or γ mode. However, such case is expected as they are operating at different power inputs.

Figure 7.9 and 7.10 showcase the ratio of the bulk and input voltages as the input voltage from the power supply is increased. As seen in both figures, the highest ratio of the RMS bulk and electrode voltage is at the critical point, where the bulk voltage and the input voltage before the end of the duty cycle are closest to each other, as shown in part (b) of Figure 7.9 and 7.10. Revisiting previous studies from chapter 6 for the unipolar pulsed discharge, considering the bulk voltage to the input voltage gap and referring to Figure 7.9, the voltage gap of the plasma operating in the γ mode of operation can be explained. Figure 7.9 shows that the electrode and bulk voltage difference diminishes as it approaches the critical point, with the difference between

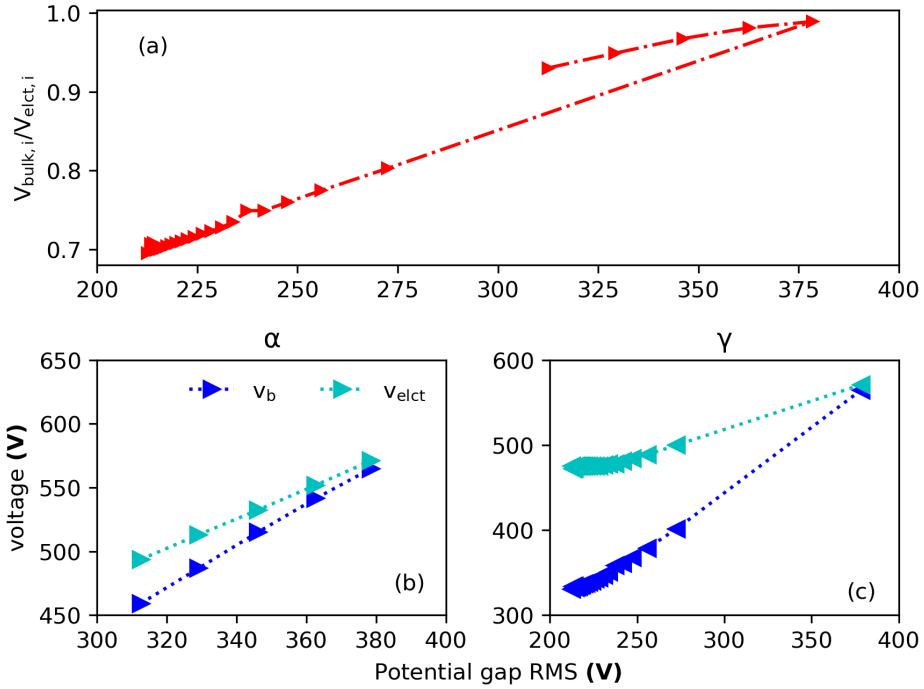

Figure 7.9: Unipolar pulsed waveform voltages at bulk and input electrode.

the voltages increasing as the plasma power input voltage increases in the γ mode, as seen in part (a) of Figure 7.9. While this behavior does not match the helium case from the previous study, where the bulk voltage matches the input voltage despite being in the γ mode of operation, this study should suffice to provide a comprehensive understanding of the argon plasma operating in the α and γ modes and how the relationship between the bulk voltage and the electrode voltage is coupled. At the same time, it was established in chapter 6 that the modes of operation of the argon and helium plasmas are strongly determined by the feedstock gas utilized.

For the bipolar pulsed discharge, as seen in figure 7.8, when comparing the rise and decay of the input voltage to the unipolar waveform seen in figure 7.9, it can be distinctly observed that the input voltage increases in a sloped manner alongside the bulk voltage for the bipolar waveform. In contrast, the input voltage tapers off for the unipolar waveform. At the same time, the sloped increase of the electrode and the bulk voltage difference remains constant for the duty cycle, allowing the current to taper off to a value of 21.13 mA/cm^2, indicating that the bipolar pulsed discharge, when viewed as a capacitor, does not charge completely compared to the unipolar pulsed discharge.

The reasons for such sloping in the input have to do with the bipolar nature of the

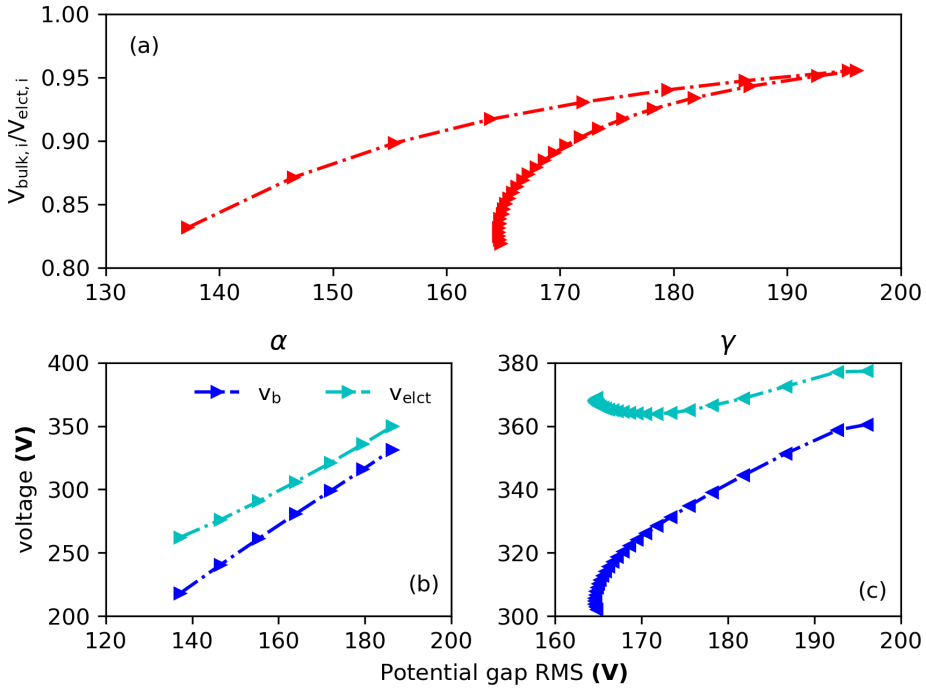

Figure 7.10: Bipolar pulsed waveform voltages at bulk and input electrode.

discharge, where the operation gap for the pulsed event between peaks is 750V. This large gap and polarity cause a delay in the development of the input voltage on the electrode. At a duty cycle of 50%, the bipolar pulsed discharge electrode input voltage does not taper off as in the case of the unipolar pulsed discharge. Hence, the current density of the bipolar pulsed discharge tapers off at 21.13 mA/cm^2 rather than 0 mA/cm^2, explaining both the bulk and electrode voltage increase, which allows for a higher peak current density. After the duty cycle, the stored charge for the unipolar and bipolar pulsed discharge manifests as a current peak. For the bipolar pulsed discharge, the bulk voltage diminishes to almost 0V.

In contrast, the voltage diminishes to 125V for the unipolar pulsed discharge, indicating from the bipolar pulsed discharge that the voltage drop to almost 0V results in a high current flow in the plasma compared to its unipolar counterpart. Additionally, while the voltage drop from the bulk plasma is larger in the unipolar waveform per duty cycle, the time it takes for the bipolar bulk voltage to drop is 22 ns compared to the unipolar waveform, which does not fully taper off at the end of the cycle at 37 ns, as seen in figures 7.7 and 7.8. However, when comparing the drop in the input voltage, the bipolar pulsed drop is larger, allowing the bulk voltage to drop completely. Besides the bias of the sheath region in the unipolar-driven plasma, its electrical characterization is more conducive to stability in the bipolar pulsed

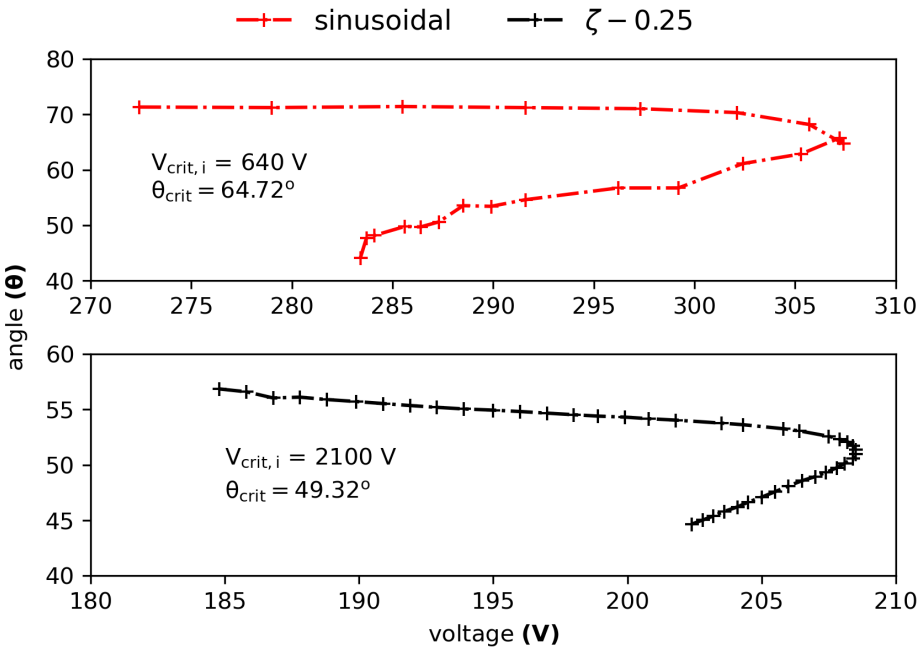

Figure 7.11: Shift angle for sinusoidal and sinusoidal damped waveform ($\xi = 0.25$) as function of input voltage.

waveform than its unipolar counterpart.

For the sinusoidal and sinusoidal damped ($\xi = 0.25$) waveforms, as seen in figure 7.11, the shift angle variation corresponds to whether the plasma is operating in the α or γ mode. Referencing the work by Atanasova et al. [136], it can be determined that the shift angle matches closely in the stable mode of operation for the frequency of operation. Specifically, as seen by Atanasova et al. [136], the shift angle decreases as a function of frequency and number density, which, in the case of the sinusoidal damped waveform, the frequency of operation is 50 MHz, agreeing with the findings of Atanasova. However, as the plasma transitions to the unstable mode of operation, the shift angle decreases significantly as the current increases, showcasing the transition mode where a CCP is encountered to a resistive plasma. Such insights are important as that is the expected mode of operation for an AGPD CCP, where the capacitive mode dominates the α mode.

However, differences in behavior can be seen in the sinusoidal and sinusoidal damped waveform. For the stable mode of operation, the shift angle remains more or less constant until the critical point, when the shift angle starts to decrease. On the other hand, the sinusoidal damped waveform ($\xi = 0.25$) shift angle linearly decreases until the critical point is encountered. Factors such as the frequency of operation

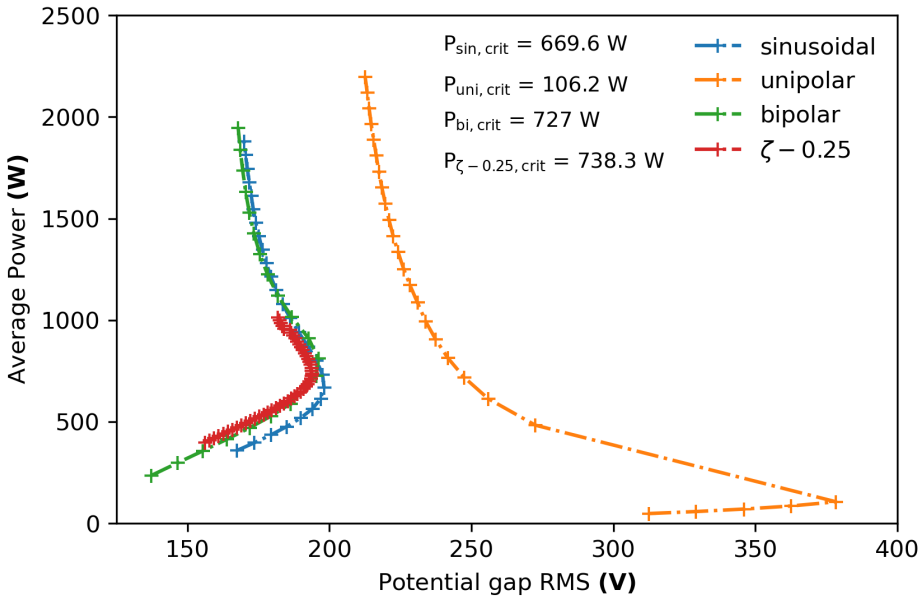

Figure 7.12: Operating power of different ignition waveforms.

and number density of the plasma at the stepped voltage influence such results, as seen by the maximum number density of the plasma at the critical point. A twofold increase in number density is observed when comparing the number density to the sinusoidal waveform. As such, this difference also affects the shift angle in a reduced manner, as the magnitudes of number densities are larger than that of the sinusoidal counterpart, which affects the shift angle in the α mode of operation.

A point of interest in utilizing different ignition waveforms is the power required to ignite the plasma and maximize the plasma number density while minimizing power consumption to generate an efficient plasma and minimize instabilities and arcing. Figure 7.12 showcases the power curves as a function of the voltage gap for bipolar, sinusoidal, and sinusoidal damped waveforms ($\xi = 0.25$). The operating values are very close to each other before arcing events occur, with the sinusoidal waveform operating at a power input of 68.7 W less than the sinusoidal damped waveform, while at the same time, that difference allowing for a twofold increase in the plasma density for the sinusoidal damped waveform. Also, the sinusoidal damped and bipolar waveforms show a difference of 11.3 W before operating in the γ mode, with the bipolar waveform having a slight increase in the number density. However, consideration of the power losses of the external circuit is also required to accurately determine the load on the system. For the sinusoidal, bipolar, unipolar, and sinusoidal damped waveforms, the average power losses per cycle due to an external circuit with a resistance of 50 Ω, referencing figures 7.1, 7.2, 7.3, and 7.5, are 2371.57 W, 798.86

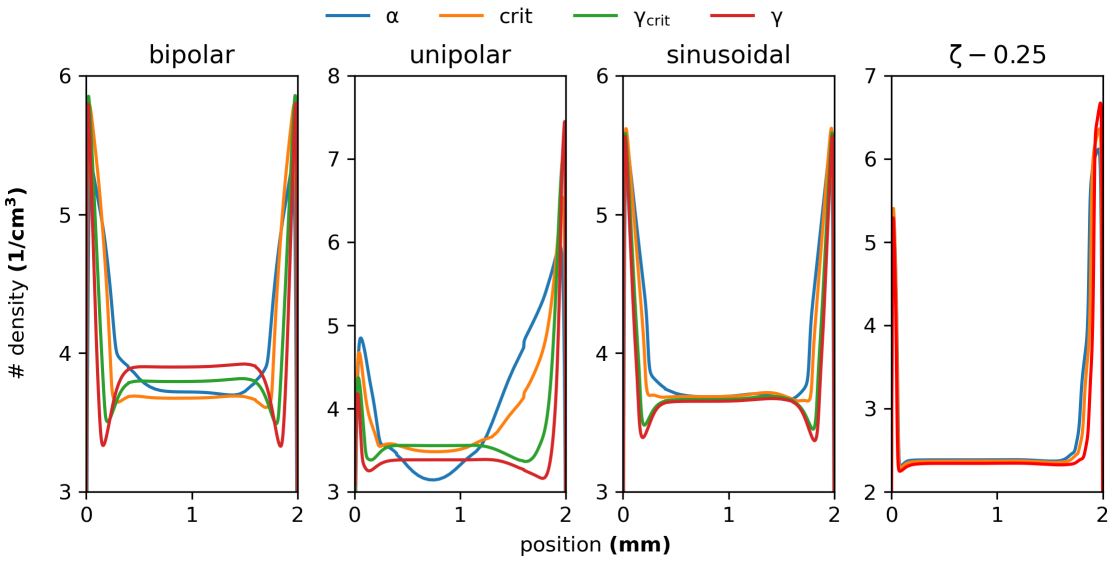

Figure 7.13: Time-averaged spatial profiles of electron temperature under different operational regimes under the operation of different waveforms. Note that γ for the sinusoidal damped waveform does not indicate instability of the plasma in comparison to the other plots, rather, it indicates operation in the γ mode.

W, 192.34 W, and 3207.23 W, respectively. While in hindsight, the sinusoidal pulsed waveform is the most inefficient when considering the high power losses within the resistance, the nature of plasmas driven at a higher frequency, which the sinusoidal damped waveform is at 50 MHz, explains the aforementioned phenomenon where higher power is required to drive the plasma at a high number density [38]. At the same time, the power required to ignite the sinusoidal plasma indicates that such a waveform is not the most efficient way to ignite the plasma. This has become an issue when trying to ignite APGD CCP. Hence, there is a need for alternatives that can minimize power usage while maximizing the plasma number density. As such, the bipolar-driven plasma strikes the best balance between an adequate number density and power utilization, with a total power utilization of 1525.86 W, lower than the sinusoidal waveform. Therefore, unless an application requires a number density larger than that of the bipolar pulsed waveform at its critical point, the aforementioned waveform should be able to strike a balance between the reactivity of the plasma and power utilization. The unipolar waveform is not considered due to its inherent instability caused by the bias of the sheath at the ground electrode, which accelerates the transition of the plasma to the γ mode of operation.

Figure 7.13 showcases the differences in the electron energy distribution using different ignition waveforms. The sinusoidal waveforms follow a behavior where, while

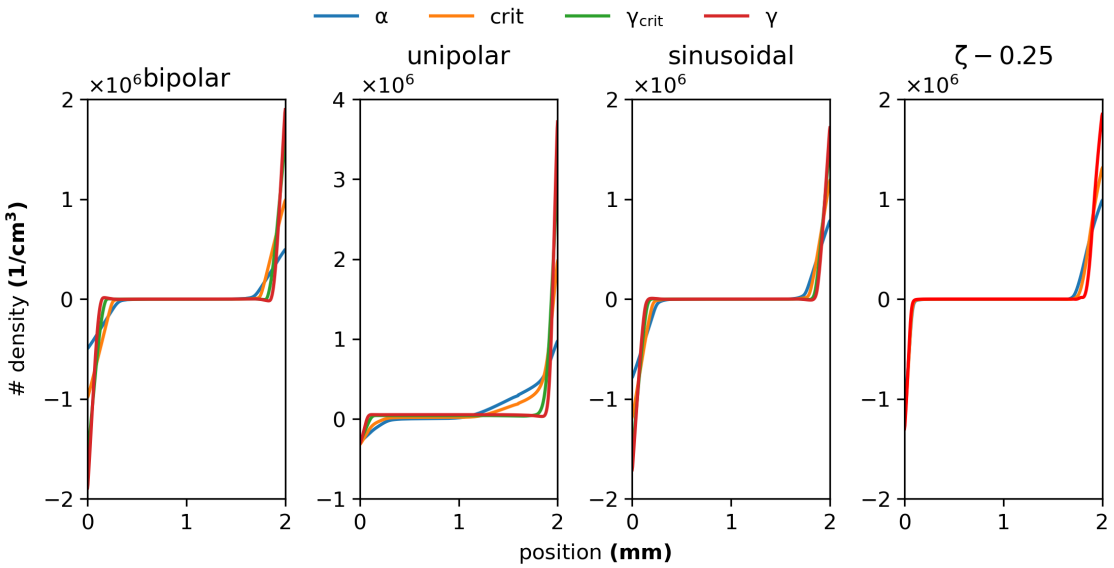

Figure 7.14: Time-averaged spatial profiles of plasma electric field under different operational regimes under the operation of different waveforms. Note that γ for the sinusoidal damped waveform does not indicate instability of the plasma in comparison to the other plots, rather, it indicates operation in the γ mode.

the bulk constant density more or less stays the same, the energy of the electrons in the pre-sheath regions decreases as the intensity of the plasma increases. The electron energy is considered the highest in the sheath region due to the large electric fields and the contribution of SEE. However, because of the energy losses of the electrons in the pre-sheath region, the maximum electron energy peaks at the critical point and decreases as the current increases.

For the unipolar pulsed discharge, the changes in the temperature profile are significant as it reaches the γ mode compared to the α mode, where the pre-sheath region losses become substantial as the generation of charged species increases. Due to the very high electric field found in the unipolar pulsed discharge, as seen in figure 7.14, the unipolar pulsed waveform is inherently unstable. In the case of the bipolar pulsed waveform, the duality of the bipolar waveform prevents the effects observed in the unipolar waveform. However, unlike the sinusoidal waveform, where the bulk voltage decreases as the current increases, for the bipolar waveform, the bulk plasma energy increases with the current. This can be explained by the duality of the pulses in the bipolar waveform, where the sheath region does not bias towards a particular region, and the voltage does not drop to 0V as in the unipolar waveform, allowing for stable plasma but also, as the bipolar waveform is not continuous, allowing for an increase on the energy in the bulk region as the electrons are contained within

the bulk region. While electron trapping is already an effect operating at the RF frequency regime, these effects are stronger due to the bipolar waveform. In the case of the sinusoidal pulsed waveform, the electric field, as seen in figure 7.14, while biased towards the ground electrode, is not as intense as that of the unipolar waveform, further showcasing the benefits of varying the voltage potential. An important observation is the slight variation in the electron profile, as seen in figure 7.13, where the profile shape essentially does not change. Notably, while the electron energy at the ground electrode is as large as that of the unipolar waveform, the number density at the critical point is almost five times larger than that of the unipolar waveform. Highlighting the frequency of operation of the sinusoidal damped waveform and how a plasma operating at a higher frequency can operate with higher input power while remaining stable, for applications requiring maximum number density, the sinusoidal damped waveform would be utilized to achieve such goals. While this study does not compare the sinusoidal damped waveform to a sinusoidal waveform operating at 50 MHz, figure 7.13 suggests that the sinusoidal power drive would be even greater than what was observed with the sinusoidal damped waveform, making the sinusoidal damped waveform an efficient way to drive a plasma at a high frequency.

7.3 Dielectric barrier discharge

The analysis of ignited plasmas in the processes of a DBD should provide insights into whether it is appropriate to use them to increase the number density when using an ignition waveform compared to bare electrodes. As seen in figures 7.15, 7.16, and 7.17, there is an increase in the reactivity of the plasma in the presence of the dielectric compared to using only bare electrodes. For figure 7.18, which corresponds to the sinusoidal damped waveform, there is a decrease in number density. At the same time, the α-γ critical point is not seen as in the case of the bare electrodes, where the differential conductivity becomes negative after the critical point. Kong's [58] studies on experimental RF DBD plasma match the behavior shown in the simulations, where, as the transition in the plasma reaches the γ mode, its slope changes rather than changing the differential conductivity. Compared to the bare waveforms, there was an increase in the number density of 24.47%, 22.15%, and 6.63% for sinusoidal, unipolar, and bipolar, respectively.

In contrast, there was a decrease of 10.72% for the sinusoidal decay waveform. A reason for the decrease in number density can be ascribed to the presence of the dielectrics, which affects the temporal characterization of the sinusoidal damped waveform. The dielectric, acting as a ballast, collects charge within the system, increasing the voltage such that the dielectric plasma voltage is larger than that of the voltage-resistance interface. While this indicates that a larger voltage is utilized to ignite the plasma, the charge accumulation in the dielectric, as the damping factor attenuates the input voltage, also affects the voltage characterization on the plasma-dielectric

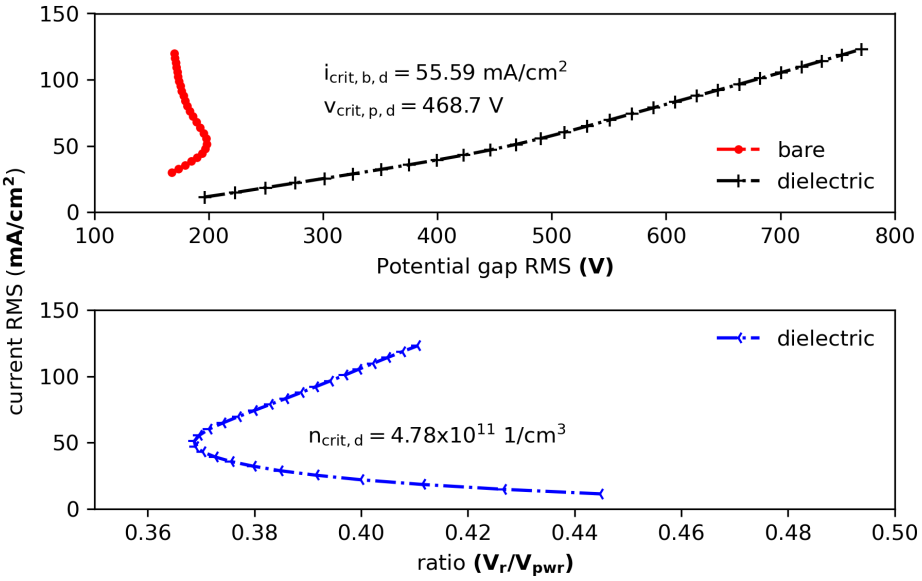

Figure 7.15: Sinusoidal driven plasma voltage and current in a DBD configuration.

interface. This reduces the effectiveness of the waveform, as the damping factor characterization of the sinusoidal damped waveform is indirectly affected by the charge accumulation in the dielectric. Effectively, the damping factor is reduced as the charge accumulated in the dielectric acts to stabilize the plasma, making the attenuation in the voltage within the plasma less forceful. The dielectric's presence also makes the plasma's operation consume more power, with the potential gap increasing by an average of 5 to 7 times compared to the bare electrodes.

However, when comparing the power consumption of the dielectric to that of the bare electrode, these values are very similar. By analyzing figure 7.19, a decrease of 3.06%, 1.69%, and 26.80% and an increase of 113.74% were obtained for sinusoidal, bipolar, sinusoidal damped, and unipolar waveforms, respectively. This indicates a similar operation power input except for the sinusoidal damped and unipolar waveforms, which can be explained by the effects of the dielectric presence on the characterization of the waveforms within the plasma. What is of interest is that the minimal power variation is seen for the bipolar and sinusoidal waveforms, indicating that the symmetry of the ignition waveform disallows for variation in power, compared to the unipolar and sinusoidal damped waveforms, which are asymmetric in comparison to the former, and a power difference is seen.

This can be explained by the biases at each half period and the effects that have on the electric field, which can be seen in figure 7.14 for the sinusoidal damped and unipolar waveforms, which have similar behavior to that of the dielectric cases. As

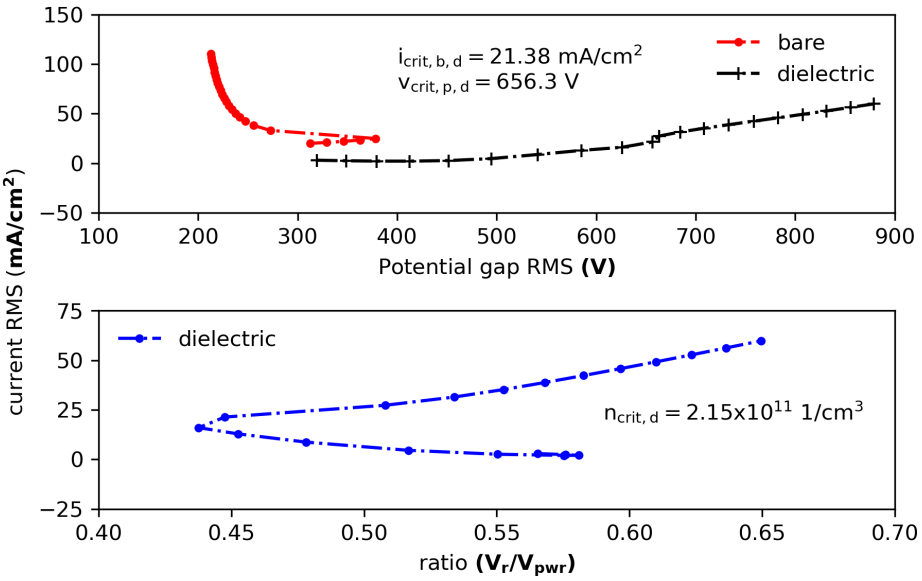

Figure 7.16: Unipolar driven plasma voltage and current in a DBD configuration.

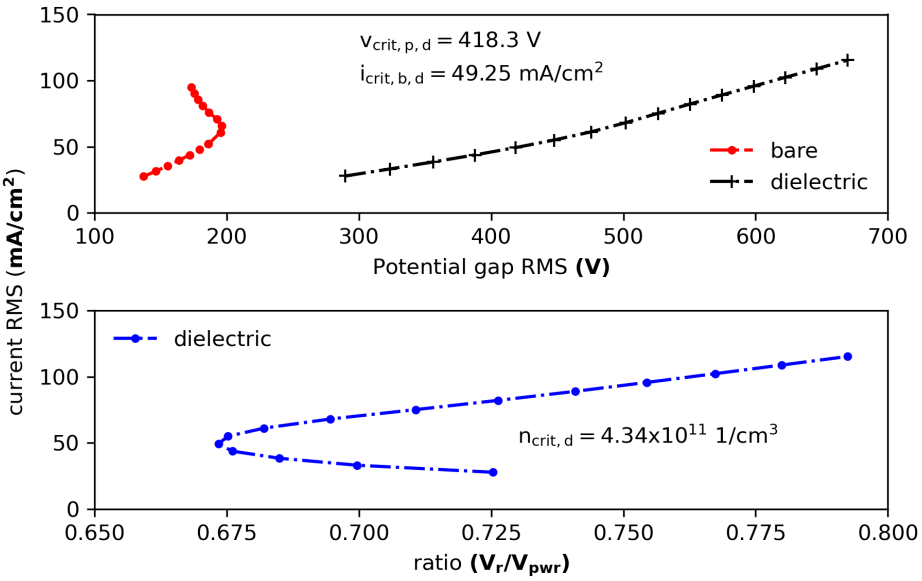

Figure 7.17: Bipolar driven plasma voltage and current in a DBD configuration.

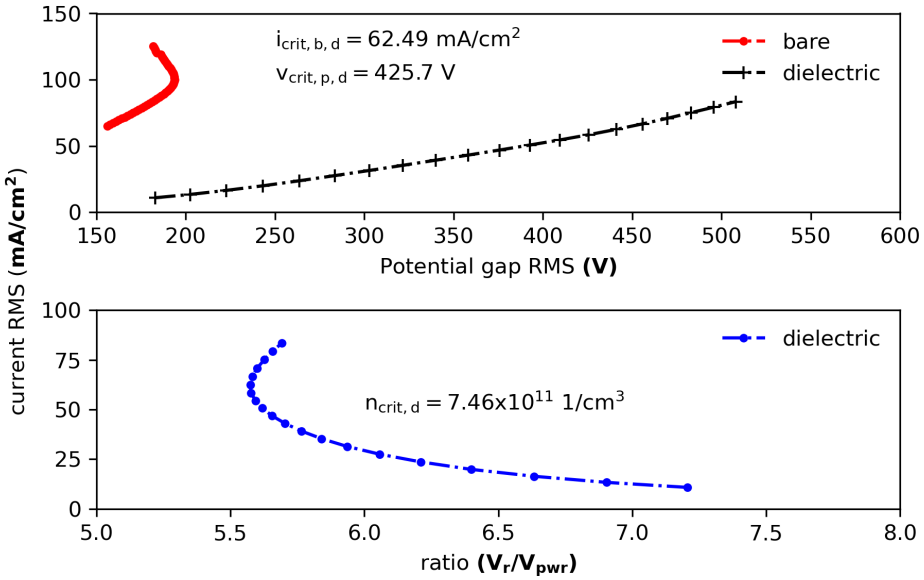

Figure 7.18: Sinusoidal damped ($\xi = 0.25$) driven plasma voltage and current in a DBD configuration.

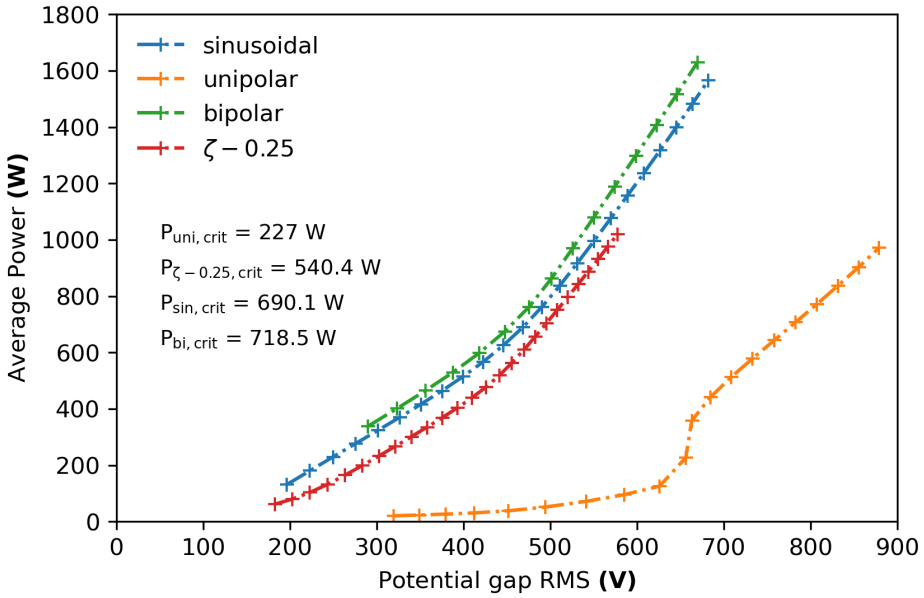

Figure 7.19: Operating power of different ignition waveforms under the presence of a dielectric.

such, this indicates that for waveforms that are not symmetric, there is a larger range of play with the waveform to optimize the operating parameters compared to those that are symmetric, as is the case for sinusoidal and bipolar waveforms. Nonetheless, the limitations for obtaining a larger plasma density are seen in the sinusoidal damped waveform, where a lower number density was obtained, requiring investigation of different parameters to optimize the ignition waveform to that of its bare electrode configuration.

7.4 Conclusion

The study of α and γ modes of operation within various plasma ignition waveforms—sinusoidal, unipolar, bipolar, and sinusoidal damped—has provided significant insights into optimizing plasma characteristics for different applications. By implementing an external circuit to model realistic operating conditions, we observed distinct behaviors in the voltage-current profiles and number densities at critical points, particularly noting the advantages of the sinusoidal damped waveform in achieving higher plasma densities with relatively stable operation. The unipolar pulsed discharge exhibited inherent instability, primarily due to the bias in the sheath activity towards the ground electrode. In contrast, the bipolar pulsed discharge offered a more stable operation due to its balanced nature.

The presence of dielectrics further complicated the plasma dynamics, particularly affecting the sinusoidal damped waveform by altering the temporal characteristics due to charge accumulation. Despite these complexities, dielectric configurations generally enhanced the plasma's reactivity compared to bare electrodes, though at the cost of increased power consumption. Symmetric waveforms like sinusoidal and bipolar showed minimal power variation with dielectrics, whereas asymmetric waveforms like unipolar and sinusoidal damped exhibited significant changes.

Overall, the findings highlight the critical role of waveform symmetry and external circuit considerations in optimizing plasma performance. The study underscores the necessity of a tailored approach in selecting and tuning ignition waveforms based on the specific application requirements, balancing the need for high plasma density and stable operation against power efficiency and system complexity. Future research should continue to explore these dynamics, particularly in refining the sinusoidal damped waveform and further investigating the impact of dielectric materials on plasma behavior.

Chapter 8

Dynamic mode decomposition for plasma modeling

8.1 Setup of simulations

The modeling parameters for generating the database to train the dimensional reduction algorithm are as follows: 1 Torr, 1 cm, one dimension, argon feedstock gas with the reaction set shown in table 4.4. A SEE of 0.01 is utilized for the electrons, alongside a SEE energy of 5 eV. A background temperature of 300 K is used. An external circuit with a resistance of 50 Ω is utilized for the input voltage. These conditions were selected to simplify the argon model to evaluate the viability of the DMD algorithm in predicting and parametrizing plasma operating conditions and because they reflect typical operating conditions found in the semiconductor industry [41, 43, 19]. Given the interest in reducing computational downtime while optimizing solutions, the pressure was chosen based on expected operating conditions in the industry. A Courant condition is utilized to control the time step. Data is saved every 5×10^{-10} s as DMD requires equal time steps. After the simulation using a sinusoidal voltage of a determined value, the Gaussian pulsed effects, as seen in figure 3.12, are applied by superposing the sinusoidal waveform to increase the number density of the plasma up to 16 cycles, where the simulation is stopped.

For the operating conditions of the sinusoidal ignited plasma, voltages of 150V, 200V, 225V, 230V, 240V, 245V, 250V, 300V, and 450V are applied. The following voltages are applied for a sinusoidal input of 300V with a single positive pulse in the next cycle: 750V, 1000V, 1250V, 1500V, 1750V, 2000V, 2250V, and 2500V. The same voltage conditions are provided for a single negative pulse, except with a sign change for the pulse with a sinusoidal input of 300V. For a sinusoidal input of 300V followed by a positive pulse cycle and a negative pulse cycle, the following voltages are used: 750V, 1000V, 1250V, 1500V, 1750V, 2000V, 2250V, and 2500V. The same parameters are used for a sinusoidal input of 300V, followed by negative and positive

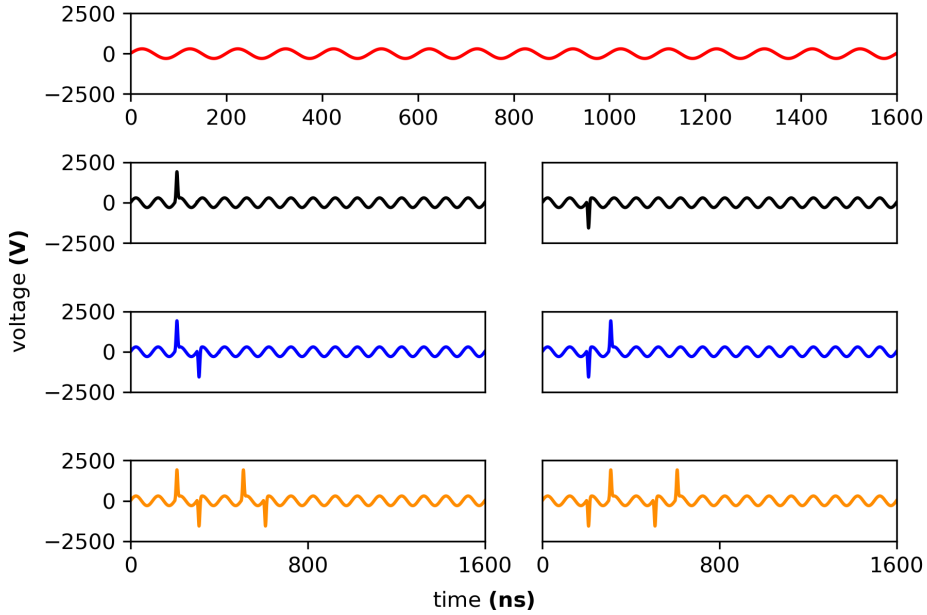

Figure 8.1: Different superposition of the gaussian pulse over the sinusoidal waveform to train the data according to a set of voltages utilized.

pulse cycles. For a dual pulsed sequence, where a sinusoidal voltage of 300V is followed by positive, negative, sinusoidal, positive, and negative pulses, each representing a cycle, the voltages used are 750V, 1000V, 1250V, 1500V, 1750V, 2000V, 2250V, and 2500V. Figure 3.12 showcases these conditions for a pulsed voltage superposed on an input voltage of 300V. The same values are used for the reverse. Figure 8.1 represents the waveforms of the conditions bound by the trained data. A frequency of 10 MHz is utilized in all instances, with the gaussian pulsed superposition of 10% of the duty cycle present.

For the case studies, three cases are examined with the trained DMD algorithm: one within the bounds of the data and two edge cases. All cases except for the sinusoidal case are run at a default sinusoidal value of 300V, with case 3 running at a default sinusoidal value of 150V, as shown in figure 8.2. The other edge case tests the boundary of the pulse discharges from the minimum positive and maximum negative values, as seen in figure 8.2 for case 1. Case 2 of figure 8.2 represents a case within the boundary of the data used to train the model. The values for the cases are as follows:

- **case 1:** 300 sinusoidal, dual pulsed, 750, -2500
- **case 2:** 300 sinusoidal, dual pulsed, 1500, -1250

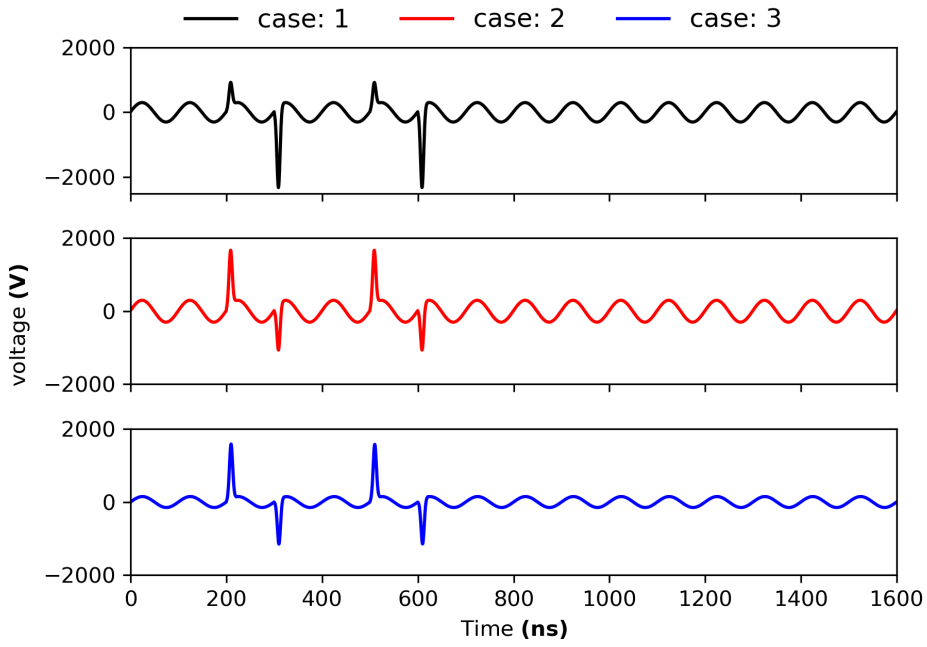

Figure 8.2: Voltage input utilized to compare somaFOAM to DMD algorithm

• **case 3:** 150 sinusoidal, dual pulsed, 1500, -1250

These case parameters generated with the DMD-trained model are also run in somaFOAM to compare the DMD algorithm to that of somaFOAM. The DMD algorithm utilizes a multidimensional input variable, a monolithic variant [60], to train the model. In this instance, the electron number density in the gap is utilized as in comparison to the argon ionized species, the electron dynamics are highly non-linear, making it ideal as to test the capabilities and limitations of the DMD algorithm as a predictive tool.

8.2 Utilization of DMD for predictive modeling

Case 1 - 300 sinusoidal, dual pulsed, 750, -2500

The first case corresponds to an edge case, where the minima and maxima of the voltage ranges are used for the positive and negative pulsed discharge, respectively. From a quick inspection of the data, it can be seen that DMD overestimates the electron bulk at cycle time 2.2T. At 2.2T, as the first pulsed event occurs, the electron dynamics are highly nonlinear, with rapid changes in the electron profile. The percentage of the average difference between somaFOAM and DMD values is 57.71%,

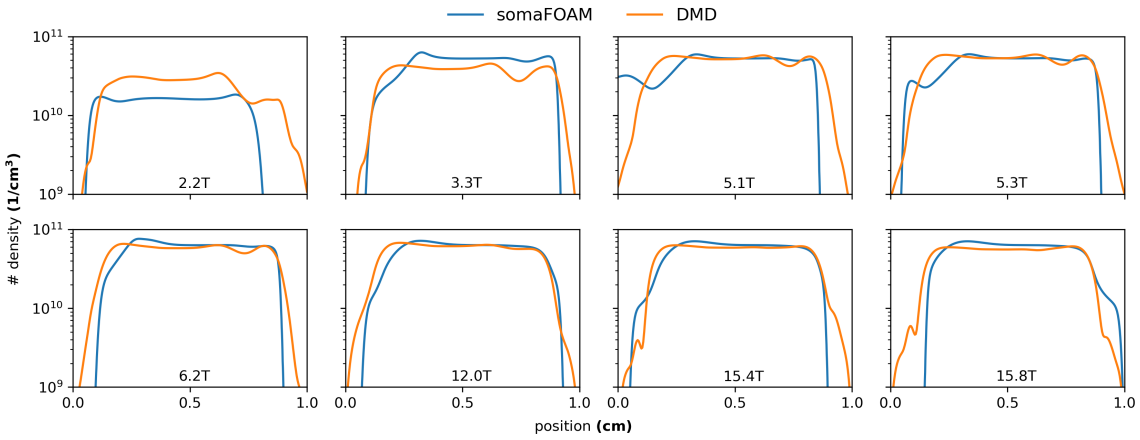

Figure 8.3: Comparison of somaFOAM to DMD generated prediction for the first case.

indicating a large discrepancy at this time step. Since the DMD prediction runs on an edge case where these predictions become less accurate than predictive cases within the bounds of operation, such a result is not unexpected. At cycle time 3.3T, as the pulsed effects start to have less impact on the increase of number density compared to that initial pulse, despite the larger negative pulse, the percentage difference of the average decreases to a value of 16.72%, showcasing better agreement with the data provided by somaFOAM. Further development of the data for cycle time 5.3T, matching the last pulsed cycle of the plasma, shows a percentage difference of the average of 0.44%, showcasing very good agreement.

While the average percentage difference provides a rough idea of the predicted values, it does not fully characterize the differences between both models. Figure 8.4 provides more complete insight into these differences within the profile.

As seen in figure 8.4, the percentage difference is consistently high in the sheath region. This can be accounted for when considering cycle times 2.2T, 3.3T, 5.1T, and 5.3T due to the non-steady state nature of these pulses from either an instant or cycled-average perspective [62, 114, 124]. Furthermore, for cycle times 6.2T, 12.0T, 15.4T, and 15.8T, the discrepancies in the sheath region can be attributed to the relatively coarse dataset used to output the DMD results. A dataset with higher data resolution would be required in highly nonlinear systems to achieve a better characterization that more closely approximates somaFOAM. Nonetheless, it is observed in the bulk region, where the nonlinearities are less intense than those in the sheath region, that there is good data agreement as the solution develops.

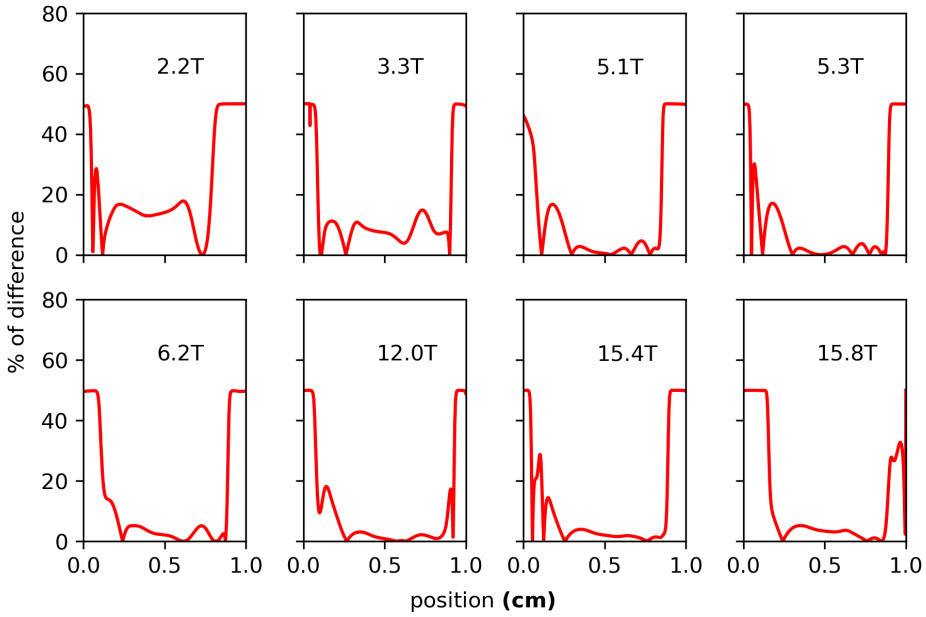

Figure 8.4: Percentage of differences between DMD and somaFOAM for the first case.

Case 2 - 300 sinusoidal, dual pulsed, 1500, -1250

For the second case, as seen in figure 8.5, there is already a better sense of agreement between the DMD prediction and somaFOAM, with a cycle time average percentage difference of 13.78% and 12.62% for cycle times 2.2T and 3.3T, respectively. Further development of the data for cycle time 5.3T, matching the last pulsed cycle of the plasma, shows a percentage difference of the average of 3.38%, showcasing very good agreement. However, the discrepancies at a similar percentage difference as seen in the first case for the sheath region remain, explained by the non-steady-state nature of the pulsed voltage Gaussian superposition in the sinusoidal waveform and the coarse dataset utilized. Figure 8.6 shows the percentage of difference in the profile, where while the bulk electron number density shows very good agreement, the sheath region still presents issues.

Besides increasing the number of cases within the boundary of operating conditions, a possible workaround for the sheath region discrepancies would be to decrease the captured time when generating the data in somaFOAM to a lower value. It might be the case that the Gaussian distribution resolution is not being captured appropriately. The default frequency of operation is 10 MHz, but the Gaussian pulse acts for only 10% of the cycle, i.e., a data point capture of 20 points if the capture time is 5×10^{-10} s. However, such an increase in the sampling rate would significantly enlarge the datasets utilized, posing a problem regarding the generation of the dataset

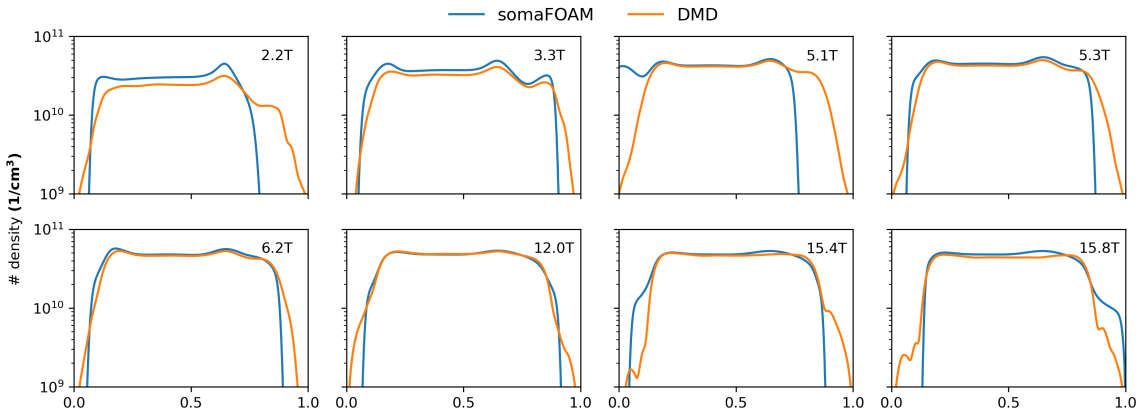

Figure 8.5: Comparison of somaFOAM to DMD generated prediction for the second case.

and processing time when running the DMD algorithm. Nonetheless, exploring this option is not discarded, as the potential benefits could outweigh these drawbacks.

Case 3 - 150 sinusoidal, dual pulsed, 1500, -1250

As the DMD algorithm is explored to its edge cases to determine the limitations of the algorithm, a sinusoidal voltage of 150V is applied, changing the background sinusoidal voltage of 300V on which the data was trained. As seen in figure 8.7, the profile screenshots during the pulsed event at 2.2T, 3.3T, 5.1T, and 5.3T showcase different profiles that do not match each other. While the plasma stabilizes at cycle times 12.0T, 15.4T, and 15.8T, the profile underestimates the number density by a magnitude of 2×10^{10} 1/cm^3 to 4×10^{10} 1/cm^3, indicating a disagreement between somaFOAM and the DMD prediction. Figure 8.8 shows a large discrepancy between somaFOAM and the DMD algorithm for both the sheath and bulk regions, indicating that the database used to train the DMD algorithm is inadequate for predicting such parameters.

To obtain a better prediction, it is recommended that the model be trained with somaFOAM simulations utilizing a sinusoidal voltage of 150V rather than 300V to achieve a better prediction than the one shown. Nonetheless, this serves as a cautionary exercise on the reliance and limitations of predictive algorithms, where the resolution, data points, and parameters of interest are crucial for developing a data-driven predictive model that can accurately predict modeling conditions to reduce computational downtime of CFD tools such as somaFOAM.

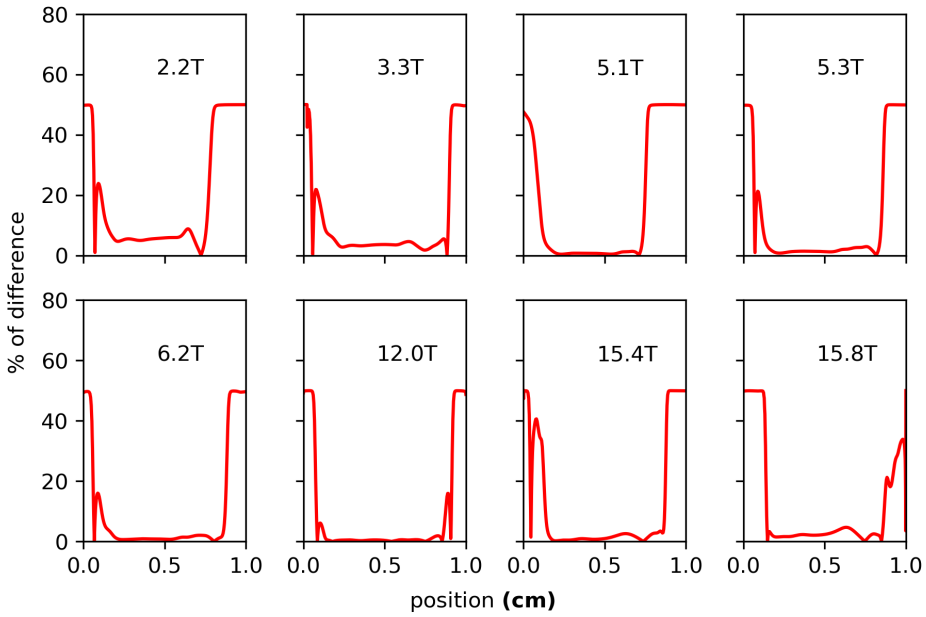

Figure 8.6: Percentage of differences between DMD and somaFOAM for the second case.

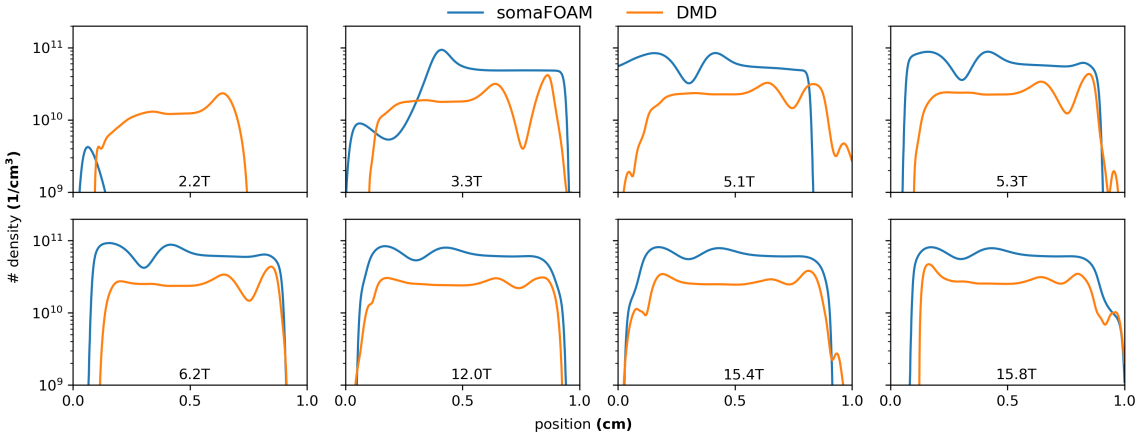

Figure 8.7: Comparison of somaFOAM to DMD generated prediction for the third case.

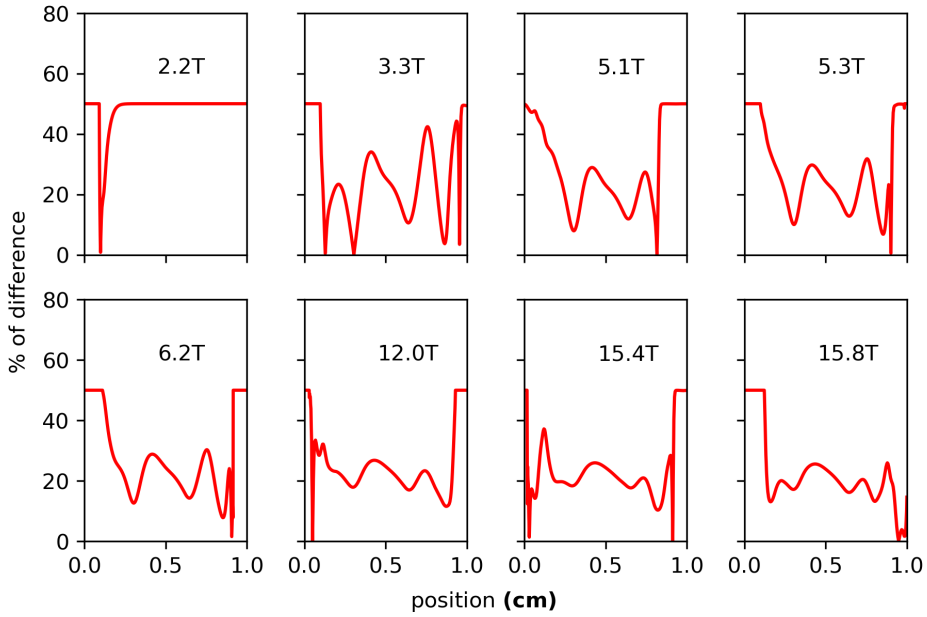

Figure 8.8: Percentage of differences between DMD and somaFOAM for the third case.

8.3 Conclusion

The first test case, an edge case with extreme voltage values, highlighted the limitations of DMD in highly nonlinear regions, particularly during the initial pulsed events. The large discrepancies observed, especially in the sheath region, indicate the challenges in capturing rapid electron dynamics with a coarse dataset. However, as the plasma evolved, the agreement between DMD and somaFOAM improved, showcasing DMD's capability in more stable conditions.

The second case, representing conditions within the trained data bounds, showed significantly better agreement between DMD predictions and somaFOAM results. This indicates that DMD performs well within its training parameters but still faces challenges with the sheath region's non-steady-state nature. The potential to improve predictions by increasing data resolution and sampling rate suggests avenues for future research, balancing the trade-off between dataset size and computational feasibility.

The third case further explored the limits of DMD by applying a sinusoidal voltage different from the training conditions. The observed discrepancies underscore the importance of training data closely matching the intended application conditions. This case is a cautionary example of the limitations of predictive algorithms when extrapolated beyond their trained boundaries.

Overall, the study illustrates the promising potential of DMD as a tool for reducing

computational overhead in plasma modeling. While the algorithm performs well within trained conditions, it highlights the need for comprehensive and high-resolution datasets to capture complex plasma behaviors accurately. Future work should focus on expanding the training datasets, optimizing sampling strategies, and exploring hybrid approaches that combine DMD with traditional CFD methods to enhance predictive accuracy and efficiency. The insights gained from this research contribute to advancing the field of plasma modeling, offering a pathway toward more efficient and scalable computational methods.

Chapter 9

Conclusion

The diagnostic study of helium and argon plasmas under different ignition waveforms was critical to this research. The operating conditions, including using a one-dimensional mesh and specific chemical profiles, were carefully selected to simulate realistic plasma environments. The study revealed that helium plasmas, due to their ease of ignition and stability, serve as a benchmark for understanding basic plasma characteristics. The comparison of sinusoidal, pulsed, and sinusoidal decay waveforms demonstrated that the sinusoidal decay waveform with a damping factor of 0.25 produced the strongest plasma for both helium and argon. This waveform consistently generated higher electron number densities and provided greater stability than other waveforms.

The sinusoidal decay waveform ($\xi = 0.25$) was the most effective for helium plasmas, followed by unipolar, sinusoidal decay ($\xi = 0.1$), sinusoidal, and bipolar waveforms. Electrical characterization of the waveforms showed phase shifts indicating different modes of operation, with the sinusoidal decay waveforms operating in the γ mode, characterized by a transition from capacitive to resistive behavior. The study also highlighted the importance of understanding electron profiles and their distribution, which varied significantly with different waveforms. Similar trends were observed in argon plasmas, with the sinusoidal decay waveform ($\xi = 0.25$) producing the highest number of densities. However, differences between helium and argon plasmas were noted, particularly in the waveforms' effectiveness and the ignition's power requirements. Argon plasmas required higher power inputs to achieve electron number densities similar to helium plasmas. These findings underscore the need for tailored approaches when working with different feedstock gases and highlight the complexities of plasma diagnostics.

The investigation into the α-γ mode of operation provided crucial insights into the stability and efficiency of plasmas under different ignition waveforms. The study examined the voltage-current profiles and identified the critical points where the plasma transitions from the α mode to the γ mode. This transition is marked by changes in differential conductivity and the onset of instabilities. The sinusoidal and bipolar

waveforms exhibited stable γ mode operation up to specific voltage thresholds before becoming unstable. The unipolar pulsed waveform, however, demonstrated inherent instability, transitioning to the γ mode at lower voltage thresholds and exhibiting significant electron activity in the sheath region. This instability was attributed to the bias in sheath activity towards the ground electrode, which accelerates the transition to the γ mode.

The sinusoidal damped waveform ($\xi = 0.25$) showed a unique behavior, maintaining stability even in the γ mode. This stability was linked to the waveform's ability to distribute power efficiently and manage the electron dynamics within the plasma. The study emphasized the importance of considering the external circuit's resistive elements, which play a crucial role in the plasma's electrical characterization and stability. These findings are critical for optimizing plasma processes in applications where maintaining stable operation is essential.

DMD was applied as a data-driven technique to reduce computational overhead in plasma modeling. The DMD algorithm was trained using a comprehensive database generated from somaFOAM simulations under various operating conditions. The algorithm's predictive capabilities were evaluated through multiple case studies, demonstrating its potential to capture the main characteristics of plasma behavior. The first test case, which represented an edge case with extreme voltage values, highlighted the limitations of DMD in highly nonlinear regions. The discrepancies observed during the initial pulsed events indicated challenges in capturing rapid electron dynamics with a coarse dataset. However, the agreement between DMD and somaFOAM improved as the plasma evolved, showcasing DMD's effectiveness in more stable conditions. Within the trained data bounds, the second case showed significantly better agreement between DMD predictions and somaFOAM results. This indicated that DMD performs well within its training parameters but still faces challenges in the sheath region's non-steady-state nature. The potential to improve predictions by increasing data resolution and sampling rate suggests avenues for future research.

The third case explored the limits of DMD by applying a sinusoidal voltage different from the training conditions. The observed discrepancies underscored the importance of training data closely matching the intended application conditions. This case highlighted the limitations of predictive algorithms when extrapolated beyond their trained boundaries, serving as a cautionary example for future applications. These findings offer valuable insights for optimizing plasma processes, particularly in the semiconductor industry, where precise control over plasma characteristics is crucial. Future research should focus on expanding the training datasets for DMD to improve its predictive accuracy, especially in highly nonlinear regions. Additionally, exploring hybrid approaches that combine DMD with traditional CFD methods could enhance plasma simulations' predictive capabilities and efficiency.

Overall, this research provides a robust framework for plasma modeling, offering significant contributions to understanding and optimizing plasma processes. The insights gained pave the way for future plasma physics and engineering advancements,

promoting more efficient and scalable computational methods for various industrial applications.

Bibliography

[1] Anthony L Peratt. "Electric space: Evolution of the plasma universe". In: *Astrophysics and Space Science* 244 (1996), pp. 89–103.

[2] Boris M Smirnov. *Physics of ionized gases*. John Wiley & Sons, 2008.

[3] Shashi K Pankaj and Kevin M Keener. "Cold plasma: Background, applications and current trends". In: *Current Opinion in Food Science* 16 (2017), pp. 49–52.

[4] Lyman Spitzer. *Physics of fully ionized gases*. Courier Corporation, 2006.

[5] S Pekárek. "Non-thermal plasma ozone generation". In: *Acta Polytechnica* 43.6 (2003).

[6] A Fridman, A Chirokov, and A Gutsol. "Non-thermal atmospheric pressure discharges". In: *Journal of Physics D: Applied Physics* 38.2 (2005), R1.

[7] Rong Feng et al. "Experimental investigation on gliding arc discharge plasma ignition and flame stabilization in scramjet combustor". In: *Aerospace Science and Technology* 79 (2018), pp. 145–153.

[8] Michael Keidar, Minkwan Kim, and Iain D Boyd. "Electromagnetic reduction of plasma density during atmospheric reentry and hypersonic flights". In: *Journal of Spacecraft and Rockets* 45.3 (2008), pp. 445–453.

[9] Nicholas J Bisek, Iain D Boyd, and Jonathan Poggie. "Numerical study of plasma-assisted aerodynamic control for hypersonic vehicles". In: *Journal of Spacecraft and Rockets* 46.3 (2009), pp. 568–576.

[10] Ambarish Vaidyanathan et al. "Characterization of fuel gas products from the treatment of solid waste streams with a plasma arc torch". In: *Journal of Environmental Management* 82.1 (2007), pp. 77–82.

[11] Yasunori Tanaka, Takayasu Fujino, and Toru Iwao. "Review of thermal plasma simulation technique". In: *IEEJ Transactions on Electrical and Electronic Engineering* 14.11 (2019), pp. 1582–1594.

[12] P Freton et al. "Numerical and experimental study of a plasma cutting torch". In: *Journal of Physics D: Applied Physics* 35.2 (2001), p. 115.

[13] Yoshitaka Mitsuda, Toyonobu Yoshida, and Kazuo Akashi. "Development of a new microwave plasma torch and its application to diamond synthesis". In: *Review of scientific instruments* 60.2 (1989), pp. 249–252.

[14] Tomohiro Okumura. "Inductively coupled plasma sources and applications". In: *Physics Research International* 2010.1 (2010), p. 164249.

[15] Bogdan Hnatiuc et al. "Diagnostic of plasma produced by a spark plug at atmospheric pressure: Reduced electric field and vibrational temperature". In: *Contributions to Plasma Physics* 54.8 (2014), pp. 712–723.

[16] Klaus Bergmann et al. "Highly repetitive, extreme-ultraviolet radiation source based on a gas-discharge plasma". In: *Applied Optics* 38.25 (1999), pp. 5413–5417.

[17] Kenro Miyamoto. *Plasma physics and controlled nuclear fusion*. Vol. 38. Springer Science & Business Media, 2005.

[18] Ronny Brandenburg. "Dielectric barrier discharges: progress on plasma sources and on the understanding of regimes and single filaments". In: *Plasma Sources Science and Technology* 26.5 (2017), p. 053001.

[19] Ruiqiang Liu et al. "A comparative study on continuous and pulsed RF argon capacitive glow discharges at low pressure by fluid modeling". In: *Physics of Plasmas* 24.1 (2017), p. 013517.

[20] RJ Shul et al. "High-density plasma etching of compound semiconductors". In: *Journal of Vacuum Science & Technology A: Vacuum, Surfaces, and Films* 15.3 (1997), pp. 633–637.

[21] Ulrich Kogelschatz and B Eliasson. "Fundamentals and applications of dielectric-barrier discharges". In: *HAKONE VII Int. Symp. On High Pressure Low Temperature Plasma Chemistry, Greifswald*. Citeseer. 2000.

[22] Tanvir Farouk et al. "Atmospheric pressure radio frequency glow discharges in argon: effects of external matching circuit parameters". In: *Plasma Sources Science and Technology* 17.3 (2008), p. 035015.

[23] Gregory Fridman et al. "Applied plasma medicine". In: *Plasma processes and polymers* 5.6 (2008), pp. 503–533.

[24] Michael G Kong and Xu Tao Deng. "Electrically efficient production of a diffuse nonthermal atmospheric plasma". In: *IEEE transactions on plasma science* 31.1 (2003), pp. 7–18.

[25] Wanli Shang, Dezhen Wang, and Yuantao Zhang. "Radio frequency atmospheric pressure glow discharge in α and γ modes between two coaxial electrodes". In: *Physics of Plasmas* 15.9 (2008), p. 093503.

[26] Ulrich Kogelschatz. “Dielectric-barrier discharges: their history, discharge physics, and industrial applications”. In: *Plasma chemistry and plasma processing* 23.1 (2003), pp. 1–46.

[27] Ian W Boyd and Irving I Liaw. “Development and application of UV excimer lamps from 354nm-126nm”. In: *High-Power Laser Ablation VI*. Vol. 6261. SPIE. 2006, pp. 27–42.

[28] André Anders. “Plasma and ion sources in large area coating: A review”. In: *Surface and Coatings Technology* 200.5-6 (2005), pp. 1893–1906.

[29] Jacques Schmitt, Mustapha Elyaakoubi, and Laurent Sansonnens. “Glow discharge processing in the liquid crystal display industry”. In: *Plasma Sources Science and Technology* 11.3A (2002), A206.

[30] Françoise Massines, Nicolas Gherardi, and Françoise Sommer. “Silane-based coatings on polypropylene, deposited by atmospheric pressure glow discharge plasmas”. In: *Plasmas and polymers* 5 (2000), pp. 151–172.

[31] JJ Shi and Michael G Kong. “Expansion of the plasma stability range in radio-frequency atmospheric-pressure glow discharges”. In: *Applied Physics Letters* 87.20 (2005), p. 201501.

[32] JJ Shi, DW Liu, and Michael G Kong. “Plasma stability control using dielectric barriers in radio-frequency atmospheric pressure glow discharges”. In: *Applied physics letters* 89.8 (2006), p. 081502.

[33] Amy E Wendt and William Nicholas Guy Hitchon. “Electron heating by sheaths in radio frequency discharges”. In: *Journal of applied physics* 71.10 (1992), pp. 4718–4726.

[34] Lu-Lu Zhao, Yue Liu, and Tagra Samir. “Numerical study on discharge characteristics influenced by secondary electron emission in capacitive RF argon glow discharges by fluid modeling”. In: *Chinese Physics B* 27.2 (2018), p. 025201.

[35] Jie Pan et al. “Comparative study of pulsed dielectric barrier discharges in argon and nitrogen at atmospheric pressure”. In: *IEEE Transactions on Plasma Science* 43.2 (2015), pp. 557–566.

[36] Zhi Fang et al. “Generation of homogeneous atmospheric-pressure dielectric barrier discharge in a large-gap argon gas”. In: *IEEE Transactions on Plasma Science* 40.7 (2012), pp. 1884–1890.

[37] J-P Boeuf. “A two-dimensional model of dc glow discharges”. In: *Journal of applied physics* 63.5 (1988), pp. 1342–1349.

[38] Da Wei Liu, Felipe Iza, and Michael G Kong. “Evolution of atmospheric-pressure RF plasmas as the excitation frequency increases”. In: *Plasma Processes and Polymers* 6.6-7 (2009), pp. 446–450.

[39] Nicolas Balcon, GJM Hagelaar, and JP Boeuf. "Numerical model of an argon atmospheric pressure RF discharge". In: *IEEE transactions on plasma science* 36.5 (2008), pp. 2782–2787.

[40] Dongsoo Lee et al. "Numerical simulation on mode transition of atmospheric dielectric barrier discharge in helium-oxygen mixture". In: *IEEE transactions on plasma science* 33.2 (2005), pp. 949–957.

[41] Gerardus Johannes Maria Hagelaar. *Modeling of microdischarges for display technology*. Vol. 109. Technische Universiteit Eindhoven Eindhoven, 2000.

[42] Miloslav Štefečka et al. "Experimental study of atmospheric pressure surface discharge in helium". In: *Science and Technology of Advanced materials* 2.3-4 (2001), pp. 587–593.

[43] Ruiqiang Liu et al. "Fluid modeling of plasma dynamics in pulsed RF capacitive glow discharges in low pressure argon". In: *Physics of Plasmas* 24.8 (2017).

[44] JJ Shi et al. "Three modes in a radio frequency atmospheric pressure glow discharge". In: *Journal of applied physics* 94.10 (2003), pp. 6303–6310.

[45] Jianjun Shi and Michael G Kong. "Mode characteristics of radio-frequency atmospheric glow discharges". In: *IEEE transactions on plasma science* 33.2 (2005), pp. 624–630.

[46] X Yang et al. "Comparison of an atmospheric pressure, radio-frequency discharge operating in the α and γ modes". In: *Plasma Sources Science and Technology* 14.2 (2005), p. 314.

[47] JJ Shi and MG Kong. "Mechanisms of the α and γ modes in radio-frequency atmospheric glow discharges". In: *Journal of applied physics* 97.2 (2005), p. 023306.

[48] Leandro Olano et al. "Dynamic secondary electron emission in rough composite materials". In: *Scientific reports* 9.1 (2019), pp. 1–10.

[49] JJ Shi, DW Liu, and Michael G Kong. "Mitigating plasma constriction using dielectric barriers in radio-frequency atmospheric pressure glow discharges". In: *Applied physics letters* 90.3 (2007), p. 031505.

[50] Se Youn Moon et al. "α, γ, and normal, abnormal glow discharge modes in radio-frequency capacitively coupled discharges at atmospheric pressure". In: *Physics of plasmas* 13.3 (2006), p. 033502.

[51] F Massines and G Gouda. "A comparison of polypropylene-surface treatment by filamentary, homogeneous and glow discharges in helium at atmospheric pressure". In: *Journal of Physics D: Applied Physics* 31.24 (1998), p. 3411.

[52] Friedrich Paschen. *Ueber die zum funkenübergang in luft: wasserstoff und kohlensäure bei verschiedenen drucken erforderliche potentialdifferenz...* JA Barth, 1889.

[53] Erich E Kunhardt. "Generation of large-volume, atmospheric-pressure, nonequilibrium plasmas". In: *IEEE transactions on plasma science* 28.1 (2000), pp. 189–200.

[54] DB Go and A Venkattraman. "Microscale gas breakdown: ion-enhanced field emission and the modified Paschen's curve". In: *Journal of Physics D: Applied Physics* 47.50 (2014), p. 503001.

[55] Saurav Gautam and Gabriele Morra. "Pre-breakdown to stable phase and origin of multiple current pulses in argon dielectric barrier discharge". In: *Plasma Science and Technology* 23.12 (2021), p. 125403.

[56] JJ Shi and Michael G Kong. "Radio-frequency dielectric-barrier glow discharges in atmospheric argon". In: *Applied physics letters* 90.11 (2007), p. 111502.

[57] Joshua L Proctor, Steven L Brunton, and J Nathan Kutz. "Dynamic mode decomposition with control". In: *SIAM Journal on Applied Dynamical Systems* 15.1 (2016), pp. 142–161.

[58] JJ Shi and Michael G Kong. "Mode transition in radio-frequency atmospheric argon discharges with and without dielectric barriers". In: *Applied Physics Letters* 90.10 (2007), p. 101502.

[59] Farbod Faraji et al. "Dynamic mode decomposition for data-driven analysis and reduced-order modeling of E× B plasmas: I. Extraction of spatiotemporally coherent patterns". In: *Journal of Physics D: Applied Physics* 57.6 (2023), p. 065201.

[60] Francesco Andreuzzi, Nicola Demo, and Gianluigi Rozza. "A dynamic mode decomposition extension for the forecasting of parametric dynamical systems". In: *SIAM Journal on Applied Dynamical Systems* 22.3 (2023), pp. 2432–2458.

[61] Ziyou Wu, Steven L Brunton, and Shai Revzen. "Challenges in dynamic mode decomposition". In: *Journal of the Royal Society Interface* 18.185 (2021), p. 20210686.

[62] J Nathan Kutz et al. *Dynamic mode decomposition: data-driven modeling of complex systems*. SIAM, 2016.

[63] James L Walsh and Michael G Kong. "10ns pulsed atmospheric air plasma for uniform treatment of polymeric surfaces". In: *Applied Physics Letters* 91.25 (2007).

[64] Yuan-Tao Zhang and Shao-Yan Cui. "Frequency effects on the electron density and α-γ mode transition in atmospheric radio frequency discharges". In: *Physics of Plasmas* 18.8 (2011), p. 083509.

[65] Peter J Schmid. "Dynamic mode decomposition of numerical and experimental data". In: *Journal of fluid mechanics* 656 (2010), pp. 5–28.

[66] Michael A Lieberman and Alan J Lichtenberg. *Principles of plasma discharges and materials processing*. John Wiley & Sons, 2005.

[67] William H. Green. *Combustion Chemistry*. url=https://cefrc.princeton.edu/sites/g/files/toruqf1071/files/Files/2014%20Lecture%20Notes/Green/Combustion-Chemistry-part-1.pdf. June 2014.

[68] Nicholas A Krall and Alvin W Trivelpiece. "Principles of plasma physics". In: *American Journal of Physics* 41.12 (1973), pp. 1380–1381.

[69] Qiang Wang, Demetre J Economou, and Vincent M Donnelly. "Simulation of a direct current microplasma discharge in helium at atmospheric pressure". In: *Journal of Applied Physics* 100.2 (2006), p. 023301.

[70] GJM Hagelaar, FJ De Hoog, and GMW Kroesen. "Boundary conditions in fluid models of gas discharges". In: *Physical Review E* 62.1 (2000), p. 1452.

[71] Althea Wilson and Babak Shotorban. "Investigation of surface boundary conditions for continuum modeling of RF plasmas". In: *Physics of Plasmas* 25.5 (2018).

[72] Miles M Turner. "Computer Simulation in Low-Temperature Plasma Physics: Future Challenges". In: *Plasma Processes and Polymers* 14.1-2 (2017), p. 1600121.

[73] M Mortazavi et al. "Modelling of Electric Field Distribution in a Non-thermal Plasma Reactor using COMSOL Multiphysics®". In: (2020).

[74] Roman Fuchs. *Plasma Simulation in STAR-CCM+ - towards a modern software tool*.

[75] GM Janssen et al. "PLASIMO, a general model: I. Applied to an argon cascaded arc plasma". In: *Plasma Sources Science and Technology* 8.1 (1999), p. 1.

[76] Stephen C Dewhurst and Kathy T Stark. *Programming in C++*. Prentice-Hall, Inc., 1989.

[77] Nicholas D Matsakis and Felix S Klock. "The rust language". In: *ACM SIGAda Ada Letters* 34.3 (2014), pp. 103–104.

[78] Brian W Kernighan and Dennis M Ritchie. "The C programming language". In: (2002).

[79] Hans Fangohr. "A comparison of C, MATLAB, and Python as teaching languages in engineering". In: *International Conference on Computational Science*. Springer. 2004, pp. 1210–1217.

[80] Aleksandar Ćoćić and Iva Guranov. "An Overview of OpenFOAM CFD Software". In: *Proceedings of Third International Symposium Contemporary problems of Fluid Mechanics, Belgrade, Serbia, May 2011*. University of Belgrade, Faculty of Mechanical Engineering. 2011, pp. 119–126.

[81] Hrvoje Jasak, Aleksandar Jemcov, Zeljko Tukovic, et al. "OpenFOAM: A C++ library for complex physics simulations". In: *International workshop on coupled methods in numerical dynamics*. Vol. 1000. 2007, pp. 1–20.

[82] F Moukalled L Mangani M Darwish. *The finite volume method in computational fluid dynamics*. 2016.

[83] Dale Anderson et al. *Computational fluid mechanics and heat transfer*. CRC press, 2020.

[84] James Stewart. *Calculus: early transcendentals*. Cengage Learning, 2012.

[85] Hrvoje Jasak. "Error analysis and estimation for the finite volume method with applications to fluid flows." In: (1996).

[86] Christopher J Greenshields. "OpenFOAM programmer's guide". In: *OpenFOAM Foundation Ltd* (2015).

[87] Venkattraman Ayyaswamy. *SOMAFOAM*. `https://github.com/vayyaswamy/SOMAFOAM`. 2018.

[88] Alejandro Alonzo-García, Claudia del Carmen Gutiérrez-Torres, and José Alfredo Jiménez-Bernal. "Computational fluid dynamics in turbulent flow applications". In: *Numerical Simulation-From Brain Imaging to Turbulent Flows* (2016), pp. 316–338.

[89] Abhishek Kumar Verma and Ayyaswamy Venkattraman. "SOMAFOAM: An OpenFOAM based solver for continuum simulations of low-temperature plasmas". In: *Computer Physics Communications* 263 (2021), p. 107855.

[90] Yousef Saad. *Iterative methods for sparse linear systems*. SIAM, 2003.

[91] Israa Abdulameer Resen, Rana IK Zaki, and Hussam K Risan. "Graphical Comparison of Critically Damped Versus Overdamped Free Vibration of Single Degree of Freedom Structure". In: *Journal of Southwest Jiaotong University* 54.5 (2019).

[92] Rajesh Bhaskaran and Lance Collins. "Introduction to CFD basics". In: *Cornell University-Sibley School of Mechanical and Aerospace Engineering* (2002), pp. 1–21.

[93] Richard Courant, Kurt Friedrichs, and Hans Lewy. "On the partial difference equations of mathematical physics". In: *IBM journal of Research and Development* 11.2 (1967), pp. 215–234.

[94] Theresa. *How To Keep the Courant Number Below 1?* url=https://www.simscale.com/knowledge-base/what-is-a-courant-number. Feb. 2020.

[95] Guilherme Caminha. *The CFL Condition and How to Choose Your Timestep Size*. url=https://www.simscale.com/blog/2017/08/cfl-condition/. Oct. 2019.

[96] HW Ellis et al. “Transport properties of gaseous ions over a wide energy range”. In: *Atomic Data and Nuclear Data Tables* 17.3 (1976), pp. 177–210.

[97] HW Ellis et al. “Transport properties of gaseous ions over a wide energy range. Part II”. In: *Atomic data and nuclear data tables* 22.3 (1978), pp. 179–217.

[98] H.W. Ellis et al. “Transport properties of gaseous ions over a wide energy range. Part III”. In: *Atomic Data and Nuclear Data Tables* 31.1 (1984), pp. 113–151. ISSN: 0092-640X. DOI: https://doi.org/10.1016/0092-640X(84)90018-4. URL: https://www.sciencedirect.com/science/article/pii/0092640X84900184.

[99] L.A. Viehland and E.A. Mason. “Transport Properties of Gaseous Ions over a Wide Energy Range, IV”. In: *Atomic Data and Nuclear Data Tables* 60.1 (1995), pp. 37–95. ISSN: 0092-640X. DOI: https://doi.org/10.1006/adnd.1995.1004. URL: https://www.sciencedirect.com/science/article/pii/S0092640X85710042.

[100] William E Wallace. “Mass spectra”. In: *NIST chemistry webbook, NIST standard reference database* 69 (2018).

[101] GJM Hagelaar and L C Pitchford. “Solving the Boltzmann equation to obtain electron transport coefficients and rate coefficients for fluid models”. In: *Plasma Sources Science and Technology* 14.4 (2005), p. 722.

[102] Valery A Godyak. “Nonequilibrium EEDF in gas discharge plasmas”. In: *IEEE transactions on plasma science* 34.3 (2006), pp. 755–766.

[103] GJM Hagelaar. “Brief documentation of BOLSIG+ version 03/2016”. In: *Laboratoire Plasma et Conversion dEnergie (LAPLACE), Universit Paul Sabatier* 118 (2016).

[104] EV Karoulina and Yu A Lebedev. “Computer simulation of microwave and DC plasmas: comparative characterisation of plasmas”. In: *Journal of Physics D: Applied Physics* 25.3 (1992), p. 401.

[105] SK Lam et al. “Kinetics of Ar* 2 in high-pressure pure argon”. In: *Journal of Physics D: Applied Physics* 33.3 (2000), p. 242.

[106] Byoung-Kuk Min, Seok-Hyun Lee, and Hun-Gun Park. “New combination of a three-component gas, Ne–Xe–Ar, for a high efficiency plasma display panel”. In: *Journal of Vacuum Science & Technology A: Vacuum, Surfaces, and Films* 18.2 (2000), pp. 349–355.

[107] CM Ferreira, J Loureiro, and A Ricard. “Populations in the metastable and the resonance levels of argon and stepwise ionization effects in a low-pressure argon positive column”. In: *Journal of applied physics* 57.1 (1985), pp. 82–90.

[108] Shahid Rauf and Mark J Kushner. "Dynamics of a coplanar-electrode plasma display panel cell. I. Basic operation". In: *Journal of applied physics* 85.7 (1999), pp. 3460–3469.

[109] Jong W Shon and Mark J Kushner. "Excitation mechanisms and gain modeling of the high-pressure atomic Ar laser in He/Ar mixtures". In: *Journal of applied physics* 75.4 (1994), pp. 1883–1890.

[110] KR Stalder et al. "Modeling the chemical kinetics of high-pressure glow discharges in mixtures of helium with real air". In: *Journal of applied physics* 99.9 (2006), p. 093301.

[111] Christopher J Greenshields et al. "Openfoam user guide version 6". In: *The OpenFOAM Foundation* 237 (2018), p. 624.

[112] Christophe Geuzaine and Jean-François Remacle. "Gmsh: A 3-D finite element mesh generator with built-in pre-and post-processing facilities". In: *International journal for numerical methods in engineering* 79.11 (2009), pp. 1309–1331.

[113] Boris Kramer et al. "Sparse sensing and DMD-based identification of flow regimes and bifurcations in complex flows". In: *SIAM Journal on Applied Dynamical Systems* 16.2 (2017), pp. 1164–1196.

[114] Jonathan H Tu. "Dynamic mode decomposition: Theory and applications". PhD thesis. Princeton University, 2013.

[115] Bingni W Brunton et al. "Extracting spatial–temporal coherent patterns in large-scale neural recordings using dynamic mode decomposition". In: *Journal of neuroscience methods* 258 (2016), pp. 1–15.

[116] Amirhossein Arzani and Scott TM Dawson. "Data-driven cardiovascular flow modelling: examples and opportunities". In: *Journal of the Royal Society Interface* 18.175 (2021), p. 20200802.

[117] Joshua L Proctor and Philip A Eckhoff. "Discovering dynamic patterns from infectious disease data using dynamic mode decomposition". In: *International health* 7.2 (2015), pp. 139–145.

[118] Erik Berger et al. "Estimation of perturbations in robotic behavior using dynamic mode decomposition". In: *Advanced Robotics* 29.5 (2015), pp. 331–343.

[119] Jordan Mann and J Nathan Kutz. "Dynamic mode decomposition for financial trading strategies". In: *Quantitative Finance* 16.11 (2016), pp. 1643–1655.

[120] Clarence W Rowley et al. "Spectral analysis of nonlinear flows". In: *Journal of fluid mechanics* 641 (2009), pp. 115–127.

[121] Eurika Kaiser, J Nathan Kutz, and Steven L Brunton. "Sparse identification of nonlinear dynamics for model predictive control in the low-data limit". In: *Proceedings of the Royal Society A* 474.2219 (2018), p. 20180335.

[122] Yueheng Lan and Igor Mezić. "Linearization in the large of nonlinear systems and Koopman operator spectrum". In: *Physica D: Nonlinear Phenomena* 242.1 (2013), pp. 42–53.

[123] Scott TM Dawson et al. "Characterizing and correcting for the effect of sensor noise in the dynamic mode decomposition". In: *Experiments in Fluids* 57 (2016), pp. 1–19.

[124] Steven L Brunton and J Nathan Kutz. *Data-driven science and engineering: Machine learning, dynamical systems, and control*. Cambridge University Press, 2022.

[125] Rowayda A Sadek. "SVD based image processing applications: state of the art, contributions and research challenges". In: *arXiv preprint arXiv:1211.7102* (2012).

[126] Nicolas Balcon. "Atmospheric pressure Radio Frequency discharges, diagnostic and numerical modeling". PhD thesis. Université Paul Sabatier-Toulouse III; Australian National University, 2007.

[127] Jaeyoung Park et al. "Discharge phenomena of an atmospheric pressure radio-frequency capacitive plasma source". In: *Journal of Applied Physics* 89.1 (2001), pp. 20–28.

[128] Tanvir Farouk et al. "Simulation of dc atmospheric pressure argon micro glow-discharge". In: *Plasma Sources Science and Technology* 15.4 (2006), p. 676.

[129] Wolfgang Schmitt, Walter E Köhler, and Hanns Ruder. "A one-dimensional model of dc glow discharges". In: *Journal of applied physics* 71.12 (1992), pp. 5783–5791.

[130] JJ Shi and Michael G Kong. "Cathode fall characteristics in a dc atmospheric pressure glow discharge". In: *Journal of applied physics* 94.9 (2003), pp. 5504–5513.

[131] M Baeva et al. "Fluid modelling of DC argon microplasmas: effects of the electron transport description". In: *Plasma Chemistry and Plasma Processing* 39.4 (2019), pp. 949–968.

[132] Suramoni Borthakur et al. "200 kJ pulsed power system for pulsed plasma device". In: *IEEE Transactions on Plasma Science* 45.7 (2017), pp. 1769–1775.

[133] ShuQun Wu et al. "A touchable pulsed air plasma plume driven by DC power supply". In: *IEEE transactions on plasma science* 38.12 (2010), pp. 3404–3408.

[134] Yueh-Ru Yang and Wen-Yao Lee. "A DC-pulse power supply designed for plasma applications". In: *2009 International Conference on Power Electronics and Drive Systems (PEDS)*. IEEE. 2009, pp. 1086–1090.

[135] E Panousis et al. “Analysis of dielectric barrier discharges under unipolar and bipolar pulsed excitation”. In: *IEEE Transactions on Dielectrics and Electrical Insulation* 16.3 (2009), pp. 734–741.

[136] M Atanasova et al. “Driving frequency dependence of capacitively coupled plasmas in atmospheric argon”. In: *Journal of Physics D: Applied Physics* 45.33 (2012), p. 335201.